

# REPORT DOCUMENTATION PAGE

Form Approved  
OMB No. 0704-0188

Public reporting burden for this collection of information is estimated to average 1 hour per response, including the time for reviewing instructions, searching data sources, gathering and maintaining the data needed, and completing and reviewing the collection of information. Send comments regarding this burden estimate or any other aspect of this collection of information, including suggestions for reducing this burden to Washington Headquarters Service, Directorate for Information Operations and Reports, 1215 Jefferson Davis Highway, Suite 1204, Arlington, VA 22202-4302, and to the Office of Management and Budget, Paperwork Reduction Project (0704-0188) Washington, DC 20503.

PLEASE DO NOT RETURN YOUR FORM TO THE ABOVE ADDRESS.

1. REPORT DATE (DD-MM-YYYY)		2. REPORT TYPE Final Technical Report		3. DATES COVERED (From - To) 01 Apr 2003 – 30 Jun 2006	
4. TITLE AND SUBTITLE Nonlinear Oscillations of Microscale Piezoelectric Resonators and Resonator Arrays				5a. CONTRACT NUMBER	
				5b. GRANT NUMBER F49620-03-1-0181	
				5c. PROGRAM ELEMENT NUMBER	
6. AUTHOR(S) Professor B. Balachandran				5d. PROJECT NUMBER	
				5e. TASK NUMBER	
				5f. WORK UNIT NUMBER	
7. PERFORMING ORGANIZATION NAME(S) AND ADDRESS(ES) Department of Mechanical Engineering University of Maryland College Park MD 20742-3035				8. PERFORMING ORGANIZATION REPORT NUMBER	
9. SPONSORING/MONITORING AGENCY NAME(S) AND ADDRESS(ES)  Air Force Office of Scientific Research (AFOSR) 875 N. Arlington St., Rm. 3112 Arlington, VA 22203 <i>Dr Victor Giurgintu/NA</i>				10. SPONSOR/MONITOR'S ACRONYM(S) AFOSR	
				11. SPONSORING/MONITORING AGENCY REPORT NUMBER N/A	
12. DISTRIBUTION AVAILABILITY STATEMENT  DISTRIBUTION A: Approved for public release; distribution unlimited. <span style="float: right;">AFRL-SR-AR-TR-07-0071</span>					
13. SUPPLEMENTARY NOTES					
14. ABSTRACT Oscillations of clamped-clamped and free-free micro-electromechanical resonators and resonator arrays have been studied in this effort. Piezoelectric actuation is used to excite these resonator structures on the input side and piezoelectric sensing is carried out on the output side. Composite structural models have been developed for these filters, and analyses has been carried out to explain experimental observations of nonlinear phenomena as well as to guide the design of these filters are presented. Semi-analytical design tools for micro-electromechanical resonators and micro-electromechanical resonator arrays have been developed. The phenomenon of intrinsic localized modes in resonator arrays has also been studied, and it is shown that these modes can be explained as forced nonlinear vibration modes. The research findings can open the doors to new resonator array designs.					
15. SUBJECT TERMS					
16. SECURITY CLASSIFICATION OF:			17. LIMITATION OF ABSTRACT	18. NUMBER OF PAGES	19a. NAME OF RESPONSIBLE PERSON
a. REPORT Unclassified	b. ABSTRACT Unclassified	c. THIS PAGE Unclassified	Unclassified	54	19b. TELEPHONE NUMBER (Include area code) (703)

# NONLINEAR OSCILLATIONS OF MICROSCALE PIEZOELECTRIC RESONATORS AND RESONATOR ARRAYS

AFOSR GRANT F49620-03-10181

B. Balachandran  
Professor  
Department of Mechanical Engineering  
University of Maryland  
College Park, MD 20742-3035  
PH: (301)405-5309  
FAX: (301)314-9477  
E-mail: balab@eng.umd.edu

## Abstract

Oscillations of clamped-clamped and free-free micro-electromechanical resonators and resonator arrays have been studied in this effort. Piezoelectric actuation is used to excite these resonator structures on the input side and piezoelectric sensing is carried out on the output side. Composite structural models have been developed for these filters, and analyses has been carried out to explain experimental observations of nonlinear phenomena as well as to guide the design of these filters are presented. Semi-analytical design tools for micro-electromechanical resonators and micro-electromechanical resonator arrays have been developed. The phenomenon of intrinsic localized modes in resonator arrays has also been studied, and it is shown that these modes can be explained as forced nonlinear vibration modes. The research findings can open the doors to new resonator array designs.

Keywords: microscale resonators, buckling, nonlinear phenomena, axial-load effects, piezoelectric actuation, Duffing oscillator, resonator arrays, intrinsic localized modes.

## 1. Introduction

Two types of piezoelectrically actuated micro-scale resonators, which are attractive for communication and signal-processing applications [1], are considered in this research effort. One type of resonators will be referred to as the AlGaAs resonator, and the other type of resonators will be referred to as the PZT resonator. Both types of resonators are composite structures, and the PZT resonators have asymmetric cross-sections, as shown in Figure 1. During the fabrication of the resonators, residual stresses are likely to be

introduced and the effect of these stresses is explored in this work. As pointed out in the authors' recent work, the resonators also exhibit non-linear characteristics [2-5]. These characteristics include Duffing oscillator like response during resonance excitations [6], temporal harmonics in the response, and spatial patterns during forced oscillations that cannot be explained by conventional linear analysis.

The rest of this report is organized as follows. In Section 2, the first component of the research activity is described. This section contains a discussion of a semi-analytical tool developed to study transverse free vibrations of clamped-clamped resonators subjected to constant axial loads. In Section 3, nonlinear analysis used to study dynamic buckling in microscale resonators is presented. Following that, progress made towards using an experimentally obtained frequency response for parametrically identifying a nonlinear oscillator model of a micro-resonator is described. In Section 5, work being conducted with arrays of composite microresonators is briefly discussed. A summary is provided in Section 6. References including the publications that came out of this work are included in Section 7. The research participants are provided in Section 8 and transitions and interactions are discussed in Section 9. A list of publications that have followed from this work is provided in Section 10, and invention disclosure made through this work is provided in Section 11.

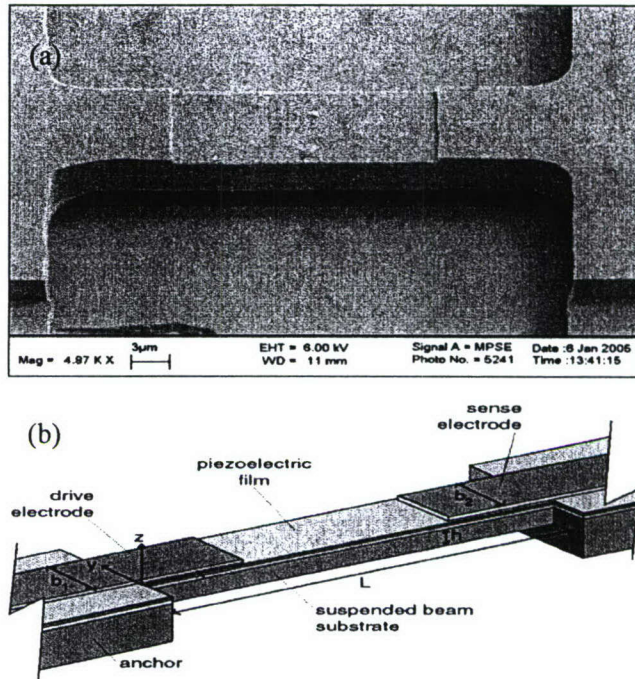


Figure 1: (a) SEM of a PZT resonator (Courtesy, Maryland MEMS Laboratory) and a schematic showing the details [1].

## 2. Semi-Analytical Tool Development

Based on a formulation with geometric nonlinearities, a semi-analytical tool [7, 8] has been developed for studying transverse free vibrations of clamped-clamped and free-free resonators subjected to constant axial loads. It is shown that the consideration of axial loads is important to predict the natural frequencies of the resonators observed in the experiments. In

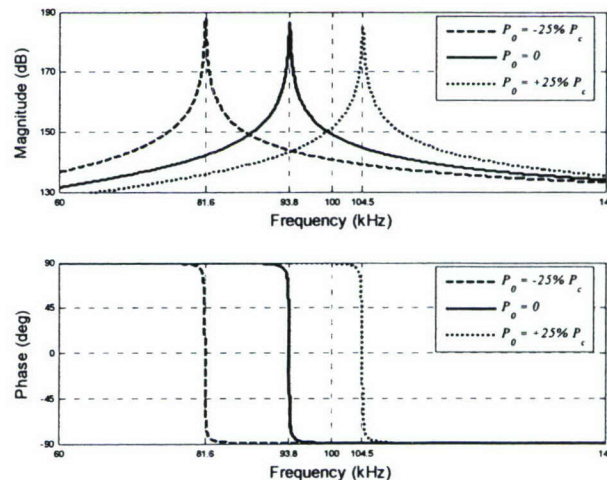


Figure 2: Response of a 400  $\mu\text{m}$  AlGaAs for three different values of the axial load [7].

addition, the developed model and the numerical implementation can be used to understand the influence of uncertainties associated with the fabrication process. Representative results obtained for a 400  $\mu\text{m}$  long resonator are shown in Figure 2. These results show how the center frequency of a filter can be shifted by using an axial load. Additional details of the work can be found in the paper [8] included at the end of the report.

### 3. Dynamic Buckling of Composite Micro-Scale Structures: Nonlinear Analysis

The resonators considered in this effort are based on the piezoelectric effect (see Figure 1). In the case of the PZT resonators, the elastic substrate is a  $\text{SiO}_2$  layer, on top of which a platinum electrode layer is deposited throughout the length of the structure. A thin layer of sol-gel piezoelectric film is located on the top of this electrode layer. To complete the structure, another platinum layer on the top of this piezoelectric film extends over one quarter of the length from each anchor and the mid-section of the resonator structure is free from this platinum electrode [1]. Due to the asymmetry of the cross section, the position of the piezoelectric layer is offset from the neutral axis, and in addition, (tensional) residual stress may also be introduced in each layer during the manufacturing process. In some typical uses of this resonator, the structure is driven close to its first resonance frequency with a DC bias in the input. So, the axial loads in a resonator can be attributed to the DC bias as well as the residual stresses.

It is believed that some of the experimental observations made in previous efforts can be explained by considering oscillations about a non-flat equilibrium position. Here, it is assumed that this non-flat equilibrium position arises due to buckling. Hence, the primary thrust of this component has been to examine if oscillations of a buckled system can be used to explain experimentally observed nonlinear motions. Representative results obtained through the analysis [9, 10, 11] are shown in Figure 3. These results are in good agreement with the corresponding experimental observations. A more full discussion of the analysis is provided in the papers [10, 11] included at the end of this report.

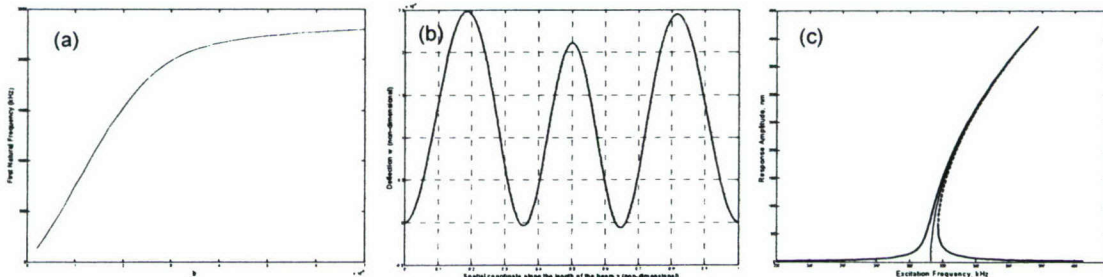


**Figure 3:** (a) First natural frequency versus  $b$  of the 200  $\mu\text{m}$  PZT resonator around the fifth static buckling mode, (b) Predicted spatial pattern when  $b = 4.65 \times 10^{-4}$ , where the corresponding natural frequency is 334 kHz, and (c) Analytical prediction for the frequency-response curve when  $b = 4.65 \times 10^{-4}$ ,  $\hat{p} = 4.65 \times 10^{-5}$ , and  $\hat{\mu} = 8.23 \times 10^{-4}$ ; the solid line represents the stable branch and dashed line represents the unstable branch.

## 4. Experimental System Identification

The investigators have been able to use experimentally obtained nonlinear frequency-response data to determine the linear and nonlinear parameters governing a micro-resonator [12, 13]. Representative results are shown in Figure 4. Through this work, the different parameters such as modal mass, linear stiffness, nonlinear stiffness, equivalent damping coefficient, modal forcing, and residual stress are identified for a microresonator excited close to its first natural frequency. The variations of these parameters with respect to the operating conditions have also been studied. Full details of the identification scheme are included in the paper [13], which is included at the end of this report.

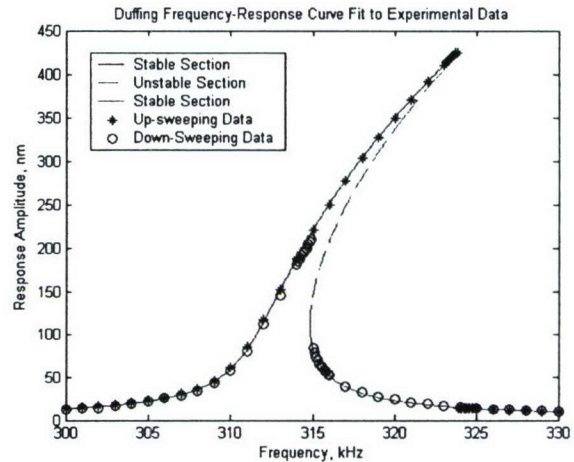


*Figure 4: Experimental data fit compared with prediction from forced Duffing model.*

## 5. Analyses of Microresonator Arrays

Both linear and nonlinear analyses have been carried out to determine the responses of micro-resonator arrays to different excitation conditions. In the linear analysis [e.g., 8], the admittance functions of clamped-clamped AlGaAs resonator arrays (e.g., Figure 5) is being studied to aid the analysis and design of these devices.

In the nonlinear analyses [14], the authors have recently examined the possibility of realizing intrinsic localized modes (ILMs) in micro-resonator arrays. The hypothesis that these modes may be forced nonlinear vibration modes of a resonator array has been analytically and numerically studied, and it has been shown that can be realized as forced nonlinear vibration modes. Additional details on this analysis is included in the paper [14] included with this report.

## 6. Summary

It is believed that the numerical and analytical efforts discussed in this report can be used as a basis to understand nonlinear phenomena such as dynamic buckling and nonlinear vibration modes in composite microscale resonators and resonator arrays, parametrically identify microresonators, and develop semi-analytical design tools for microresonators and microresonator arrays. The present work can help take advantage of nonlinearities for designing RF filters, mixers, switches, signal processors, and other MEMS devices.

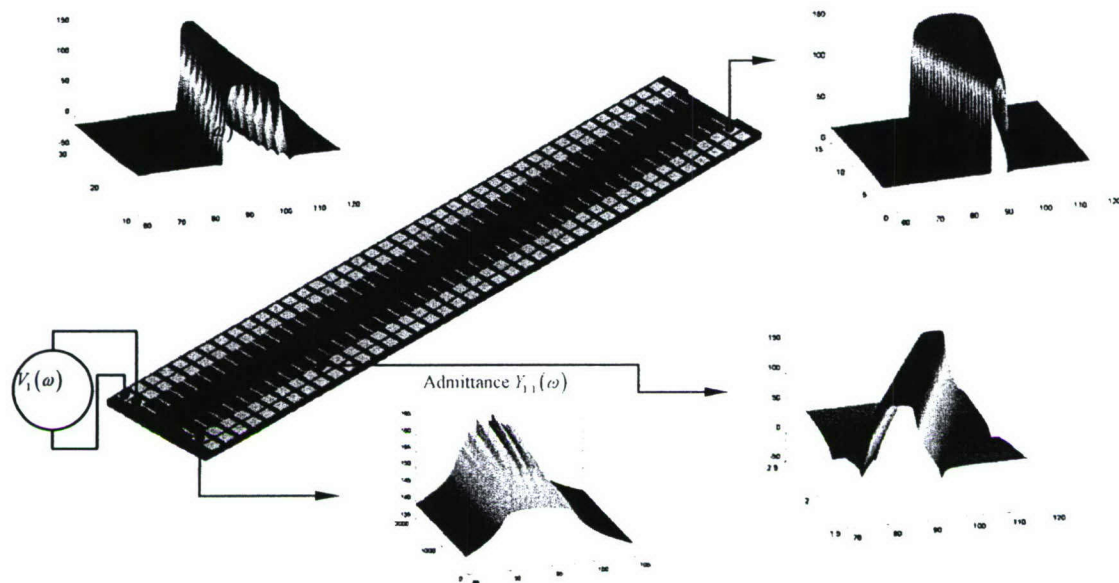


**Figure 5:** Illustrative plots of the admittance functions at different output ports of a microresonator array with respect to different system parameters.

## 7. References

- [1] DeVoe, D. L., "Piezoelectric Thin Film Micromechanical Beam Resonators," *Sensors and Actuators A (Physical)*, Vol. 88, 263-272, 2001.
- [2] Li, H. and Balachandran, B., "Buckling Induced Nonlinear Phenomenon in a Micro-electromechanical Resonator," *Proceedings of the ASME International Mechanical Engineering Congress and Exposition*, New Orleans, 2002; Paper No. IMECE2002-39010.
- [3] Balachandran, B. and Li, H., "Nonlinear Phenomena in Microelectromechanical Resonators," *Proceedings of IUTAM Symposium on Chaotic Dynamics and Control of Systems and Processes in Mechanics*, Rome, Italy, June 8-13, 2003.
- [4] Li, H. and Balachandran, B., "Nonlinear Oscillations of Micromechanical Oscillators," *Proceedings of the ASME International Design Engineering Technical Conferences*, Chicago, 2003; Paper No. DETC2003/VIB-48520.
- [5] Preidikman, S., Li, H., and Balachandran, B., "Forced Oscillations of Microelectromechanical Resonators," *Proceedings of the ASME International Mechanical Engineering Congress and Exposition*, Washington, D. C., 2003; Paper No. IMECE2003-44552.
- [6] Nayfeh, A. H. and Balachandran, B., *Applied Nonlinear Dynamics: Analytical, Computational, and Experimental Methods*, John Wiley & Sons, Inc., New York, 1995.
- [7] Preidikman, S. and Balachandran, B., "Computational Multi-Field Mechanics Model of Piezoelectric Micro-resonators," in *Smart Structures and Materials 2005: Modeling, Signal Processing, and Control*, R. C. Smith, ed., *Proc. SPIE* 5757, pp. 18-29, 2005.

- [8] Preidikman, S. and Balachandran, B., "A Semi-analytical Tool Based on Geometric Nonlinearities for Microresonator Design," *J. Micromechanics and Microengineering*, Vol. 16, 512-525, 2006.
- [9] Li, H., Preidikman, S. and Balachandran, B. "Nonlinear Forced Oscillations of Piezoelectric Resonators," in *Smart Structures and Materials 2005: Modeling, Signal Processing, and Control*, R. C. Smith, ed., *Proc. SPIE 5757*, pp. 30-41, 2005.
- [10] Li, H. and Balachandran, B., "Buckling and Free Oscillations of Composite Microresonators," *IEEE Journal of MEMS*, Vol. 15 (No. 1), 42-51, 2006.
- [11] Li, H., Preidikman, S., Balachandran, B., and Mote Jr., C. D., "Nonlinear Free and Forced Oscillations of Piezoelectric Microresonators," *J. Micromechanics and Microengineering*, Vol. 16, 356-367, 2006.
- [12] Dick, A., Balachandran, B., DeVoe, D., and Mote Jr., C. D. "Parametric Identification of Piezoelectric Micro-Scale Resonators," *Proceedings of the Fifth EUROMECH Nonlinear Dynamics Conference*, Eindhoven, The Netherlands, August 2005, Paper No. 239.
- [13] Dick, A., Balachandran, B., DeVoe, D., and Mote Jr, C. D. "Parametric Identification of Piezoelectric Micro-Scale Resonators," *J. Micromechanics and Microengineering*, Vol. 16, 1593-1601, 2006.
- [14] Dick, A., Balachandran, B., and Mote Jr, C. D. "Intrinsic Localized Modes and Nonlinear Normal Modes in Micro-Resonator Arrays," *Proceedings of the 2005 ASME International Mechanical Engineering Congress and Exposition*, Orlando, Florida, November 2005, Paper No. IMECE2005-80255.

## 8. Research Participants

1. B. Balachandran, Professor and PI
2. D. DeVoe, Associate Professor and co-PI
3. S. Preidikman, Visiting Faculty
4. H. Li, Graduate Student (Completed Doctoral studies in 2006)
5. A. Dick, Graduate Student (To complete doctoral studies in FALL 2006/SPRING 2007)

## 9. Interactions and Transitions

During the course of this research activity, the principal investigator has visited and interacted with researchers at AFRL/MNMF Program (Mr. Jason Foley, AFRL, Eglin AFB, Florida) and discussed modelling issues and the relevance of considering nonlinearities for the SiC MEMs. The research results have also been disseminated through conference presentations, conference proceeding papers, and journal publications, which are listed in Section 9. Other interactions include those conducted with researchers in the RF MEMS Group of the Army Research Laboratory, Adelphi, Maryland and those pursued through the DARPA NMA SP program.

## 10. Publications and Presentations from this Work

- [1] Li, H. and Balachandran, B., "Buckling Induced Nonlinear Phenomenon in a Micro-electromechanical Resonator," *Proceedings of the ASME International Mechanical Engineering Congress and Exposition*, New Orleans, 2002; Paper No. IMECE2002-39010.
- [2] Balachandran, B. and Li, H., "Nonlinear Phenomena in Microelectromechanical Resonators," *Proceedings of IUTAM Symposium on Chaotic Dynamics and Control of Systems and Processes in Mechanics*, Rome, Italy, June 8-13, 2003.
- [3] Li, H. and Balachandran, B., "Nonlinear Oscillations of Micromechanical Oscillators," *Proceedings of the ASME International Design Engineering Technical Conferences*, Chicago, 2003; Paper No. DETC2003/VIB-48520.
- [4] Preidikman, S., Li, H., and Balachandran, B., "Forced Oscillations of Microelectromechanical Resonators," *Proceedings of the ASME International Mechanical Engineering Congress and Exposition*, Washington, D. C., 2003; Paper No. IMECE2003-44552.
- [5] Balachandran, B. and Preidikman, S., "Oscillations of Piezoelectric Microscale Resonators," in *Progress in Computational Structures Technology*, Chapter 13, pp. 327—352, Saxe-Coburg Publications, Stirling, Scotland.
- [6] Balachandran, B., "Oscillations of Micro-Scale Resonators," *Proceedings of the Fourth International Conference on Smart Materials, Structures, and Systems*, Bangalore, India, July 2005, Paper No. SE01.
- [7] Dick, A., Balachandran, B., DeVoe, D., and Mote Jr., C. D. "Parametric Identification of Piezoelectric Micro-Scale Resonators," *Proceedings of the Fifth*

- EUROMECH Nonlinear Dynamics Conference*, Eindhoven, The Netherlands, August 2005, Paper No. 239.
- [8] Dick, A., Balachandran, B., and Mote Jr, C. D. "Intrinsic Localized Modes and Nonlinear Normal Modes in Micro-Resonator Arrays," *Proceedings of the 2005 ASME International Mechanical Engineering Congress and Exposition*, Orlando, Florida, November 2005, Paper No. IMECE2005-80255.
- [9] Li, H., Preidikman, S. and Balachandran, B. "Nonlinear Forced Oscillations of Piezoelectric Resonators," in *Smart Structures and Materials 2005: Modeling, Signal Processing, and Control*, R. C. Smith, ed., *Proc. SPIE* 5757, pp. 30-41, 2005.
- [10] Preidikman, S. and Balachandran, B., "Computational Studies of Piezoelectric Micro-Resonator Arrays," *Presented at the 2005 ASME International Mechanical Engineering Congress and Exposition*, Orlando, Florida, November 2005.
- [11] Preidikman, S. and Balachandran, B., "Computational Multi-Field Mechanics Model of Piezoelectric Micro-resonators," in *Smart Structures and Materials 2005: Modeling, Signal Processing, and Control*, R. C. Smith, ed., *Proc. SPIE* 5757, pp. 18-29, 2005.
- [12] Dick, A., Balachandran, B., and Mote Jr., C. D. "Nonlinear Vibration Modes in Micro-Resonator Arrays," in *Smart Structures and Materials 2006: Modeling, Signal Processing, and Control*, *Proc. SPIE* 6166, Paper No. 6166-24.
- [13] Dick, A., Balachandran, B., DeVoe, D., and Mote Jr, C. D. "Parametric Identification of Piezoelectric Micro-Scale Resonators," *J. Micromechanics and Microengineering*, Vol. 16, 1593-1601, 2006.
- [14] Li, H. and Balachandran, B., "Buckling and Free Oscillations of Composite Microresonators," *IEEE Journal of MEMS*, Vol. 15 (No. 1), 42-51, 2006.
- [15] Li, H., Preidikman, S., Balachandran, B., and Mote Jr., C. D., "Nonlinear Free and Forced Oscillations of Piezoelectric Microresonators," *J. Micromechanics and Microengineering*, Vol. 16, 356-367, 2006.
- [16] Preidikman, S. and Balachandran, B., "A Semi-analytical Tool Based on Geometric Nonlinearities for Microresonator Design," *J. Micromechanics and Microengineering*, Vol. 16, 512-525, 2006.

## **11. Invention Disclosures**

1. Dick, A. and Balachandran, B., "MEMS Accelerometer for High Acceleration Levels and Extreme Environments, *University of Maryland Invention Disclosure PS-2005-086*.

# Buckling and Free Oscillations of Composite Microresonators

He Li and B. Balachandran, *Fellow, ASME*

**Abstract**—Free oscillations of piezoelectric, microelectromechanical resonators are considered in this effort. These resonators are modeled as clamped-clamped composite structures, with stepwise varying properties across the length of the resonator. The different features of the model development are discussed, and buckling in these resonators is studied. A nonlinear analysis conducted to study oscillations about a buckled position is presented. The results of the analysis are found to compare well with the experimental observations. [1482]

**Index Terms**—Buckled beam, clamped-clamped piezoelectric resonator structure, dynamic buckling, microelectromechanical systems (MEMS) resonator.

## I. INTRODUCTION

OSCILLATIONS of microelectromechanical resonators fabricated as clamped-clamped composite structures are studied here. These microresonators, which are to be used as filters, are important for mobile communication systems and signal processing applications (e.g., Fourier transform computations) [1]. Analytical studies of the nonlinear dynamic response of electrostatically actuated microresonators modeled as beam-like structures have been recently carried out [2]. The resonators considered in this effort are based on the piezoelectric effect, as shown in Fig. 1. The elastic substrate is a SiO<sub>2</sub> layer, and on the top of this layer, a platinum electrode layer is deposited throughout the length of the structure. A thin layer of sol-gel piezoelectric film is located on the top of this electrode layer. To complete the structure, the top layer is a platinum electrode layer that extends over one quarter of the length from each anchor [3], [4]. Each resonator structure has three layers in the mid-span where the top electrode layer is absent and four layers elsewhere. Due to the asymmetry of the cross section, the position of the piezoelectric layer is offset from the neutral axis, and in addition, residual stress may also be introduced in each layer during the manufacturing process.

Here, the resonators considered typically range in lengths from 100  $\mu\text{m}$  to 400  $\mu\text{m}$ , with a width of 20  $\mu\text{m}$  and a total thickness of about 2.3  $\mu\text{m}$ . For comparisons of model predictions with experimental results, particular attention is paid to a 200  $\mu\text{m}$  long resonator. The layer thickness values for this resonator are provided in Table I. As shown in Fig. 2, each resonator is modeled as a composite beam with stepwise axially varying

properties. The axial stiffness and bending stiffness values for a resonator considered in this study are given in Table II. The subscripts used for the different stiffness values correspond to the sections shown in Fig. 2.

## II. EXPERIMENTS AND OBSERVATIONS

For a 200- $\mu\text{m}$ -long resonator, the first natural frequency, was experimentally determined to be close to 334 kHz, while the model prediction for this resonator, without consideration of the axial force and nonflat equilibrium position, is about 186 kHz. A sketch of the experimental arrangement used to study forced oscillations of this resonator is shown in Fig. 3. A laser vibrometer is used to get a measure of the transverse vibrations at the midpoint of the resonator. The excitation signal fed into the input port of the resonator consists of a sinusoidal component close to the first natural frequency and a dc bias offset. In Fig. 4, a representative spatial response distribution of this resonator observed in the experiments is shown [4]. This spatial distribution was measured by using a scanning laser vibrometer. The experimental observations suggest that the oscillations may be taking place around a nonflat equilibrium position.

Here, the hypothesis that the nonflat equilibrium position is caused by buckling is explored to explain the experimental observation shown in Fig. 4 and accurately predict the experimentally obtained value of the first natural frequency. This hypothesis is motivated by prior work conducted with buckled microstructures [5]–[9] and large-scale structures [10], [11]. These prior studies on electrostatically actuated microstructures have by and large focused on the static case, and in addition, the modeling of the spatial information has not been carried out in the dynamic case. Furthermore, in all of the previous studies, the structures considered have a uniform section unlike the microstructures considered in the present work. Here, the piezoelectrically actuated microstructures have stepwise axially varying properties (see Table II).

To explain the response characteristics such as those shown in Fig. 4, here, the buckling of a beam with stepwise axially varying properties is studied and the free oscillations about different buckling modes are examined. The model development is presented in Section III, along with the buckling analysis and treatment of free vibrations about a buckled position. This work is of general nature and it can be used to study buckling in any composite beam with stepwise axially varying properties and free oscillations of such a structure about a buckled position. In Section IV, the model predictions for microresonators are provided, compared with experimental observations, and discussed.

Manuscript received December 10, 2004; revised October 3, 2005. This work was supported by DARPA under Contract F3060202C0016 and an AFOSR Grant F49620-03-10181. Subject Editor N. C. Tien.

The authors are with the Department of Mechanical Engineering, University of Maryland, College Park, MD 20742 USA (e-mail: lihe@wam.umd.edu; balab@eng.umd.edu).

Digital Object Identifier 10.1109/JMEMS.2005.863598

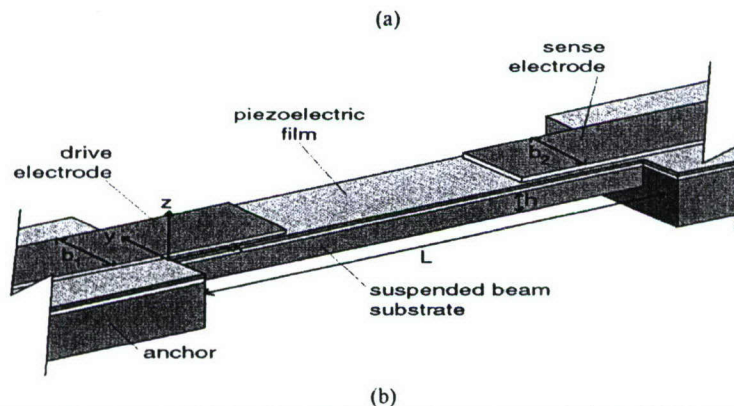
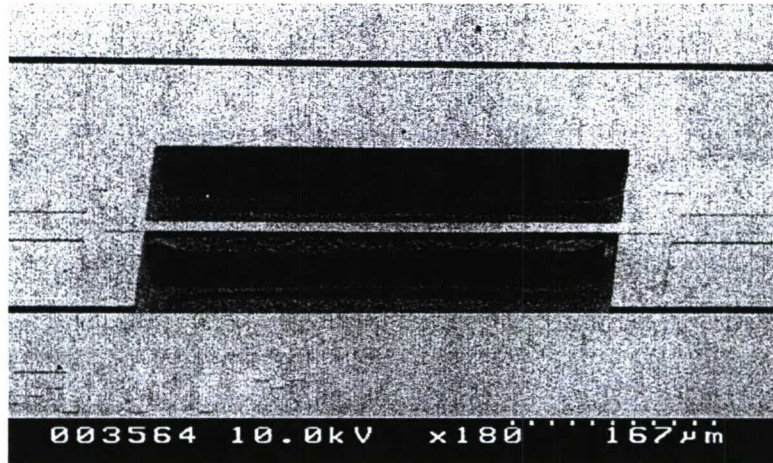


Fig. 1. Piezoelectric microresonator: (a) SEM picture of a 400- $\mu\text{m}$ -long PZT resonator (courtesy, Maryland MEMS Laboratory) and (b) schematic of piezoelectric resonator [3].

TABLE I  
LAYER THICKNESS VALUES FOR A 200  $\mu\text{m}$  COMPOSITE RESONATOR

SiO <sub>2</sub> [ $\mu\text{m}$ ]	Bottom Pt [ $\mu\text{m}$ ]	PZT [ $\mu\text{m}$ ]	Top Pt [ $\mu\text{m}$ ]
1.030	0.085	1.09	0.090

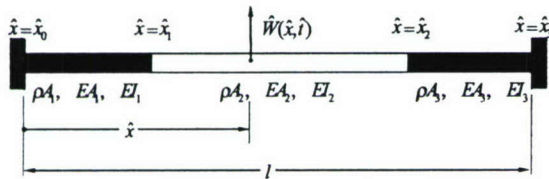


Fig. 2. Clamped-clamped composite beam with stepwise axially varying characteristics.

TABLE II  
AXIAL STIFFNESS AND BENDING STIFFNESS VALUES FOR A 200  $\mu\text{m}$  LONG RESONATOR

$EA_1$ [N]	$EA_2$ [N]	$EA_3$ [N]	$EI_1$ [N·m <sup>2</sup> ]	$EI_2$ [N·m <sup>2</sup> ]	$EI_3$ [N·m <sup>2</sup> ]
3.17	2.88	3.17	$1.39 \times 10^{-12}$	$0.83 \times 10^{-12}$	$1.39 \times 10^{-12}$

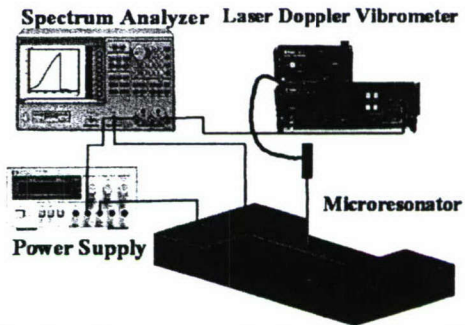


Fig. 3. Experimental arrangement showing how a laser vibrometer is positioned to examine transverse vibrations of resonator. The resonator is excited by signals input to the drive electrode.

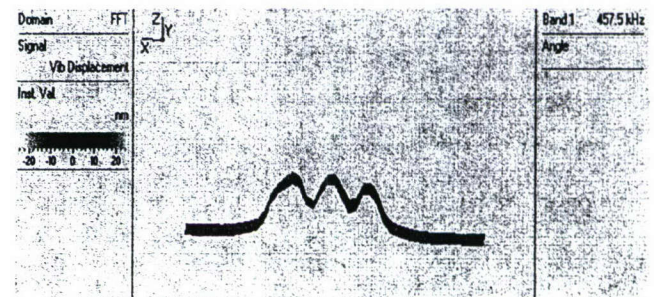


Fig. 4. Laser vibrometer measurement of a spatial pattern observed in experiments. The presence of spatial harmonics distorts the spatial pattern from the typical mode shape associated with the fundamental mode of vibration of a clamped-clamped beam [4] (courtesy, Maryland MEMS laboratory).

### III. MODELING AND QUANTITATIVE ANALYSIS

#### A. Governing Equations

In Fig. 2, a model of the resonator as a clamped-clamped beam has been presented. The axially varying properties along the resonator can be expressed in the form

$$\begin{aligned} m(\hat{x}) &= \sum_{k=1}^n m_k H_k(\hat{x}), \\ EA(\hat{x}) &= \sum_{k=1}^n EA_k H_k(\hat{x}), \\ EI(\hat{x}) &= \sum_{k=1}^n EI_k H_k(\hat{x}) \end{aligned} \quad (1)$$

where  $m_k$ ,  $EI_k$ , and  $EA_k$  are constants,  $\hat{x}$  is the spatial variable,  $H_k(\hat{x}) = [u(\hat{x} - \hat{x}_{k-1}) - u(\hat{x} - \hat{x}_k)]$  is the Heaviside function and  $u(\hat{x})$  is the unit step function, and  $n$  is the total number of beam sections, which is 3 here. The structure extends from  $\hat{x}_0 = 0$  to  $\hat{x}_n = l$ , where  $l$  is the unbuckled structure's length.

For the considered composite structures, taking into account that the length to thickness ratio is more than ten, the width is much larger than the thickness in each section, it is assumed that each section of the structure can be treated as an Euler-Bernoulli beam and the lateral displacement along the  $y$  direction of Fig. 1(b) can be ignored. Then, for initially straight beams undergoing undamped and unforced motions, the nonlinear equations of motion can be written as [12]

$$\begin{aligned} m_k \frac{\partial^2 \hat{u}_k(\hat{x}, \hat{t})}{\partial \hat{t}^2} - EA_k \frac{\partial^2 \hat{u}_k(\hat{x}, \hat{t})}{\partial \hat{x}^2} \\ = [EA_k - \hat{N}_0] \frac{\partial}{\partial \hat{x}} \left[ \left( \frac{1}{2} - \frac{\partial \hat{u}_k(\hat{x}, \hat{t})}{\partial \hat{x}} \right) \left( \frac{\partial \hat{w}_k(\hat{x}, \hat{t})}{\partial \hat{x}} \right)^2 \right], \end{aligned} \quad (2)$$

$$\begin{aligned} m_k \frac{\partial^2 \hat{w}_k(\hat{x}, \hat{t})}{\partial \hat{t}^2} - \hat{N}_0 \frac{\partial^2 \hat{w}_k(\hat{x}, \hat{t})}{\partial \hat{x}^2} + EI_k \frac{\partial^4 \hat{w}_k(\hat{x}, \hat{t})}{\partial \hat{x}^4} \\ = [EA_k - \hat{N}_0] \frac{\partial}{\partial \hat{x}} \left[ e_k(\hat{x}, \hat{t}) \frac{\partial \hat{w}_k(\hat{x}, \hat{t})}{\partial \hat{x}} \right], \end{aligned} \quad (3)$$

where the nonlinear axial strain has the form

$$\begin{aligned} e_k(\hat{x}, \hat{t}) &= \frac{d\hat{s} - d\hat{x}}{d\hat{s}} \\ &= \frac{\partial \hat{u}_k}{\partial \hat{x}} - \left( \frac{\partial \hat{u}_k}{\partial \hat{x}} \right)^2 + \frac{1}{2} \left( \frac{\partial \hat{w}_k}{\partial \hat{x}} \right)^2, \end{aligned} \quad (4)$$

In (2)–(4), the symbol  $\hat{\cdot}$  has been used to indicate a dimensional variable,  $\hat{w}_k(\hat{x}, \hat{t})$  is the transverse displacement of the beam in the  $k$ th section,  $\hat{u}_k(\hat{x}, \hat{t})$  is the displacement along  $\hat{x}$  axis in the  $k$ th section,  $\hat{t}$  is the time variable, and  $\hat{N}_0$  is the prescribed initial static axial load, which is assumed to be a constant with respect to  $\hat{x}$ . In (4),  $d\hat{x}$  is the length of a differential element of the undeformed beam and  $d\hat{s}$  is the corresponding length of a differential element of the deformed beam. For the convenience

of further analysis, the following dimensionless variables are introduced:

$$\begin{aligned} x &= \frac{\hat{x}}{l}, \quad w = \frac{\hat{w}}{l}, \quad u = \frac{\hat{u}}{l}, \\ t_k &= \frac{\hat{t}}{l^2} \sqrt{\frac{EI_k}{m_k}}, \quad N_k = \frac{\hat{N}_0 l^2}{EI_k}. \end{aligned} \quad (5)$$

In terms of the dimensionless spatial variable  $x$ , the boundaries of the structure are located at  $x_0 = 0$  and  $x_n = 1$ . By using the nondimensional variables given in (5), (2)–(4), can be written in the following form:

$$\begin{aligned} r_k^2 \frac{\partial^2 u_k}{\partial t_k^2} - \frac{\partial^2 u_k}{\partial x^2} &= [1 - r_k^2 N_k] \frac{\partial}{\partial x} \\ &\times \left[ \left( \frac{1}{2} - \frac{\partial u_k}{\partial x} \right) \right. \\ &\times \left. \left( \frac{\partial w_k}{\partial x} \right)^2 \right], \end{aligned} \quad (6)$$

$$\begin{aligned} r_k^2 \left[ \frac{\partial^2 w_k}{\partial t_k^2} - N_k \frac{\partial^2 w_k}{\partial x^2} + \frac{\partial^4 w_k}{\partial x^4} \right] &= [1 - r_k^2 N_k] \\ &\times \frac{\partial}{\partial x} \left[ e_k \frac{\partial w_k}{\partial x} \right], \end{aligned} \quad (7)$$

$$\begin{aligned} e_k(x, t_k) &= \frac{\partial u_k}{\partial x} - \left( \frac{\partial u_k}{\partial x} \right)^2 \\ &+ \frac{1}{2} \left( \frac{\partial w_k}{\partial x} \right)^2, \end{aligned} \quad (8)$$

In (6)–(8), the parameter  $r_k = (\sqrt{EI_k}/EA_k/l)$  is the slenderness ratio of the  $k$ th section of the resonator.

For the resonator with a length of 200  $\mu\text{m}$  and the stiffness values provided in Table II, the  $k$ th section's slenderness ratio  $r_k$  is of the order of  $10^{-3}$ ; this means that the longitudinal inertia term is small compared to the longitudinal stiffness term in (6). Here, based on the small value of the slenderness ratio, it is assumed that  $u_k = O(w_k^2)$  [12]. Then, (8) can be reduced to

$$e_k = \frac{\partial u_k}{\partial x} + \frac{1}{2} \left( \frac{\partial w_k}{\partial x} \right)^2 + \dots \quad (9)$$

Dropping the terms with  $r_k$  and the cubic terms, (6) can be integrated with respect to the spatial variable to obtain

$$-\frac{\partial u_k}{\partial x} = \frac{1}{2} \left( \frac{\partial w_k}{\partial x} \right)^2 - \varepsilon_k(t_k). \quad (10)$$

From (10), it is noted that the displacement  $u_k$  can be regarded as a quasi-static motion, and that the expression for  $\varepsilon_k$  is equivalent to the expression for  $e_k$  in (9), which has the same form as the Green–Lagrange strain  $\varepsilon_{11}$  [13]. Spatially integrating (10) one more time and evaluating the resulting expression at  $x = x_k$ ,  $\varepsilon_k$  can be determined as

$$\begin{aligned} \varepsilon_k(t_k) &= \frac{u_k(x_k, t_k) - u_k(x_{k-1}, t_k)}{(x_k - x_{k-1})} \\ &+ \frac{1}{2(x_k - x_{k-1})} \int_{x_{k-1}}^{x_k} \left( \frac{\partial w_k}{\partial x} \right)^2 dx, \end{aligned} \quad (11)$$

$k = 1, 2, \dots, n.$

From (10), it had been noted that  $\varepsilon_k$  is constant with respect to  $x$ . Based on this observation, the force equilibrium condition at the interconnection of any two adjacent sections requires that the axial load due to this strain is constant among all of the sections; that is

$$\hat{Q}(\hat{t}) = EA_k \varepsilon_k(\hat{t}). \quad (12)$$

After substituting (11) for  $e_k$  into (7) and simplifying, the resulting equation of motion governing the transverse vibrations of the microresonator with stepwise axially varying properties is obtained as

$$\begin{aligned} & \frac{\partial^2 w_k}{\partial t_k^2} + \frac{\partial^4 w_k}{\partial x^4} \\ & - \left[ N_k(t_k) + \frac{u_k(x_k, t_k) - u_k(x_{k-1}, t_k)}{r_k^2(x_k - x_{k-1})} \right. \\ & \quad \left. + \frac{1}{2r_k^2(x_k - x_{k-1})} \int_{x_{k-1}}^{x_k} \left( \frac{\partial w_k}{\partial x} \right)^2 dx \right] \frac{\partial^2 w_k}{\partial x^2} = 0, \\ & k = 1, 2, \dots, n. \end{aligned} \quad (13)$$

For the particular case of a clamped-clamped resonator, the associated boundary conditions are

$$w(x, t) = 0 \text{ and } \frac{\partial w(x, t)}{\partial x} = 0 \text{ at } x = 0 \text{ and } x = 1. \quad (14)$$

The governing equation given by (13) is different from that treated in previous work [10], [11], since the resonator has axially varying properties. This equation along with the boundary conditions represents a nonlinear model that can be used to study transverse vibrations of a beam with stepwise axially varying properties and sections that have ‘‘small’’ slenderness-ratio values.

### B. Static Buckling Problem

To solve (13), the static buckling problem is first addressed. It is assumed that the dimensionless static buckling deflection of the resonator can be expressed as

$$\begin{aligned} \chi(x) &= \sum_{k=1}^n \chi_k(x) H_k(x) \\ \pi(x) &= \sum_{k=1}^n \pi_k(x) H_k(x) \end{aligned} \quad (15)$$

where  $\chi_k(x)$  and  $\pi_k(x)$  are the transverse and axial displacement of the  $k$ th section of the beam, respectively. For the static buckling analysis, the inertia term in (13) is dropped, and the static compressive axial forces  $-\hat{P}_0$  and  $-P_{0,k}$  are substituted for  $\hat{N}_0$  and  $N_k$  respectively in (5) and (13). After carrying these substitutions through, the nonlinear equation governing the equilibrium of the beam subjected to a static axial force can be written as

$$\begin{aligned} & \frac{d^4 \chi_k}{dx^4} + \left[ P_{0,k} - \frac{\pi_k(x_k) - \pi_k(x_{k-1})}{r_k^2(x_k - x_{k-1})} \right. \\ & \quad \left. - \frac{1}{2r_k^2(x_k - x_{k-1})} \int_{x_{k-1}}^{x_k} \left( \frac{d\chi_k}{dx} \right)^2 dx \right] \\ & \quad \times \frac{d^2 \chi_k}{dx^2} = 0, \quad k = 1, 2, \dots, n. \end{aligned} \quad (16)$$

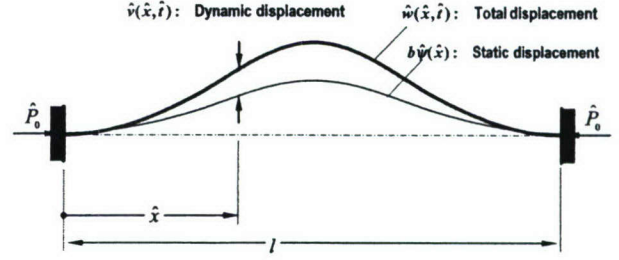


Fig. 5. Buckled beam configuration.

The associated boundary conditions follow from (14) as

$$\chi(x) = 0 \text{ and } \frac{d\chi(x)}{dx} = 0 \text{ at } x = 0 \text{ and } x = 1. \quad (17)$$

In order to obtain the solution of (16), the critical buckling force must be first calculated by attacking the linear buckling problem for this composite resonator with axially varying properties. To this end, after switching to the dimensional variable  $\hat{x}$ , the critical buckling configuration  $\hat{\psi}(\hat{x})$  is determined with respect to the applied critical axial load  $\hat{P}_c$ . First, it is assumed that

$$\hat{\psi}(\hat{x}) = \sum_{k=1}^n \hat{\psi}_k(\hat{x}) H_k(\hat{x}). \quad (18)$$

Then, noting that each of the  $k$  sections has uniform properties, the linear static buckling problem is written as

$$EI_k \frac{d^4 \hat{\psi}_k}{d\hat{x}^4} + \hat{P}_c \frac{d^2 \hat{\psi}_k}{d\hat{x}^2} = 0, \quad k = 1, 2, \dots, n. \quad (19)$$

Introducing the dimensionless variables from (5) into (19) results in

$$\frac{d^4 \psi_k}{dx^4} + \zeta_k^2 \frac{d^2 \psi_k}{dx^2} = 0, \quad k = 1, 2, \dots, n \quad (20)$$

where  $\zeta_k^2 = P_{c,k} = (\hat{P}_c l^2 / EI_k)$ . The general solution of (20) is given by

$$\psi_k(x) = a_{1,k} + a_{2,k}x + a_{3,k} \cos(\zeta_k x) + a_{4,k} \sin(\zeta_k x). \quad (21)$$

To determine the arbitrary constants  $a_{j,k}$  for  $j = 1, 2, 3, 4$  and  $k = 1, 2, \dots, n$ , the following boundary conditions for a clamped-clamped beam are used

$$\begin{aligned} \psi_1(x) &= 0 \text{ and } \frac{d\psi_1(x)}{dx} = 0 \text{ at } x = x_0, \\ \psi_n(x) &= 0 \text{ and } \frac{d\psi_n(x)}{dx} = 0 \text{ at } x = x_n. \end{aligned} \quad (22)$$

In addition, as the beam is a continuous system, two adjacent sections have to share the same transverse displacement, same slope, same bending moment, and same shear force at the respective connection point. This leads to the following nondimensional form of the compatibility conditions [14]

$$\begin{aligned} & \psi_{k-1}(x) = \psi_k(x), \\ & \frac{d\psi_{k-1}(x)}{dx} = \frac{d\psi_k(x)}{dx}, \\ & EI_{k-1} \frac{d^2 \psi_{k-1}(x)}{dx^2} = EI_k \frac{d^2 \psi_k(x)}{dx^2}, \\ & EI_{k-1} \frac{d^3 \psi_{k-1}(x)}{dx^3} = EI_k \frac{d^3 \psi_k(x)}{dx^3} \\ & \text{at } x = x_{k-1}, \quad k = 2, 3, \dots, n. \end{aligned} \quad (23)$$

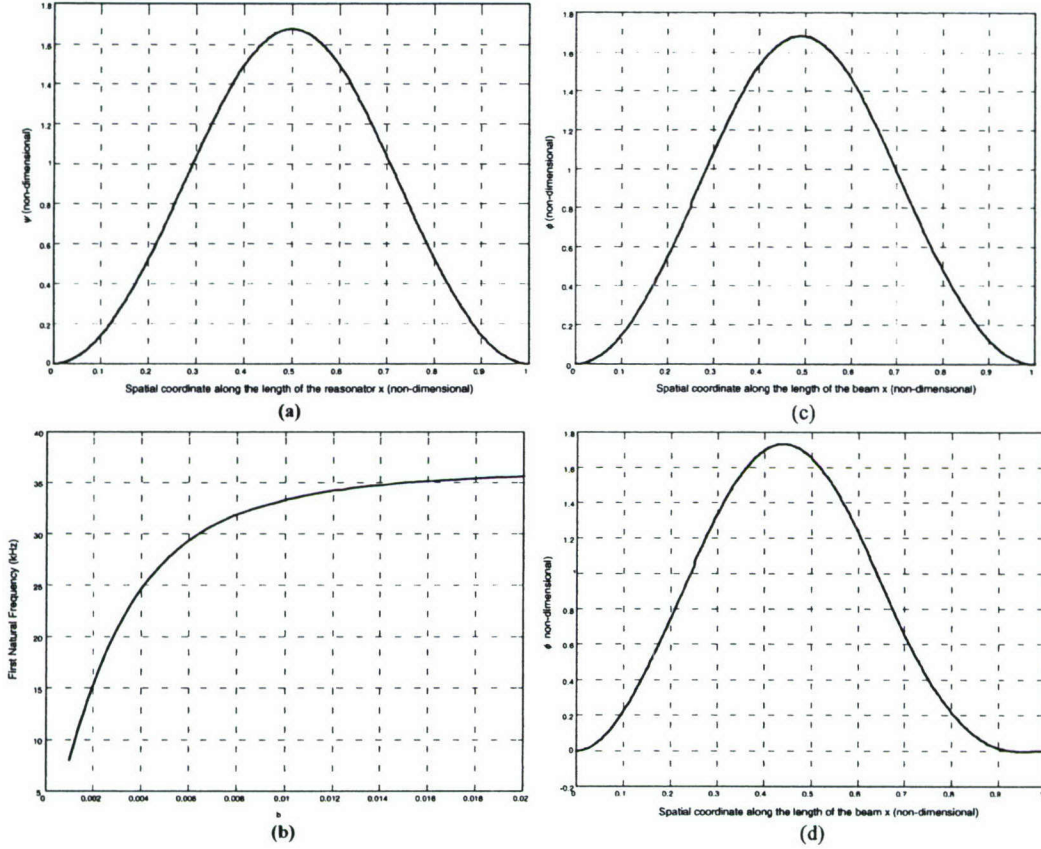


Fig. 6. (a) First static buckling mode shape of the 200  $\mu\text{m}$  PZT resonator, (b) first natural frequency versus  $b$ , (c) first mode shape of free vibration about first buckling mode for  $b = 0.001$ , and (d) first mode shape of free vibration about first buckling mode for  $b = 0.02$ .

For  $n = 3$ , after substituting (21) into (22) and (23), one obtains a set of twelve homogeneous algebraic equations that defines an eigenvalue problem for the  $a_{j,k}$  and the eigenvalues  $\zeta_k$ . It is important to note here from the definition of  $\zeta_k$  provided in the context of (20), that the different eigenvalues are functions of the critical buckling force. From (9) and (12), it is noted that in the  $k$ th section, the axial displacement  $\vartheta_k$ , the transverse displacement  $\psi_k$  and the longitudinal extension measure  $e_{c,k}$  have to satisfy

$$e_{c,k} = \frac{\partial \vartheta_k}{\partial x} + \frac{1}{2} \left( \frac{\partial \psi_k}{\partial x} \right)^2 \quad (24)$$

$$\hat{Q}_c(\hat{t}) = EA_k e_{c,k}(\hat{t}). \quad (25)$$

After calculating the critical buckling force, the post-buckling problem is considered. When the compressive axial force is larger than the critical buckling force, the linear buckling problem given by (20) cannot be used to study the beam's deformation. The nonlinear equation given by (16) needs to be considered.

For solving (16), it is assumed that

$$\chi_k(x) = b_k \psi_k(x), \quad k = 1, 2, \dots, n \quad (26)$$

where  $b_k$  is a nondimensional factor, which is called the buckling factor. This factor is a measure of the amplitude of the

post-buckling deformation with respect to the shape of the critical buckling mode. From (9) and (24) along with (26), one can obtain that

$$\begin{aligned} \pi_k &= b_k^2 \vartheta_k \\ e_k &= b_k^2 e_{c,k}. \end{aligned} \quad (27)$$

Next substitution of (20), (24), and (26) into (16) results in

$$b_k^2 = \frac{\tau_k^2 (P_{0,k} - P_{c,k})}{e_{c,k}}, \quad k = 1, 2, \dots, n. \quad (28)$$

After substituting (25) into (28), and returning to dimensional variables, it is found that  $b_k$  is the same constant with respect to  $\hat{x}$  for all the sections; that is

$$b^2 = \frac{(\hat{P}_0 - \hat{P}_c)}{\hat{Q}_c}. \quad (29)$$

Therefore, the solution of (16) and (27) becomes

$$\begin{aligned} \chi_k(x) &= b \psi_k(x), \\ \pi_k(x) &= b^2 \vartheta_k(x), \\ e_k &= b^2 e_{c,k}, \quad k = 1, 2, \dots, n. \end{aligned} \quad (30)$$

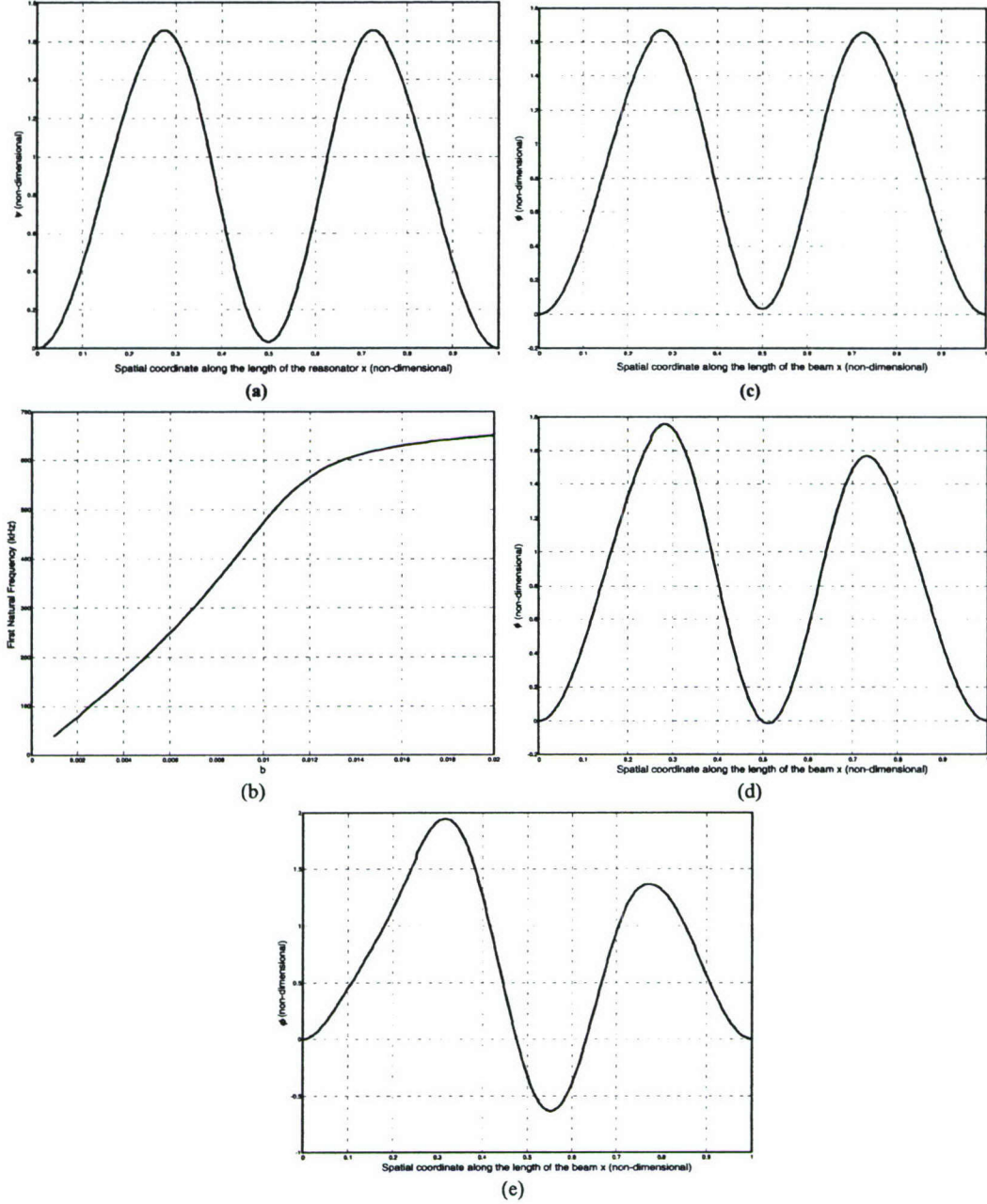


Fig. 7. (a) The third static buckling mode shape of the  $200\ \mu\text{m}$  PZT resonator, (b) first natural frequency versus  $b$ , (c) first mode shape of free oscillation about third buckling mode for  $b = 0.001$ , (d) first mode shape of free oscillation about third buckling mode for  $b = 0.004$ , and (e) first mode shape of free oscillation about third buckling mode for  $b = 0.01$ .

### C. Free Linear Vibrations About the Postbuckled Position

Free oscillations of the undamped resonator modeled as a beam with stepwise axially varying properties are considered in this section. The equation of motion and the corresponding boundary conditions for an undamped, unforced beam subjected to an axial load are given by (13) and (14). The solution of this system can be written as the sum of a static component and a dynamic component [5] (see Fig. 5)

$$\begin{aligned} w_k(x, t_k) &= b\psi_k(x) + v_k(x, t_k), \\ u_k(x, t_k) &= b^2\vartheta_k(x) + f_k(x, t_k), \quad k = 1, 2, \dots, n \end{aligned} \quad (31)$$

where  $v_k(x, t_k)$  and  $f_k(x, t_k)$  are the  $k$ th component of the dynamic deflection,  $\psi_k(x)$  and  $\vartheta_k(x)$  are the  $k$ th component of the static buckling mode shape  $\psi(x)$  and  $\vartheta(x)$ , respectively, and  $b$  is the buckling level factor defined by (29).

Next, the natural frequencies  $\hat{\omega}$  and mode shapes associated with free oscillations around the postbuckled position  $b\psi(x)$  are examined. To find the natural frequencies and mode shapes from (13), (31) is substituted into (13). It is assumed that  $|v_k(x, t_k)| \ll |b\psi_k(x)|$ ,  $f_k = O(v_k^2)$ , and the separation of variables is used to express the solution as

$$v_k(x, t_k) = \phi_k(x)e^{i\omega_k t_k} \quad (32)$$

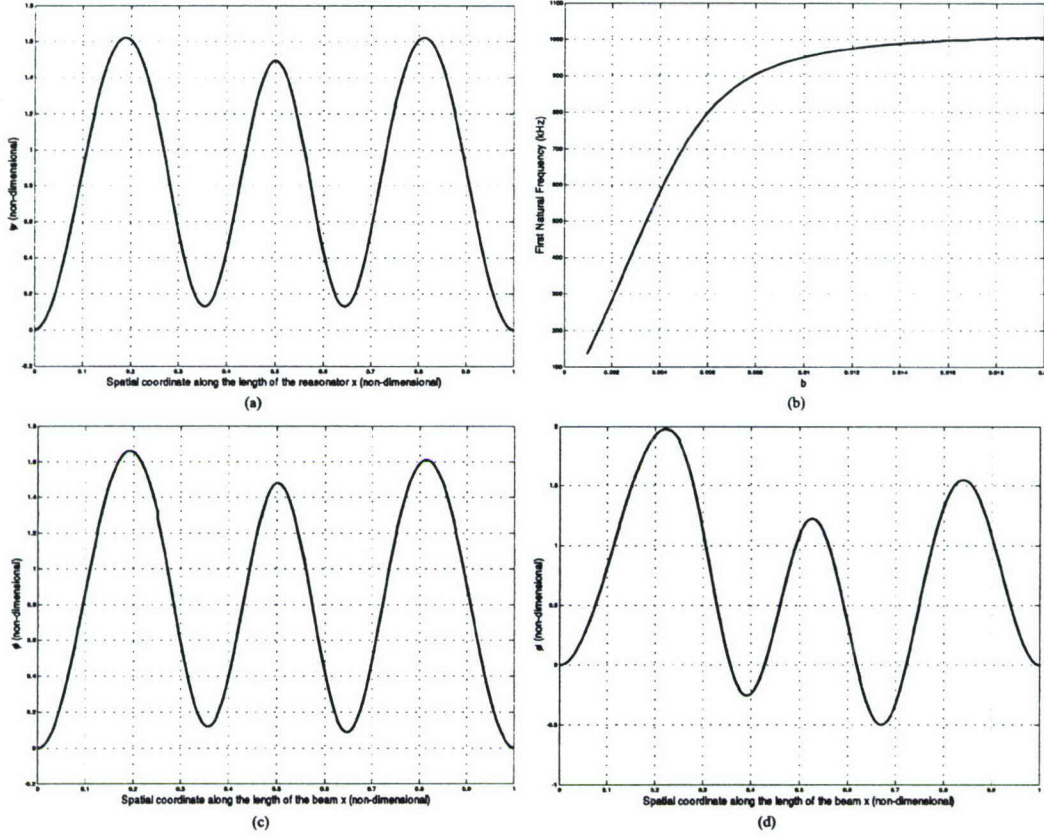


Fig. 8. (a) The fifth static buckling mode shape of the 200  $\mu\text{m}$  PZT resonator, (b) first natural frequency versus  $b$ , (c) first mode shape of free oscillation about fifth buckling mode for  $b = 0.001$ , and (d) first mode shape of free oscillation about fifth buckling mode for  $b = 0.005$ .

where  $\phi_k(x)$  is the mode shape and  $\omega_k = \sqrt{(m_k/EI_k)l^2\hat{\omega}}$  is the nondimensional quantity associated with section  $k = 1, 2, \dots, n$ . Making use of (20), (13), and (32), the following equation is obtained:

$$\begin{aligned}
 & -\omega_k^2\phi_k + P_{c,k}\frac{d^2\phi_k}{dx^2} + \frac{d^4\phi_k}{dx^4} \\
 & = \frac{EA_k l^2 b^2}{EI_k(x_k - x_{k-1})} \frac{d^2\psi_k}{dx^2} \int_{x_{k-1}}^{x_k} \left[ \frac{d\psi_k}{dx} \frac{d\phi_k}{dx} \right] dx \\
 & k = 1, 2, \dots, n.
 \end{aligned} \quad (33)$$

The general solution of (33) is composed of a homogeneous solution  $\phi_{h,k}(x)$  and a particular solution  $\phi_{p,k}(x)$ ; that is,

$$\phi_k(x) = \phi_{h,k}(x) + \phi_{p,k}(x). \quad (34)$$

As in the critical buckling case, the spatial displacement term  $\phi_k(x)$  has to satisfy the boundary conditions and the compatibility conditions that are similar to those given by (22) and (23). The homogeneous solution is given by

$$\begin{aligned}
 \phi_{h,k}(x) = & C_{1,k} \sin(\lambda_{1,k}x) + C_{2,k} \cos(\lambda_{1,k}x) \\
 & + C_{3,k} \sinh(\lambda_{2,k}x) + C_{4,k} \cosh(\lambda_{2,k}x)
 \end{aligned} \quad (35)$$

where

$$\begin{aligned}
 \lambda_{1,k} & = \sqrt{\frac{1}{2} \left( P_{c,k} + \sqrt{P_{c,k}^2 + 4\omega_k^2} \right)}, \\
 \lambda_{2,k} & = \sqrt{\frac{1}{2} \left( -P_{c,k} + \sqrt{P_{c,k}^2 + 4\omega_k^2} \right)}.
 \end{aligned} \quad (36)$$

After substituting (34) and (35) into (33), the differential equation governing the particular solution  $\phi_{p,k}(x)$  is obtained as

$$\begin{aligned}
 & -\omega_k^2\phi_{p,k} + \frac{d^4\phi_{p,k}}{dx^4} + P_{c,k}\frac{d^2\phi_{p,k}}{dx^2} \\
 & - \frac{EA_k l^2 b^2}{EI_k(x_k - x_{k-1})} \frac{d^2\psi_k}{dx^2} \int_{x_{k-1}}^{x_k} \left[ \frac{d\psi_k}{dx} \frac{d\phi_{p,k}}{dx} \right] dx \\
 & = \frac{EA_k l^2 b^2}{EI_k(x_k - x_{k-1})} \frac{d^2\psi_k}{dx^2} \int_{x_{k-1}}^{x_k} \left[ \frac{d\psi_k}{dx} \frac{d\phi_{h,k}}{dx} \right] dx.
 \end{aligned} \quad (37)$$

It follows that the solution of (37) can be written as

$$\phi_{p,k}(x) = C_{5,k} [a_{3,k} \cos(\zeta_k x) + a_{4,k} \sin(\zeta_k x)] \quad (38)$$

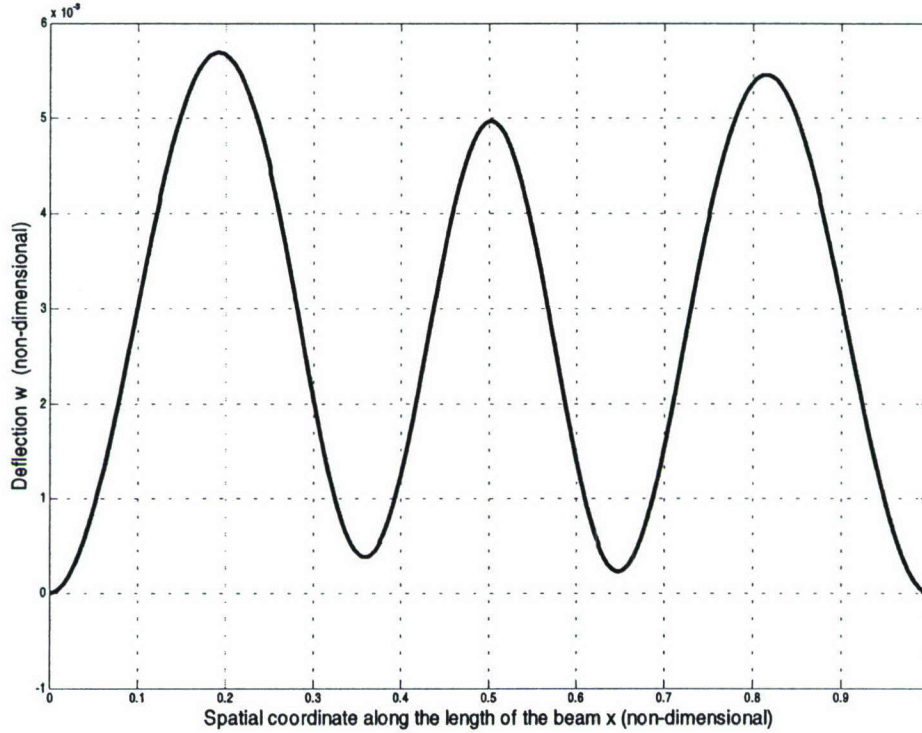


Fig. 9. Predicted spatial pattern for  $b = 0.00235$ , where the corresponding natural frequency is 333 kHz.

where the  $C_{5,k}$  are constants. Making use of (37) and (38), the relations between the constants  $C_{j,k}$ ,  $j = 1, 2, \dots, 5$  are obtained as

$$B_{1,k}C_{1,k} + B_{2,k}C_{2,k} + B_{3,k}C_{3,k} + B_{4,k}C_{4,k} + B_{5,k}C_{5,k} = 0 \quad (39)$$

where the  $B_{j,k}$  s are defined in Appendix I. Equation (39) constitutes an eigenvalue problem for the  $C_{j,k}$  and the natural frequencies  $\omega_k$ . After determining these values for  $C_{j,k}$ , the expression for the free vibration mode shape of the postbuckled beam with stepwise axially varying properties can be written as

$$\phi(x) = \sum_{k=1}^n \phi_k(x)H_k(x). \quad (40)$$

#### IV. RESULTS AND DISCUSSION

For the 200- $\mu\text{m}$ -long resonator discussed in Sections I and II, the different buckling modes determined for different levels of the  $b$  factor are shown in Figs. 6–9. The shapes are similar to those determined at the macroscale for other structures [10].

As discussed in Section II, the first natural frequency of a 200- $\mu\text{m}$ -long resonator was determined as 334 kHz [4]. The amplitude of the forced oscillation was determined to be in the range of 100 nm to 1  $\mu\text{m}$  depending on the drive voltage amplitude of the sinusoidal signal. In Fig. 8(b), the variation of the first natural frequency versus the scaling parameter  $b$  is shown

for free oscillations about the fifth buckling mode of the resonator. When  $b$  is equal to 0.00235, the first natural frequency of the resonator is determined from the model as 333 kHz, which is close to the experimental result; it is important to note that for the same frequency value, the corresponding value of  $b$  depends on the beam stiffness and geometric properties as well as how one scales the static critical buckling mode shape. In this work, the buckling factor  $b$  is obtained by normalizing the nondimensional static critical buckling mode shape  $\psi$ , so that its inner product over the nondimensional variable running from 0 to 1 is 1. The corresponding deflection  $w = (b\psi + \phi)$  is shown in Fig. 9. In this figure, the amplitude value of  $\phi$  is tuned to be  $10^{-3}$ , so that the highest displacement over the spatial coordinate is 200 nm. This free oscillation mode shape is similar to the spatial patterns observed during forced oscillations when the excitation frequency is close to the first natural frequency of the resonator (see Fig. 4).

The agreement between the analytical prediction and experimental data suggests that the hypothesis that the nonflat equilibrium position of the resonator is caused by buckling can be a valid one. Along with the work reported in reference [5], the present study provides the first evidence of such a phenomenon in microscale resonators. In addition, the present work can be used as a basis to study buckling and free oscillations of resonators with stepwise axially varying properties.

#### APPENDIX

Here, the details of the constants that arise in the context of (40) are provided. See the equation at the top of the next page.

$$\begin{aligned}
B_{1,k} &= \frac{EA_k l^2 b^2 P_{c,k}}{EI_k (x_k - x_{k-1})} \\
&\times \left\{ a_{2,k} \sin(\lambda_{1,k} x) + a_{3,k} \zeta_k \lambda_{1,k} \left[ \frac{\cos[(\zeta_k - \lambda_{1,k})x]}{2(\zeta_k - \lambda_{1,k})} + \frac{\cos[(\zeta_k + \lambda_{1,k})x]}{2(\zeta_k + \lambda_{1,k})} \right] \right. \\
&\quad \left. + a_{4,k} \zeta_k \lambda_{1,k} \left[ \frac{\sin[(\zeta_k - \lambda_{1,k})x]}{2(\zeta_k - \lambda_{1,k})} + \frac{\sin[(\zeta_k + \lambda_{1,k})x]}{2\zeta_k + \lambda_{1,k}} \right] \right\} \Bigg|_{x_{k-1}}^{x_k} \\
B_{2,k} &= \frac{EA_k l^2 b^2 P_{c,k}}{EI_k (x_k - x_{k-1})} \\
&\times \left\{ a_{2,k} \cos(\lambda_{1,k} x) + a_{3,k} \zeta_k \lambda_{1,k} \left[ \frac{\sin[(\zeta_k - \lambda_{1,k})x]}{2(\zeta_k - \lambda_{1,k})} - \frac{\sin[(\zeta_k + \lambda_{1,k})x]}{2(\zeta_k + \lambda_{1,k})} \right] \right. \\
&\quad \left. + a_{4,k} \zeta_k \lambda_{1,k} \left[ \frac{-\cos[(\zeta_k - \lambda_{1,k})x]}{2(\zeta_k - \lambda_{1,k})} + \frac{\cos[(\zeta_k + \lambda_{1,k})x]}{2(\zeta_k + \lambda_{1,k})} \right] \right\} \Bigg|_{x_{k-1}}^{x_k} \\
B_{3,k} &= \frac{EA_k l^2 b^2 P_{c,k}}{EI_k (x_k - x_{k-1})} \\
&\times \left\{ a_{2,k} \sinh(\lambda_{2,k} x) - \frac{a_{3,k} \zeta_k \lambda_{2,k}}{\lambda_{2,k}^2 + \zeta_k^2} \left[ \lambda_{2,k} \sin(\zeta_k x) \sinh(\lambda_{2,k} x) - \zeta_k \cos(\zeta_k x) \cosh(\lambda_{2,k} x) \right] \right. \\
&\quad \left. + \frac{a_{4,k} \zeta_k \lambda_{2,k}}{\lambda_{2,k}^2 + \zeta_k^2} \left[ \lambda_{2,k} \cos(\zeta_k x) \sinh(\lambda_{2,k} x) + \zeta_k \sin(\zeta_k x) \cosh(\lambda_{2,k} x) \right] \right\} \Bigg|_{x_{k-1}}^{x_k} \\
B_{4,k} &= \frac{EA_k l^2 b^2 P_{c,k}}{EI_k (x_k - x_{k-1})} \\
&\times \left\{ a_{2,k} \cosh(\lambda_{2,k} x) - \frac{a_{3,k} \zeta_k \lambda_{2,k}}{\lambda_{2,k}^2 + \zeta_k^2} \left[ \lambda_{2,k} \sin(\zeta_k x) \cosh(\lambda_{2,k} x) - \zeta_k \cos(\zeta_k x) \sinh(\lambda_{2,k} x) \right] \right. \\
&\quad \left. + \frac{a_{4,k} \zeta_k \lambda_{2,k}}{\lambda_{2,k}^2 + \zeta_k^2} \left[ \lambda_{2,k} \cos(\zeta_k x) \cosh(\lambda_{2,k} x) + \zeta_k \sin(\zeta_k x) \sinh(\lambda_{2,k} x) \right] \right\} \Bigg|_{x_{k-1}}^{x_k} \\
B_{5,k} &= -\omega_k^2 + \frac{EA_k l^2 b^2 P_{c,k}}{EI_k (x_k - x_{k-1})} \\
&\times \left\{ \frac{a_{3,k}^2 + a_{4,k}^2}{2} \zeta_k^2 x + a_{2,k} a_{3,k} \cos(\zeta_k x) + a_{2,k} a_{4,k} \sin(\zeta_k x) \right. \\
&\quad \left. - \frac{a_{3,k}^2 - a_{4,k}^2}{4} \zeta_k \sin(2\zeta_k x) + \frac{a_{3,k} a_{4,k}}{2} \zeta_k \cos(2\zeta_k x) \right\} \Bigg|_{x_{k-1}}^{x_k}
\end{aligned}$$

#### ACKNOWLEDGMENT

The authors would like to thank Dr. D. DeVoe and Dr. S. Preidikman for valuable discussions related to this work.

#### REFERENCES

- [1] L. Lin, C. T.-C. Nguyen, R. T. Howe, and A. P. Pisano, "Microelectromechanical filters for signal processing," in *Proc. Micro Electro Mechanical Systems, 1992, MEMS '92: An Investigation of Micro Structures, Sensors, Actuators, Machines and Robot*, Feb. 4–7, 1992, pp. 226–231.
- [2] M. I. Younis and A. H. Nayfeh, "A study of the nonlinear response of a resonant microbeam to an electric actuation," *Nonlinear Dynam.*, vol. 31, no. 1, pp. 91–117, 2003.
- [3] D. L. DeVoe, "Piezoelectric thin film micromechanical beam resonators," *Sens. Actuators A, Phys.*, vol. 88, pp. 263–272, 2001.
- [4] L. Currano, "Experimental and Finite Element Analysis of Piezoelectrically Driven MEMS Actuators," M.S. Thesis, Department of Mechanical Engineering, University of Maryland, College Park, MD, 2002.
- [5] H. Li and B. Balachandran, "Buckling induced nonlinear phenomenon in a micro-electromechanical resonator," in *Proc. ASME International Mechanical Engineering Congress and Exposition*, 2002, Paper no. IMECE2002-39 010.
- [6] M. Chiao and L. Lin, "Self-Buckling of micromachined beams under resistive heating," *J. Microelectromech. Syst.*, vol. 9, no. 1, pp. 146–151, 2000.
- [7] U. Lindberg, J. Soderkvist, T. Lammerink, and M. Elwenspoek, "Quasi-buckling of micromachined beams," *J. Micromech. Microeng.*, vol. 3, pp. 183–186, 1998.
- [8] W. Fang and J. A. Wickert, "Post-Buckling of micromachined beams, micro electro mechanical systems," *J. Micromech. Microeng.*, vol. 4, pp. 116–122, 1994.
- [9] M. T. A. Saif, "On a tunable bistable MEMS—Theory and experiment," *J. Microelectromech. Syst.*, vol. 9, pp. 157–170, Jun. 2000.
- [10] A. H. Nayfeh, W. Kreider, and T. J. Anderson, "Investigation of natural frequencies and mode shapes of buckled beams," *AIAA Journal*, vol. 33, no. 6, pp. 1121–1126, Jun. 1995.
- [11] A. H. Nayfeh and W. Lacarbonara, "On the discretization of spatially continuous systems with quadratic and cubic nonlinearities," *JSME Int. J.*, vol. 41, no. 3, pp. 510–531, 1998.

- [12] A. H. Nayfeh and D. T. Mook, *Nonlinear Oscillations*. New York: Wiley, 1979, pp. 447–453.
- [13] Y. R. Talpaert, *Tensor Analysis and Continuum Mechanics*. New York: Kluwer Academic, 2002, pp. 199–209.
- [14] R. Seshadri, "Active Vibration Control of Beams Using Piezoelectric Actuators," M.S. Scholarly Paper, Department of Mechanical Engineering, University of Maryland, College Park, MD, 1994.

**He Li** received the B.S. degree in material science from Harbin Institute of Technology, China, and the M.S. degree in mechanical engineering from University of Science and Technology of Beijing, P. R. China, in 1995 and 2000, respectively. He is currently working towards the Ph.D. degree in the Department of Mechanical Engineering of University of Maryland, College Park.

His research interests include nonlinear dynamics, computational design and modeling of Microelectromechanical Systems (MEMS) and smart structures, fiber optics.

**B. Balachandran** is a Professor of Mechanical Engineering at the University of Maryland. His research interests include nonlinear dynamics, vibration and acoustics control, system identification, and signal analyses. The publications that he has authored/coauthored include a Wiley textbook entitled *Applied Nonlinear Dynamics: Analytical, Computational, and Experimental Methods* (New York: 1995) and a Thomson textbook entitled *Vibrations* (New York: 2003).

Dr. Balachandran is a Fellow of the American Society of Mechanical Engineers (ASME). He serves on the Editorial Board of the *Journal of Vibration and Control* and as an Associate Editor of the *AIAA Journal* and the *ASME Journal of Computational and Nonlinear Dynamics*.

# Nonlinear free and forced oscillations of piezoelectric microresonators

H Li, S Preidikman, B Balachandran and C D Mote Jr

Department of Mechanical Engineering, University of Maryland, College Park, MD 20742-3035, USA

Received 21 September 2005, in final form 2 December 2005

Published 13 January 2006

Online at stacks.iop.org/JMM/16/356

## Abstract

Free and forced oscillations of piezoelectric, microelectromechanical resonators fabricated as clamped–clamped composite structures are studied in this effort. Piezoelectric actuation is used to excite these structures on the input side and piezoelectric sensing is carried out on the output side. A refined integro-partial differential model is developed for a clamped–clamped composite beam structure and used for studying the nonlinear transverse vibrations of these resonators. This model accounts for the longitudinal extension due to transverse vibrations, distributed actuation and axially varying properties across the length of the structure. Free oscillations about a post-buckled position are studied, and for weak damping and weak forcing, the method of multiple scales is used to obtain an approximate solution for the response to a harmonic forcing. Analytical predictions are also compared with experimental observations. The model development and the analysis can serve as a basis for analysing the responses of other composite microresonators.

(Some figures in this article are in colour only in the electronic version)

## 1. Introduction

Nonlinear oscillations of microelectromechanical resonators fabricated as clamped–clamped composite structures are studied in this paper. These microresonators, which are to be used as filters, are important for mobile communication systems and signal processing applications (e.g., Fourier transform computations) [1]. While the nonlinear response of a microresonator subjected to an electrostatic actuation has received considerable attention [2], the nonlinear response of a microresonator subjected to a piezoelectric actuation has received limited attention recently [3].

The resonators considered in this effort are based on the piezoelectric effect, as shown in figure 1. Fabrication details for these resonators can be found in [4]. The dimensions of the resonators considered in this study typically range in length from 50  $\mu\text{m}$  to 400  $\mu\text{m}$ , with a width of 20  $\mu\text{m}$ , and a thickness of about 2.3  $\mu\text{m}$ . The elastic substrate is an amorphous  $\text{SiO}_2$  layer, on the top of which a thin platinum electrode layer is deposited first, followed by a layer of sol–gel piezoelectric film throughout the structure's length. To complete the structure, a platinum electrode layer that extends over one quarter of the length from each boundary is deposited as the top layer [5],

so that each resonator structure has three layers in the mid-span where the top electrode layer is absent and four layers elsewhere. Due to the asymmetry of the cross section, the position of the piezoelectric layer is offset from the neutral axis, and in addition, residual stress may also be introduced in each layer during the fabrication process.

For comparisons of model predictions with experimental results, particular attention is paid to a 200  $\mu\text{m}$  long resonator. The material properties and thickness values for the different layers are provided in tables 1 and 2. As discussed later in the third section, each resonator is modeled as a composite beam with properties that vary in a stepwise manner from section to section, as shown in figure 2. The values of axial stiffness, bending stiffness and mass per unit length for the different sections are given in table 3 and these values are identified by using the subscripts used in figure 2.

The experimental observations that will be used for comparison with the analytical predictions are collected together in the next section. In the third section, the model development carried out to study buckling in a composite structure is presented, and in the fourth section, analysis of linear free oscillations of the structure is detailed. Forced oscillations are examined in the fifth section

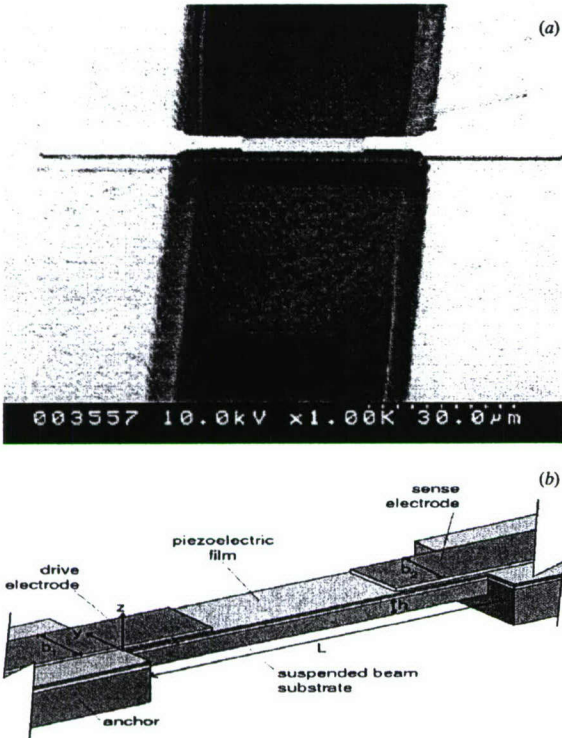


Figure 1. Piezoelectric microresonator: (a) SEM of a 50 μm long PZT microresonator [6] and (b) a schematic showing the details [5].

Table 1. Material properties for different layers of a 200 μm composite resonator.

	SiO <sub>2</sub>	Bottom Pt	PZT	Top Pt
$\rho$ (kg m <sup>-3</sup> )	2194	17 839	8800	18 762
$E$ (Pa)	$100 \times 10^9$	$160 \times 10^9$	$25 \times 10^9$	$160 \times 10^9$

Table 2. Thickness values for a 200 μm composite resonator.

SiO <sub>2</sub> (μm)	Bottom Pt (μm)	PZT (μm)	Top Pt (μm)
1.030	0.085	1.09	0.090

and the results and discussion are presented in the sixth section.

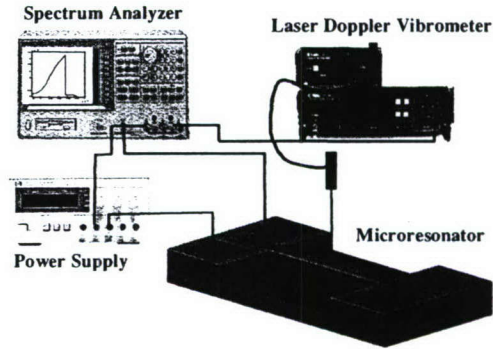


Figure 3. Experimental arrangement of laser vibrometer for examining transverse vibrations at the mid-span of the resonator. This structure is excited by signals input to the drive electrode.

Table 3. Values of axial stiffness, bending stiffness and mass per unit length for the 200 μm long resonator of interest.

$EA_1$ (N)	$EA_2$ (N)	$EA_3$ (N)
3.17	2.88	3.17
$EI_1$ (N m <sup>2</sup> )	$EI_2$ (N m <sup>2</sup> )	$EI_3$ (N m <sup>2</sup> )
$1.39 \times 10^{-12}$	$0.83 \times 10^{-12}$	$1.39 \times 10^{-12}$
$m_1$ (kg m <sup>-1</sup> )	$m_2$ (kg m <sup>-1</sup> )	$m_3$ (kg m <sup>-1</sup> )
$3.01 \times 10^{-1}$	$2.68 \times 10^{-1}$	$3.01 \times 10^{-1}$

## 2. Experiments and observations

In figure 3, a sketch of the experimental arrangement used to study transverse vibrations of a microresonator is shown. The silicon wafer containing the resonator is first placed on a probe station, and the drive port of the resonator is electrically connected to provide a sinusoidal excitation along with a dc bias input. A laser vibrometer is used to measure the transverse vibrations at the mid point of the resonator, and the data are collected by using a dynamic spectrum analyser.

For a 200 μm long resonator, the first natural frequency was experimentally determined to be close to 313 kHz, while the model prediction for this resonator, without consideration of the axial force and possible nonflatness of static state, is about 186 kHz. In figure 4(a), a representative spatial response distribution of another resonator obtained by using a scanning laser vibrometer is shown. The resonator is excited by a

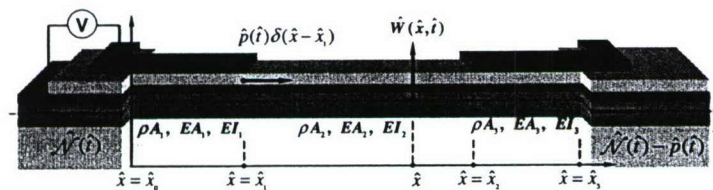
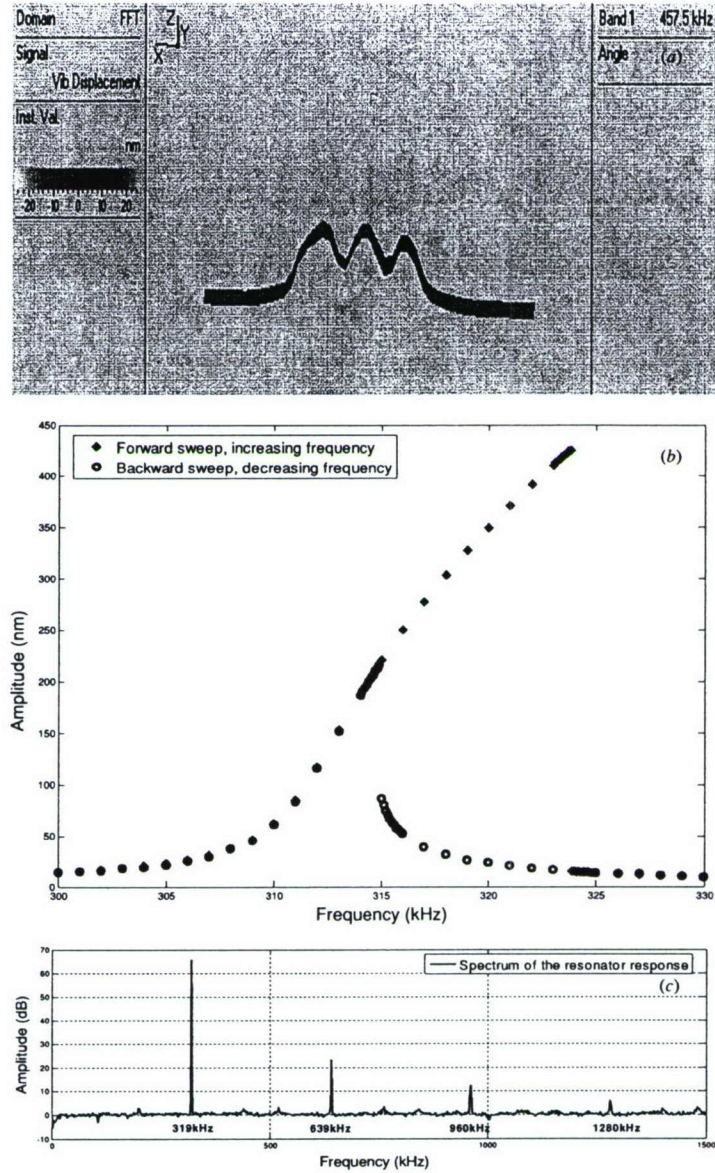


Figure 2. Clamped-clamped composite structure model of piezoelectrically actuated resonator shown in figure 1.



**Figure 4.** Microresonator response: (a) laser vibrometer measurement of a spatial pattern observed in experiments; (b) hardening Duffing-type frequency response of a  $200\ \mu\text{m}$  PZT resonator excited by a sinusoidal input signal with an amplitude of  $0.398\ \text{V}$  and (c) spectrum of the laser vibrometer measurement at the mid-span of a  $200\ \mu\text{m}$  resonator, in response to an excitation with a frequency close to the first natural frequency and an amplitude of  $60\ \text{mV}$ .

sinusoidal excitation with a frequency close to the first natural frequency [6]. The presence of spatial harmonics distorts the spatial pattern from the typical mode shape associated with the fundamental mode of vibration of a clamped–clamped beam. A typical frequency response observed in the experiments is shown in figure 4(b). The response amplitude varies from a few hundred nanometers to a micrometer depending on the excitation level. In figure 4(c), it is illustrated that the response spectrum consists of second and third harmonics.

The presence of second harmonics suggests that the oscillations may be taking place about a nonflat static equilibrium position (e.g., [7]).

In this paper, the hypothesis that the nonflat static equilibrium position is caused by buckling is pursued along the lines of our recent work ([3]). This hypothesis is motivated by prior work conducted with buckled microstructures [8–14] and large-scale structures [15]. The prior studies on microstructures have by and large focused on the static cases of electrostatically actuated microstructures [11–14], and in addition, these structures were modeled as uniform beams. By contrast, in this work, the microstructures are piezoelectrically actuated and these structures have properties that vary stepwise in the axial direction. Here, a refined model of a composite structure with axially varying

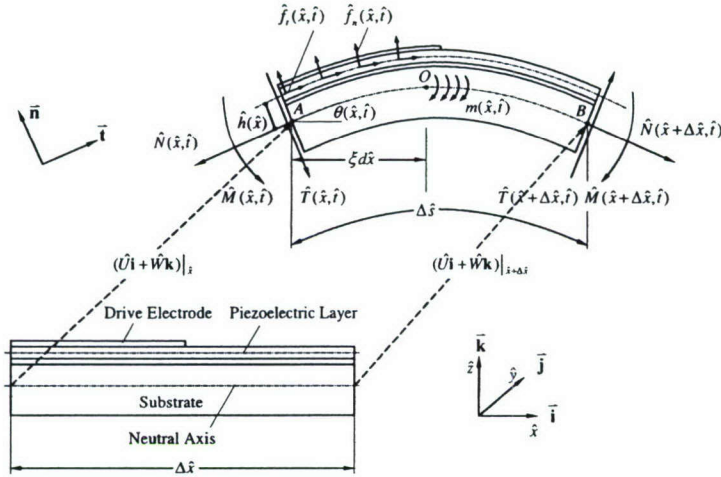


**Figure 5.** Free-body diagram of an infinitesimal beam section. The beam is deformed from an initial flat position.  $\Delta\hat{x}$  is the length of the undeformed beam segment and  $\Delta\hat{x}$  is the length of the corresponding deformed segment.

properties is developed and used to predict the spatial responses and temporal responses of microresonators and also accurately predict the first natural frequency of the considered microresonator.

### 3. Model development and buckling analysis

Following that, this model is extended to apply to a structure with stepwise variation of the properties along the length of the structure, such as that shown in figure 2.

This model is used to examine static buckling in composite structures such as the microresonators considered in this paper, and after establishing the static-equilibrium position as a buckled position, free oscillations are considered about a buckled position in the fourth section. This work is of a general nature and it can be used to study buckling in any composite beam with axial properties that vary in a stepwise fashion across the structure's length. The treatment presented in this paper is a refinement of an earlier treatment presented by the authors [17]. Compared to the authors' earlier work, the treatment of kinematics is different in this case.

#### 3.1. Governing equations

To establish the governing equations, apart from the Euler–Bernoulli beam assumptions, it is also assumed that the axial and transverse displacements are small compared to the length and that the initial flat position shown in figure 5 is free of stresses and external forces. The governing equations along axial and transverse directions can be obtained as [19]

$$\rho A \frac{\partial^2 \hat{U}}{\partial \hat{t}^2} + 2\hat{\mu}_u \frac{\partial \hat{U}}{\partial \hat{t}} - \frac{\partial}{\partial \hat{x}} \left\{ EA \left[ \frac{\partial \hat{U}}{\partial \hat{x}} + \frac{1}{2} \left( \frac{\partial \hat{W}}{\partial \hat{x}} \right)^2 - \frac{\partial \hat{U}}{\partial \hat{x}} \left( \frac{\partial \hat{W}}{\partial \hat{x}} \right)^2 \right] + \frac{\partial}{\partial \hat{x}} \left( EI \frac{\partial^2 \hat{W}}{\partial \hat{x}^2} \right) \frac{\partial \hat{W}}{\partial \hat{x}} \left( 1 - \frac{\partial \hat{U}}{\partial \hat{x}} \right) \right\}$$

$$\begin{aligned} &= \hat{f}_t \left( 1 + \frac{\partial \hat{U}}{\partial \hat{x}} \right) - \hat{f}_n \frac{\partial \hat{W}}{\partial \hat{x}} - \frac{\partial}{\partial \hat{x}} \left( \hat{m} \frac{\partial \hat{W}}{\partial \hat{x}} \right) \quad (1) \\ &\rho A \frac{\partial^2 \hat{W}}{\partial \hat{t}^2} + 2\hat{\mu}_w \frac{\partial \hat{W}}{\partial \hat{t}} - \frac{\partial}{\partial \hat{x}} \left\{ EA \left[ \frac{\partial \hat{U}}{\partial \hat{x}} - \left( \frac{\partial \hat{U}}{\partial \hat{x}} \right)^2 + \frac{1}{2} \left( \frac{\partial \hat{W}}{\partial \hat{x}} \right)^2 \right] \frac{\partial \hat{W}}{\partial \hat{x}} \right\} + \frac{\partial^2}{\partial \hat{x}^2} \left( EI \frac{\partial^2 \hat{W}}{\partial \hat{x}^2} \right) \\ &= \frac{\partial}{\partial \hat{x}} \left\{ \frac{1}{2} \frac{\partial}{\partial \hat{x}} \left( EI \frac{\partial^2 \hat{W}}{\partial \hat{x}^2} \right) \left( \frac{\partial \hat{W}}{\partial \hat{x}} \right)^2 \right. \\ &\quad \times \left. \left[ + \frac{3}{2} \frac{\partial}{\partial \hat{x}} EI \frac{\partial^2 \hat{W}}{\partial \hat{x}^2} \left( \frac{\partial \hat{W}}{\partial \hat{x}} \right)^2 \right] + \hat{m} \left( 1 + \frac{\partial \hat{U}}{\partial \hat{x}} \right) \right\} \\ &\quad + \hat{f}_t \frac{\partial \hat{W}}{\partial \hat{x}} + \hat{f}_n \left( 1 + \frac{\partial \hat{U}}{\partial \hat{x}} \right), \quad (2) \end{aligned}$$

where the carat symbol '^' has been used to indicate a dimensional variable;  $\hat{U}(\hat{x}, \hat{t})$  and  $\hat{W}(\hat{x}, \hat{t})$  are the axial and transverse displacements;  $\hat{x}$  is the spatial variable and  $\hat{t}$  is the time;  $\rho A$  is the mass density per unit length;  $EA$  is the axial stiffness;  $EI$  is the bending stiffness;  $\hat{\mu}_u$  and  $\hat{\mu}_w$  are the viscous damping factors for motions along the axial and transverse directions, respectively. As shown in figure 5,  $\hat{f}_t(\hat{x}, \hat{t})$  and  $\hat{f}_n(\hat{x}, \hat{t})$  are distributed forces along the tangent and normal directions, and  $\hat{m}(\hat{x}, \hat{t})$  is a distributed moment; the axial force  $\hat{N}(\hat{x}, \hat{t})$  is given by

$$\hat{N}(\hat{x}, \hat{t}) = EAe, \quad (3)$$

where  $e$  is the Green–Lagrange strain measure [20], corresponding to the elongation of the beam along the longitudinal direction. The expression for  $e$  will be given later in this paper.

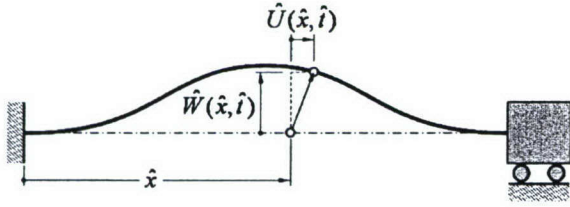


**Figure 6.** Structure with clamped–clamped boundary conditions governing the transverse vibrations and clamped–sliding boundary conditions governing the axial vibrations.

For later use, the following dimensionless quantities are introduced:

$$\begin{aligned} x &= \frac{\hat{x}}{l}, & h &= \frac{\hat{h}}{l}, & W &= \frac{\hat{W}}{l}, \\ U &= \frac{\hat{U}}{l}, & t &= \frac{\hat{t}}{l^2} \sqrt{\frac{EI}{\rho A}}, & f_i &= \frac{\hat{f}_i l^3}{EI}, \\ f_n &= \frac{\hat{f}_n l^3}{EI}, & m &= \frac{\hat{m} l^2}{EI}, & \bar{\mu} &= \frac{\hat{\mu}_w l^2}{\sqrt{\rho A EI}}. \end{aligned} \quad (4)$$

For the microresonator parameter values given in table 3, the slenderness ratio  $r = \sqrt{EI/EA}l^{-1}$  is of the order of  $10^{-3}$ . Based on this observation, an additional assumption that  $U = O(W^2)$  has been used, where  $O(\cdot)$  is the Landau symbol that is used here to state that  $U$  is of the order of  $W^2$  [18]. It is also assumed that  $W = O(r)$  and  $e = O(r^2)$ .

Introducing the dimensionless quantities given by equation (4) into equations (1) and (2), dropping the higher-order terms, and simplifying, the governing equation of a uniform beam with constant  $\rho A$ ,  $EI$  and  $EA$  values can be obtained as shown below.

$$\frac{\partial}{\partial x} \left( \frac{e}{r^2} \right) + f_i = 0 \quad (5)$$

$$\frac{\partial^2 W}{\partial t^2} + 2\bar{\mu} \frac{\partial W}{\partial t} - \frac{e}{r^2} \frac{\partial^2 W}{\partial x^2} + \frac{\partial^4 W}{\partial x^4} = \frac{\partial m}{\partial x} + f_n. \quad (6)$$

Here, noting that the resonator is actuated by a distributed piezoelectric layer, as shown in figures 2 and 5, the boundary conditions for axial and transverse vibrations are considered as shown in figure 6.

$$W(x, t) = 0, \quad \frac{\partial W(x, t)}{\partial x} = 0, \quad U(x, t) = 0 \quad \text{at } x = 0,$$

$$W(x, t) = 0, \quad \frac{\partial W(x, t)}{\partial x} = 0, \quad U(x, t) = \bar{\varepsilon} \quad \text{at } x = 1. \quad (7)$$

Equations (5) and (6) along with the boundary conditions (7) represent the governing equations of a clamped–clamped structure. From the form of equation (5), it is clear that the longitudinal dynamics is neglected but the dependence of the longitudinal strain on the transverse excitation and displacement are captured.

### 3.2. Governing equations for microresonators with stepwise varying properties

For the microresonators shown in figure 2, as discussed in the previous work of the authors [17], the axial properties can be

written as

$$\rho A(\hat{x}) = \sum_{k=1}^n \rho A_k H_k(\hat{x}), \quad EA(\hat{x}) = \sum_{k=1}^n EA_k H_k(\hat{x}), \quad (8)$$

$$EI(\hat{x}) = \sum_{k=1}^n EI_k H_k(\hat{x}), \quad \hat{h}(\hat{x}) = \sum_{k=1}^n h_k H_k(\hat{x}),$$

where the subscript  $k$  represents the  $k$ th section of the resonator and this index runs from 1 to 3. The quantities  $\rho A_k$ ,  $EI_k$ ,  $EA_k$  and  $\hat{h}_k$  are constant over the section of interest. Furthermore, in equation (8), the function  $H_k(\hat{x}) = [u(\hat{x} - \hat{x}_{k-1}) - u(\hat{x} - \hat{x}_k)]$  is constructed by using the unit step function  $u(\hat{x})$ .

Following the earlier work on structures with piezoelectric elements (e.g., [21]), noting that the distributed actuation is present in the first section of the microresonator, the distributed loading is determined as (figure 2)

$$\begin{aligned} \hat{f}_i(\hat{x}, \hat{t}) &= \hat{p}(\hat{t})\delta(\hat{x} - \hat{x}_1), & \hat{p}(\hat{t}) &= \hat{p}_0 \cos \hat{\Omega} \hat{t}, \\ \hat{m}(\hat{x}, \hat{t}) &= \hat{f}_i(\hat{x}, \hat{t})\hat{h}(\hat{x}), & \hat{f}_n(\hat{x}, \hat{t}) &= 0, \end{aligned} \quad (9)$$

where  $\hat{p}_0$  is the input forcing amplitude,  $\hat{\Omega}$  is the input excitation frequency and  $\delta(\hat{x})$  is the Dirac delta function. For convenience of discussion, the following quantities are introduced:

$$X_k = U_k(x_k), \quad K_k = \frac{EA_k}{(x_k - x_{k-1})},$$

$$\bar{EA} = \left[ \sum_{i=1}^n K_i^{-1} \right]^{-1}, \quad \hat{N}_0 = \bar{EA} \bar{\varepsilon} \quad (10)$$

$$\bar{EA}_1 = \left[ \sum_{i=1}^n K_i^{-1} \right]^{-1}, \quad \bar{EA}_2 = \left[ \sum_{i=m+1}^n K_i^{-1} \right]^{-1},$$

where  $\bar{(\cdot)}$  means an average value.

After using the boundary conditions given in (7), the displacement compatibility conditions

$$U_k(x_k) = U_{k+1}(x_k), \quad W_k(x_k) = W_{k+1}(x_k) \quad (11)$$

and making use of equation (9) in (6), the result obtained is the following equation governing the transverse vibration field in the  $k$ th section [19]:

$$\begin{aligned} \frac{\partial^2 W_k}{\partial t_k^2} + 2\bar{\mu}_k \frac{\partial W_k}{\partial t_k} - \frac{e_k}{r_k^2} \frac{\partial^2 W_k}{\partial x^2} + \frac{\partial^4 W_k}{\partial x^4} &= \bar{F}_k \cos \Omega_k t_k \\ x &\in [x_{k-1}, x_k], \quad k = 1, 2, 3. \end{aligned} \quad (12)$$

In equation (12),

$$\begin{aligned} e_k(t_k) &= r_k^2 N_k + r_k^2 q_k \bar{p}_k \cos(\Omega_k t_k) + \left[ \sum_{i=1}^n \Lambda_{ik} \int_{x_{i-1}}^{x_i} \left( \frac{\partial W_i}{\partial x} \right)^2 dx \right] \\ x &\in [x_{k-1}, x_k], \quad k = 1, 2, \dots, n, \end{aligned} \quad (13)$$

where

$$\Lambda_{ik} = \begin{cases} \frac{\bar{EA}}{2EA_k}, & i \neq k \\ \frac{\bar{EA}}{2EA_k} + \frac{1}{(x_k - x_{k-1})}, & i = k, \end{cases} \quad (14)$$

$$q_k = \begin{cases} \frac{\bar{EA}}{EA_2}, & k \leq m \\ -\frac{\bar{EA}}{EA_1}, & k > m \end{cases} \quad (15)$$

$$N_k = \frac{\hat{N}_0 l^2}{EI_k}, \quad \bar{F}_k(x) = \bar{p}_k h_k \frac{\partial \delta(x - x_1)}{\partial x}, \quad (16)$$

$$\bar{p}_k = \frac{\hat{p}_0 l^2}{EI_k}, \quad \text{and} \quad \Omega_k = \sqrt{\frac{\rho A_k l^4}{EI_k}} \hat{\Omega}.$$

Equations (12)–(16) are suitable for studies of structures with axially varying properties and distributed actuation. In addition, this model is applicable to structures with ‘small’ slenderness ratios such as the microresonators considered in this work.

In sections 3.3, 4 and 5, solutions of equation (12) are sought. First, the possibility for static buckling is explored and this corresponds to the situation when the resonator structure is released from the Si wafer. Following that, free and forced oscillation problems around the post-buckling state are then solved. The developments of sections 4 and 5 are applicable to any resonator with a non-flat equilibrium position.

### 3.3. Static buckling problem

In this section, the static buckling problem is addressed along the lines of the authors’ previous work [17]. It is assumed that the dimensionless static buckling deflection of the resonator can be expressed as

$$\chi(x) = \sum_{k=1}^n \chi_k(x) H_k(x), \quad (17)$$

where  $\chi_k(x)$  is the transverse displacement of the  $k$ th section of the beam. For the static buckling analysis, the inertia, damping and external actuation terms in equation (12) are dropped, and the static axial forces (extensional)  $\hat{N}_0$  and  $N_k$  given in equations (10) and (16) are replaced by the static compressive forces  $-\hat{P}_0$  and  $-P_{0,k}$ , respectively. After carrying these substitutions through, the nonlinear equation governing the equilibrium of the beam subjected to a static axial force can be written as

$$\frac{d^4 \chi_k}{dx^4} + \left\{ P_{0,k} - \frac{1}{r_k^2} \sum_{i=1}^3 \left[ \Lambda_{ik} \int_{x_{i-1}}^{x_i} \left( \frac{d\chi_i}{dx} \right)^2 dx \right] \right\} \frac{d^2 \chi_k}{dx^2} = 0, \quad (18)$$

$$k = 1, 2, \dots, n.$$

The associated boundary conditions follow the form of (7).

The approximate solution of the post-buckling system described by equation (18) can be obtained as given below, in terms of a critical buckling mode shape with the amplitude  $b$ , called the *buckling factor*.

$$\chi_k(x) = b \psi_k(x). \quad (19)$$

This is given by

$$b^2 = \frac{(\hat{P}_0 - \hat{P}_c)}{EA_k \sum_{i=1}^n \left[ \Lambda_{ik} \int_{x_{i-1}}^{x_i} (d\psi_i/dx)^2 dx \right]}, \quad (20)$$

where  $\psi_k(x)$  is the  $k$ th component of the static critical buckling mode shape  $\psi(x)$  and it has the form

$$\psi_k(x) = a_{1,k} + a_{2,k}x + a_{3,k} \cos(\zeta_k x) + a_{4,k} \sin(\zeta_k x). \quad (21)$$

In equation (21),  $\zeta_k^2 = P_{c,k} = \hat{P}_c l^2 / EI_k$  and the constants  $a_{i,k}$  for  $i = 1, 2, 3, 4$  and  $k = 1, 2, \dots, n$  can be determined

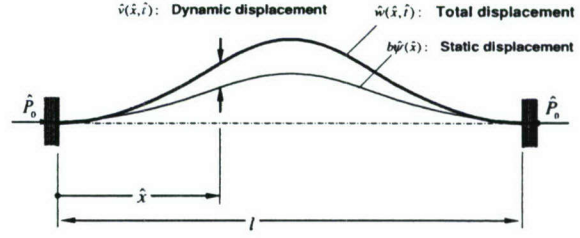


Figure 7. Buckled beam configuration.

by making use of the following boundary conditions and compatibility conditions:

$$\psi_1(x) = 0, \quad \frac{d\psi_1(x)}{dx} = 0 \quad \text{at} \quad x = x_0, \quad (22)$$

$$\psi_n(x) = 0, \quad \frac{d\psi_n(x)}{dx} = 0 \quad \text{at} \quad x = x_n.$$

$$\psi_{k-1}(x) = \psi_k(x), \quad \frac{d\psi_{k-1}(x)}{dx} = \frac{d\psi_k(x)}{dx}$$

$$EI_{k-1} \frac{d^2 \psi_{k-1}(x)}{dx^2} = EI_k \frac{d^2 \psi_k(x)}{dx^2} \quad (23)$$

$$EI_{k-1} \frac{d^3 \psi_{k-1}(x)}{dx^3} = EI_k \frac{d^3 \psi_k(x)}{dx^3} \quad \text{at} \quad x = x_{k-1}$$

Here, it is important to note that in making the approximation (19), the boundary condition for axial motions is held fixed at  $x = l$  instead of the sliding boundary condition shown in figure 6, previously.

## 4. Free linear oscillations about the post-buckled position

Free oscillations of the undamped resonator are considered in this section. The governing equation of motion in the presence of a compressive axial load is of the form

$$\frac{\partial^2 w_k}{\partial t_k^2} + \left\{ P_{0,k} - \frac{1}{r_k^2} \left[ \sum_{i=1}^n \Lambda_{ik} \int_{x_{i-1}}^{x_i} \left( \frac{\partial w_i}{\partial x} \right)^2 dx \right] \right\} \frac{\partial^2 w_k}{\partial x^2} + \frac{\partial^4 w_k}{\partial x^4} = 0, \quad k = 1, 2, \dots, n. \quad (24)$$

where  $w_k$  is the overall transverse displacement in the free-vibration case. The corresponding boundary and compatibility conditions are similar to those given by equations (22) and (23). Following the authors’ previous work ([17, 18]), the solution of this boundary-value problem can be written as the sum of a static component and a dynamic component (see figure 7).

$$w_k(x, t_k) = b \psi_k(x) + v_k(x, t_k), \quad (25)$$

where  $v_k(x, t_k)$  is the  $k$ th component of the dynamic deflection.

Next, the natural frequencies  $\hat{\omega}$  and mode shapes associated with free oscillations around the post-buckled position  $b\psi(x)$  are examined. To find the natural frequencies and mode shapes, one first substitutes equation (25) into equation (24), assumes that  $|v_k(x, t_k)| \ll |b\psi_k(x)|$ , and uses separation of variables in the following form:

$$v_k(x, t_k) = \phi_k(x) e^{j\omega_k t_k}, \quad (26)$$

where  $j^2 = -1$ , and  $\phi_k(x)$  and  $\omega_k = \sqrt{\rho A_k / EI_k} l^2 \hat{\omega}$  are the mode shape and the natural frequency associated with

section  $k$ , respectively. Here, it is necessary to emphasize the relationship between  $\omega_k$  and  $\hat{\omega}$ ; that is,  $\omega_k t_k = \hat{\omega} t$ . Making use of equations (20), (24), (25) and (26), the following is obtained:

$$-\omega_k^2 \phi_k + P_{c,k} \frac{d^2 \phi_k}{dx^2} + \frac{d^4 \phi_k}{dx^4} - \frac{2b^2}{r_k^2} \frac{d^2 \psi_k}{dx^2} \times \left[ \sum_{i=1}^n \Lambda_{ik} \int_{x_{i-1}}^{x_i} \left( \frac{d\psi_i}{dx} \frac{d\phi_i}{dx} \right) dx \right] = 0. \quad (27)$$

The general solution of (27) is given by

$$\phi_k(x) = C_{1,k} \sin(\lambda_{1,k}x) + C_{2,k} \cos(\lambda_{1,k}x) + C_{3,k} \sinh(\lambda_{2,k}x) + C_{4,k} \cosh(\lambda_{2,k}x) + C_{5,k} [a_{3,k} \cos(\zeta_k x) + a_{4,k} \sin(\zeta_k x)], \quad (28)$$

where

$$\lambda_{1,k} = \sqrt{\frac{1}{2}(P_{c,k} + \sqrt{P_{c,k}^2 + 4\omega_k^2})}, \quad (29)$$

$$\lambda_{2,k} = \sqrt{\frac{1}{2}(-P_{c,k} + \sqrt{P_{c,k}^2 + 4\omega_k^2})}$$

and the  $C_{r,k}$ ,  $r = 1, 2, \dots, 5$ , are constants that satisfy

$$\sum_{i=1}^n \Lambda_{ik} (B_{1,i} C_{1,i} + B_{2,i} C_{2,i} + B_{3,i} C_{3,i} + B_{4,i} C_{4,i} + D_{k,i} C_{5,i}) = 0, \quad (30)$$

where the  $B_{r,i}$  and  $D_{k,i}$  ( $r = 1, 2, 3, 4$  and  $k = 1, 2, \dots, n$ ) are constants, the expressions for which are detailed in [17, 19] along with the derivations for equations (24)–(30).

Equation (30) along with the associated boundary conditions and compatibility conditions forms an eigenvalue problem for the eigenmodes  $C_{r,i}$  and the natural frequencies  $\omega_k$ . After determining these values for  $C_{r,i}$ , the expression for the free vibration mode shapes of the post-buckled beam with axially varying properties can be determined as

$$\phi(x) = \sum_{k=1}^n \phi_k(x) H_k(x). \quad (31)$$

## 5. Forced oscillations

Forced oscillations of a resonator modeled as a beam with axially varying properties are considered in this section. The equation of motion is given by equations (12) and (13), the boundary conditions are given by equations (7), and the displacement compatibility conditions are similar to those given by (23). For solving (12), it is assumed that

$$W_k(x, t_k) = b\psi_k(x) + \eta_k(x, t_k), \quad (32)$$

where  $\eta_k(x, t_k)$  represents the dynamic deflection and  $b\psi_k(x)$  is the static post-buckling deflection given by (19). Making use of the development given in section 3.3 and (32), equation (18) can be rewritten as

$$\begin{aligned} \ddot{\eta}_k + P_{c,k} \eta_k'' + \eta_k^{iv} - \frac{2b^2}{r_k^2} \left[ \sum_{i=1}^n \Lambda_{ik} \langle \psi'_i, \eta'_i \rangle_i \right] \psi_k'' \\ = [\bar{F}_k + q_k \bar{p}_k (b\psi_k'' + \eta_k'')] \cos(\Omega_k t_k) - 2\bar{\mu}_k \dot{\eta}_k \\ + \frac{2b}{r_k^2} \left[ \sum_{i=1}^n \Lambda_{ik} \langle \psi'_i, \eta'_i \rangle_i \right] \eta_k'' + \frac{1}{r_k^2} \left[ \sum_{i=1}^n \Lambda_{ik} \langle \eta'_i, \eta'_i \rangle_i \right] \eta_k'' \\ + \frac{b}{r_k^2} \left[ \sum_{i=1}^n \Lambda_{ik} \langle \eta'_i, \eta'_i \rangle_i \right] \psi_k'', \quad k = 1, 2, \dots, n. \quad (33) \end{aligned}$$

From here onwards, the following notation and definitions are used for convenience:  $(\cdot) = \partial/\partial t_k$ ,  $(\cdot)' = \partial/\partial x$ ,  $\langle a, b \rangle_i = \int_{x_{i-1}}^{x_i} a(x)b(x) dx$  and  $\langle a, b \rangle = \int_{x_0}^{x_n} a(x)b(x) dx$ . Again, the boundary and compatibility conditions are similar to those given by (22) and (23). Next, assuming weak damping and forcing terms, the method of multiple scales [22] is used to seek for an approximate solution of (33). The basic approach follows that presented in an earlier work [16], but here, the application is directed toward a composite microscale structure with varying axial properties. Different time scales are introduced by using a small, dimensionless book-keeping parameter  $\varepsilon$  as follows:

$$T_{0k} = t_k, \quad T_{1k} = \varepsilon t_k, \quad T_{2k} = \varepsilon^2 t_k, \quad \dots \quad (34)$$

The time derivatives take the form

$$\partial/\partial t_k = D_{0k} + \varepsilon D_{1k} + \varepsilon^2 D_{2k} + \dots, \quad D_{ik} = \partial/\partial T_{ik}, \quad (35)$$

where

$$D_{ik} = l^2 \sqrt{\frac{\rho A_k}{E I_k}} \hat{D}_i \quad \text{and} \quad \hat{D}_i = \frac{\partial}{\partial \hat{T}_i}. \quad (36)$$

To balance the effect of the nonlinearity, damping and excitation, the following scaling is used:

$$\bar{p}_k = \varepsilon^3 p_k, \quad \bar{\mu}_k = \varepsilon^2 \mu_k. \quad (37)$$

The approximate solution is then expanded as

$$\eta_k(x, t_k) = \varepsilon \eta_{1k}(x, T_{0k}, T_{1k}, T_{2k}) + \varepsilon^2 \eta_{2k}(x, T_{0k}, T_{1k}, T_{2k}) + \varepsilon^3 \eta_{3k}(x, T_{0k}, T_{1k}, T_{2k}) + \dots \quad (38)$$

Introducing (34)–(38) into (33), rewriting the excitation term in polar form, and collecting terms of the same power of  $\varepsilon$ , the following hierarchy of equations is obtained:

$O(\varepsilon)$ :

$$\begin{aligned} \mathcal{L}(\eta_{1k}) = D_{0k}^2 \eta_{1k} + P_{c,k} \eta_{1k}'' + \eta_{1k}^{iv} \\ - \frac{2b^2}{r_k^2} \left[ \sum_{i=1}^n \Lambda_{ik} \langle \psi'_i, \eta'_{1i} \rangle_i \right] \psi_k'' = 0 \end{aligned} \quad (39)$$

$O(\varepsilon^2)$ :

$$\begin{aligned} \mathcal{L}(\eta_{2k}) = \frac{2b}{r_k^2} \left[ \sum_{i=1}^n \Lambda_{ik} \langle \psi'_i, \eta'_{1i} \rangle_i \right] \eta_{1k}'' \\ + \frac{b}{r_k^2} \left[ \sum_{i=1}^n \Lambda_{ik} \langle \eta'_{1i}, \eta'_{1i} \rangle_i \right] \psi_k'' - 2D_{0k} D_{1k} \eta_{1k} \end{aligned} \quad (40)$$

$O(\varepsilon^3)$ :

$$\begin{aligned} \mathcal{L}(\eta_{3k}) = -2\bar{\mu}_k D_{0k} \eta_{1k} - 2D_{0k} D_{1k} \eta_{2k} - (D_{1k}^2 + 2D_{0k} D_{2k}) \eta_{1k} \\ \times \frac{2b}{r_k^2} \left[ \sum_{i=1}^n \Lambda_{ik} \langle \psi'_i, \eta'_{1i} \rangle_i \right] \eta_{2k}'' + \frac{2b}{r_k^2} \left[ \sum_{i=1}^n \Lambda_{ik} \langle \psi'_i, \eta'_{2i} \rangle_i \right] \eta_{1k}'' \\ + \frac{1}{r_k^2} \left[ \sum_{i=1}^n \Lambda_{ik} \langle \eta'_{1i}, \eta'_{1i} \rangle_i \right] \eta_{1k}'' + \frac{2b}{r_k^2} \left[ \sum_{i=1}^n \Lambda_{ik} \langle \eta'_{1i}, \eta'_{2i} \rangle_i \right] \psi_k'' \\ + \left[ \frac{1}{2} F_k e^{i\Omega_k t_k} + \text{c.c.} \right], \end{aligned} \quad (41)$$

where c.c. stands for the complex conjugate of the preceding quantity and

$$F_k = p_k h_k \frac{\partial \delta(x - x_m)}{\partial x} + b q_k p_k \psi_k''. \quad (42)$$

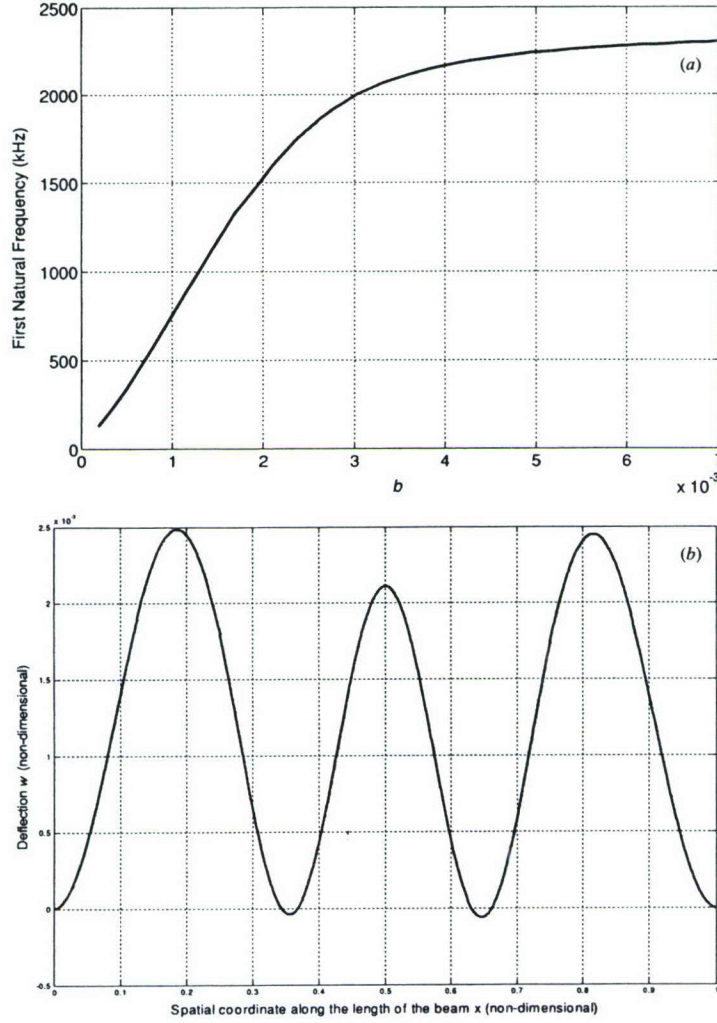


**Figure 8.** Results of nonlinear analysis: (a) first natural frequency versus  $b$ , (b) predicted forced spatial response when  $b = 4.65 \times 10^{-4}$  and (c) frequency-response curve for  $b = 4.65 \times 10^{-4}$ ,  $\hat{p} = 4.65 \times 10^{-5}$  and  $\hat{\mu} = 8.23 \times 10^{-4}$ . The solid and dashed lines represent stable and unstable branches, respectively.

The corresponding boundary and compatibility conditions at all orders are similar to those given by equations (22) and (23). The excitation frequency is assumed to be close to the first natural frequency; that is,

$$\hat{\Omega} = \hat{\omega}_1 + \varepsilon^2 \hat{\sigma}, \quad \text{or} \quad \Omega_k = \omega_{1k} + \varepsilon^2 \sigma_k. \quad (43)$$

The solution of (39) can be written as

$$\eta_{1k} = \phi_{1k}(x) [A_1(T_{1k}, T_{2k}) e^{j\omega_{1k} T_{0k}} + \bar{A}_1(T_{1k}, T_{2k}) e^{-j\omega_{1k} T_{0k}}], \quad (44)$$

where  $\bar{A}_1$  is the complex conjugate of  $A_1$ , which can be written in polar form as  $A_1(T_{1k}, T_{2k}) = \frac{1}{2} a e^{j\beta}$ . On substituting (44) into (40), the right-hand side of (40) can be expressed as the summation of terms that produce non-secular terms and secular terms (ST),

$$\mathcal{L}(\eta_{2k}) = b \Psi_k(x) [A_1^2 e^{j2\omega_{1k} T_{0k}} + A_1 \bar{A}_1 + \text{c.c.}] + \text{ST}, \quad (45)$$

where

$$\Psi_k(x) = \frac{2}{r_k^2} \left[ \sum_{i=1}^n \Lambda_{ik} (\psi'_i, \phi'_{1i})_i \right] \phi''_{1k} + \frac{1}{r_k^2} \left[ \sum_{i=1}^n \Lambda_{ik} (\phi'_{1i}, \phi'_{1i})_i \right] \psi''_k, \quad (46)$$

$$\text{ST} = -j2\omega_{1k} \phi_{1k} [D_{1k} A_1 e^{j\omega_{1k} T_{0k}} - D_{1k} \bar{A}_1 e^{-j\omega_{1k} T_{0k}}].$$

Setting the sum of the secular terms to zero one obtains  $A_1 = A_1(T_{2k})$ , and solving (45) by assuming the approximate solution for the spatial term of  $\eta_{2k}(x, t_k)$  to be a weighted summation of the free-oscillation mode shapes given by (28), one has

$$\eta_{2k} = b A_1 \bar{A}_1 \Phi_{1k}(x) + b A_1^2 \Phi_{2k}(x) e^{j2\omega_{1k} T_{0k}} + \text{c.c.}, \quad (47)$$

where  $\Phi_{1k}(x)$  and  $\Phi_{2k}(x)$  are defined as

$$\Phi_{1k}(x) = \sum_{r=1}^{\infty} T_r \phi_{rk},$$

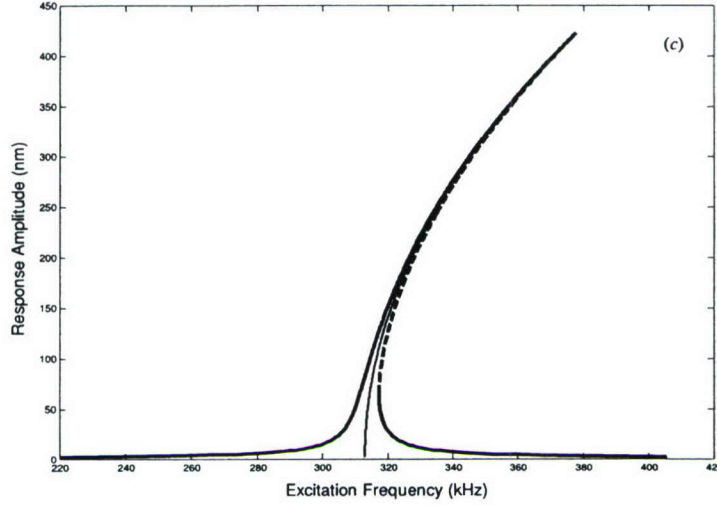


Figure 8. (Continued.)

$$T_r = \frac{\sum_{i=1}^n \sum_{k=1}^n \left[ \frac{\Delta_{ik} E A_k}{\rho A_k} \langle \psi'_i, \phi'_{1i} \rangle_i \langle (2\phi''_{1k} + \psi''_k), \phi_{rk} \rangle_k \right]}{I^2 \hat{\omega}_r^2 \langle \phi_r, \phi_r \rangle} \quad (48)$$

$$\Phi_{2k}(x) = \sum_{r=1}^{\infty} S_r \phi_{rk}, \quad (49)$$

$$S_r = \frac{\sum_{i=1}^n \sum_{k=1}^n \left[ \frac{\Delta_{ik} E A_k}{\rho A_k} \langle \psi'_i, \phi'_{1i} \rangle_i \langle (2\phi''_{1k} + \psi''_k), \phi_{rk} \rangle_k \right]}{I^2 [\hat{\omega}_r^2 - (2\hat{\omega}_1)^2] \langle \phi_r, \phi_r \rangle}.$$

Next, to solve (41), substituting (43), (44) and (47), one arrives at

$$\mathcal{L}(\eta_{3k}) = A_1^3 h_{1k}(x) e^{j3\omega_1 T_{0k}} + h_{2k}(x, T_{2k}) e^{j\omega_1 T_{0k}} + \text{c.c.}, \quad (50)$$

where

$$h_{1k}(x) = \frac{2b^2}{r_k^2} \left\{ \Phi''_{2k} \left[ \sum_{i=1}^n \Lambda_{ik} \langle \psi'_i, \phi'_{1i} \rangle_i \right] + \psi''_k \left[ \sum_{i=1}^n \Lambda_{ik} \langle \phi'_{1i}, \Phi'_{2i} \rangle_i \right] + \phi''_{1k} \left[ \sum_{i=1}^n \Lambda_{ik} \langle \psi'_i, \Phi'_{2i} \rangle_i \right] + \frac{\phi''_{1k}}{2b^2} \left[ \sum_{i=1}^n \Lambda_{ik} \langle \phi'_{1i}, \phi'_{1i} \rangle_i \right] \right\} \quad (51)$$

$$h_{2k}(x, T_{2k}) = A_1^2 \bar{A}_1 g_k(x) - 2j\omega_{1k} \phi_{1k} [\mu_k A_1 + D_{2k} A_1] + \frac{1}{2} F_k e^{j\sigma_k T_{2k}} \quad (52)$$

$$g_k(x) = \frac{2b^2}{r_k^2} \sum_{i=1}^n \left\{ \Lambda_{ik} [2\Phi''_{1k} \langle \psi'_i, \phi'_{1i} \rangle_i + \Phi''_{2k} \langle \psi'_i, \phi'_{1i} \rangle_i + 2\phi''_{1k} \langle \psi'_i, \Phi'_{1i} \rangle_i + \phi''_{1k} \langle \psi'_i, \Phi'_{2i} \rangle_i + 2\psi''_k \langle \phi'_{1i}, \Phi'_{1i} \rangle_i + \psi''_k \langle \phi'_{1i}, \Phi'_{2i} \rangle_i + \frac{3}{2b^2} \phi''_{1k} \langle \phi'_{1i}, \phi'_{1i} \rangle_i] \right\}. \quad (53)$$

The solvability condition [22] requires the right-hand side of (50) and its boundary conditions be orthogonal to every

solution of the corresponding homogeneous adjoint problem from  $x = 0$  to 1, which, from (26) and (31), is  $\phi_{rk}(x) e^{\pm j\hat{\omega}_r t}$  for the  $k$ th section and the  $r$ th mode. Multiplying the right-hand side of (50) by  $\phi_{1k}(x) e^{-j\hat{\omega}_1 t}$ , spatially integrating the result from  $x = x_{k-1}$  to  $x = x_k$ , adding all sections together, and setting the sum of the secular terms to zero, the following complex-valued modulation equation is obtained:

$$2j \left[ \sum_{k=1}^n \langle (\mu_k A_1 + D_{2k} A_1) \omega_{1k} \phi_{1k}, \phi_{1k} \rangle_k \right] = \frac{1}{2} \left[ \sum_{k=1}^n \langle F_k, \phi_{1k} \rangle_k \right] e^{j\hat{\sigma} \hat{T}_2} + A_1^2 \bar{A}_1 \left[ \sum_{k=1}^n \langle g_k, \phi_{1k} \rangle_k \right]. \quad (54)$$

Further, substituting (4) and (36) into (54), and letting  $\gamma = \hat{\sigma} \hat{T}_2 - \beta$ , it is found that the approximate solution and frequency-response equation are respectively given by

$$W = \sum_{k=1}^n W_k(x, t_k) H_k,$$

and

$$\hat{\sigma} = -\hat{\alpha}_{nn} a^2 \pm \left( \frac{\mathcal{F}^2}{4\hat{\omega}_1^2 a^2} - C^2 \hat{\mu}^2 \right)^{\frac{1}{2}}, \quad (55)$$

where

$$W_k(x, t_k) = b [\psi_k(x) + \frac{1}{2} b a^2 \Phi_{1k}(x)] + a \phi_{1k}(x) \cos(\Omega_k t_k - \gamma) + \frac{1}{2} b a^2 \Phi_{2k}(x) \cos[2(\Omega_k t_k - \gamma)] + \dots \quad (56)$$

$$\hat{\alpha}_{nn} = \sum_{k=1}^n \langle \phi_{1k}, g_k \rangle_k / \left[ 8\hat{\omega}_1 \sum_{k=1}^n \frac{\rho A_k l^4}{EI_k} \langle \phi_{1k}, \phi_{1k} \rangle_k \right],$$

$$\mathcal{F} = \sum_{k=1}^n \langle \phi_{1k}, F_k \rangle_k / \left[ \sum_{k=1}^n \frac{\rho A_k l^4}{EI_k} \langle \phi_{1k}, \phi_{1k} \rangle_k \right], \quad (57)$$

$$C = \sum_{k=1}^n \frac{1}{EI_k} \langle \phi_{1k}, \phi_{1k} \rangle_k / \left[ \sum_{k=1}^n \frac{\rho A_k}{EI_k} \langle \phi_{1k}, \phi_{1k} \rangle_k \right].$$

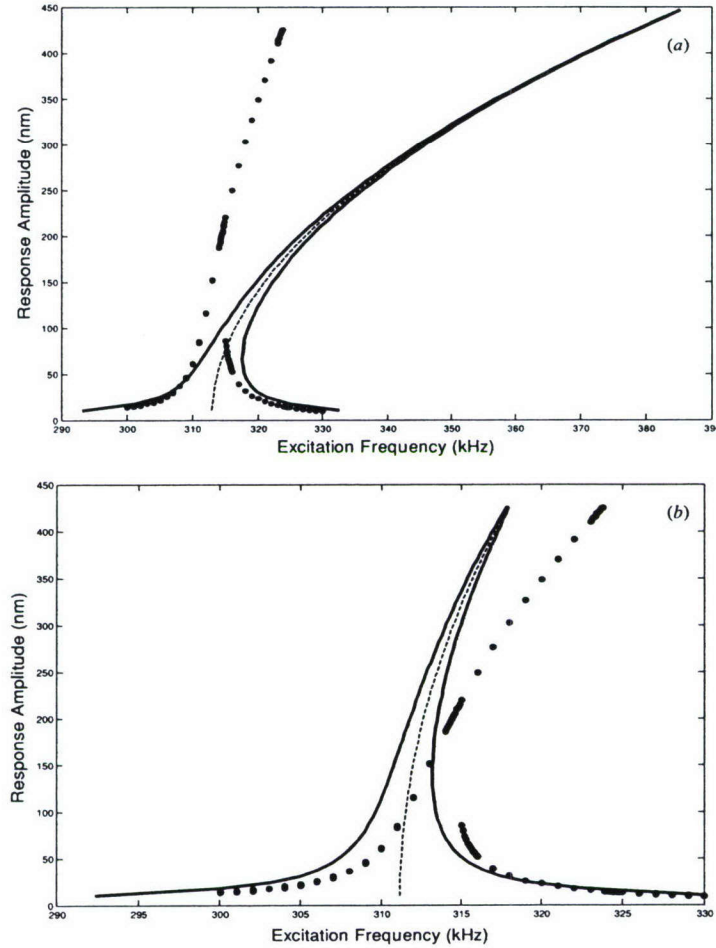


**Figure 9.** Comparisons between experimental measurements and the predicted frequency responses: (a) thickness is 90 nm,  $\hat{\mu} = 8.23 \times 10^{-4}$ ,  $b = 4.65 \times 10^{-4}$  and  $\hat{\alpha}_{nn} = -2.73 \times 10^{11}$ ; (b) thickness is 93.77 nm,  $\hat{\mu} = 8.23 \times 10^{-4}$ ,  $b = 4.65 \times 10^{-4}$  and  $\hat{\alpha}_{nn} = -2.84 \times 10^{10}$ ; (c) thickness is 140 nm,  $\hat{\mu} = 8.23 \times 10^{-4}$ ,  $b = 4.85 \times 10^{-4}$  and  $\hat{\alpha}_{nn} = -2.77 \times 10^{11}$ ; and (d) thickness is 160 nm,  $\hat{\mu} = 8.23 \times 10^{-4}$ ,  $b = 4.86 \times 10^{-4}$  and  $\hat{\alpha}_{nn} = 4.36 \times 10^{10}$ .

## 6. Results and discussion

In figure 8(a), the variation of the first natural frequency of a 200  $\mu\text{m}$  PZT resonator versus the buckling factor  $b$  is shown for free oscillations about the fifth static buckling mode. It is important to note that for the same frequency value, the corresponding value of  $b$  depends on the resonator's stiffness and geometric properties as well as the normalization used to define the static critical buckling mode shape. (Here, the normalization used for the static critical buckling mode shape  $\psi(x)$  is  $\int_0^1 \psi^2(x) dx = 1$ .) When  $b$  equals  $4.65 \times 10^{-4}$ , the first natural frequency of the resonator is determined to be 313 kHz, which is close to the experimental result given in the second section of this paper. The corresponding deflection,  $b[\psi + \frac{1}{2}ba^2\Phi_1] + a\phi_1$ , determined from equations (32) and (44), is shown in figure 8(b). In this figure, the amplitude  $a$  of mode shape  $\phi$  is scaled to be  $10^{-3}$ , so that the predicted dynamic displacement is of the same order as that seen in experiments. When the excitation frequency is close to the first natural frequency of the resonator, the predicted forced

spatial response is similar to the experimentally observed spatial pattern (see figure 4(a)). The frequency–response curve obtained from (55) is shown in figure 8(c). It resembles that of a Duffing oscillator with a hardening spring and this is qualitatively consistent with the experimental results of figure 3(b). Guided by related work [23], the damping coefficient  $\hat{\mu}$  and the excitation force amplitude  $\hat{p}$  are chosen to generate the predictions.

The agreement between the analytical predictions and experimental data suggests that the hypothesis of the non-flat equilibrium position of the resonator caused by buckling can be a valid one. The present work can be used as a basis to study buckling and oscillations of microresonators with axially stepwise varying properties. For different values of the top electrode thickness, the numerical values of  $\hat{\alpha}_{nn}$  and  $C$  are found to vary. The associated comparisons between the experimentally observed frequency response and the predicted frequency response obtained from equation (55) are given in figure 9. The dotted lines correspond to the experimental measurements and the solid lines correspond

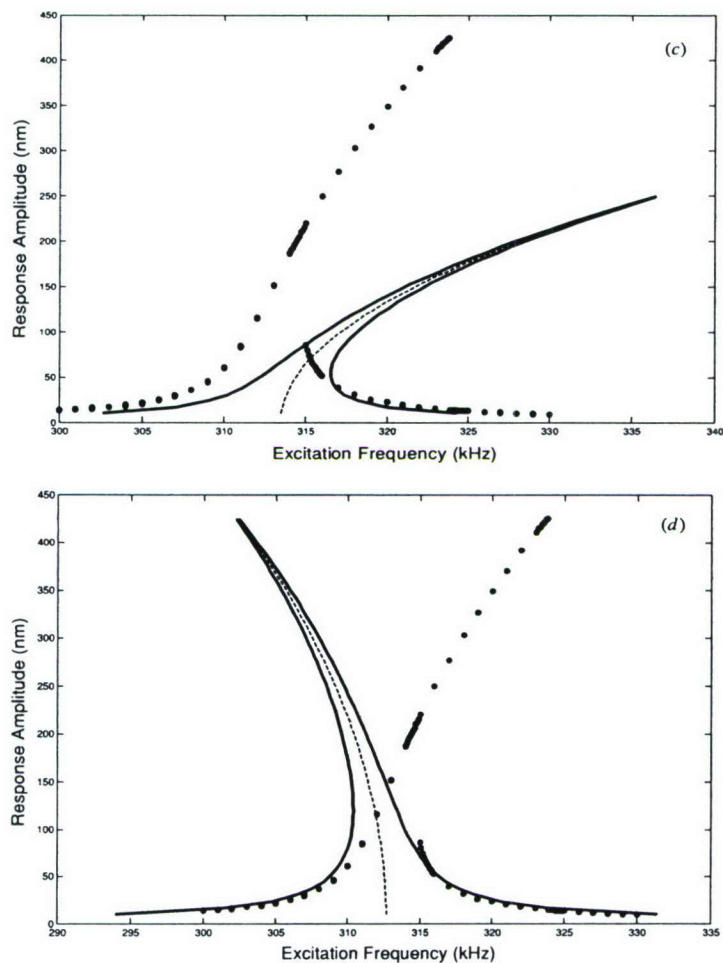


Figure 9. (Continued.)

to model predictions. It is seen that the top electrode thickness affects the frequency–response curve dramatically by changing it from hardening to softening in some cases.

### Acknowledgments

The authors gratefully acknowledge the support received for this work through DARPA contract no F3060202C0016, AFOSR grant no F49620-03-10181, and ARO grant no W911NF0510076. Material property data were obtained from researchers at the Maryland MEMS Laboratory, University of Maryland, College Park, Maryland (MD), and the Army Research Laboratory, Adelphi, MD.

### References

- [1] Lin L, Nguyen C T-C, Howe R T and Pisano A P 1992 Microelectromechanical filters for signal processing *Technical Digest, IEEE Micro Electromechanical Systems Workshop (Travemunde, Germany, 4–7 February 1992)* pp 226–31
- [2] Younis M I and Nayfeh A H 2003 A study of the nonlinear response of a resonant microbeam to an electric actuation *Nonlinear Dyn.* **31** 91–117
- [3] Balachandran B and Li H 2003 Nonlinear phenomena in microelectromechanical resonators *Proc. IUTAM Symp. on Chaotic Dynamics and Control of Systems and Processes in Mechanics (Rome, Italy, 8–13 June)* pp 97–106
- [4] Piekarski B, DeVoe D, Dubey M, Kaul R, Conrad J and Zeto R 2001 Surface micromachined piezoelectric resonant beam filters *Sensors Actuators A* **91** 313–20
- [5] DeVoe D L 2001 Piezoelectric thin film micromechanical beam resonators *Sensors Actuators A* **88** 263–72
- [6] Currano L 2002 Experimental and finite element analysis of piezoelectrically driven MEMS actuators *MS Thesis* Department of Mechanical Engineering, University of Maryland, College Park
- [7] Anderson T J, Nayfeh A H and Balachandran B 1996 Coupling between high-frequency modes and a low frequency mode: theory and experiment *Nonlinear Dyn.* **11** 17–36
- [8] Li H and Balachandran B 2002 Buckling induced nonlinear phenomenon in a micro-electromechanical resonator *Proc. ASME Int. Mechanical Engineering Congress and Exposition (Orlando, FL, 2002)* Paper No IMECE2002-39010
- [9] Preidikman S, Li H and Balachandran B 2003 Forced oscillations of microelectromechanical resonators *Proc. Symp. on Nonlinear Dynamics and Stochastic Mechanics*.

- 2003 ASME Int. Mechanics Engineering Congress and Exposition (Washington, DC, 15–21 November) Paper No IMECE2003-44552
- [10] Li H and Balachandran B 2003 Nonlinear oscillations of micromechanical oscillators *Proc. 2003 ASME Int. Design Engineering Technical Conf. (Chicago)* Paper No DETC2003/VIB-48520
- [11] Chiao M and Lin L 2000 Self-buckling of micromachined beams under resistive heating *J. Microelectromech. Syst.* **9** 146–51
- [12] Lindberg U, Soderkvist J, Lammerink T and Elwenspoek M 1998 Quasi-buckling of micromachined beams *J. Micromech. Microeng.* **3** 183–6
- [13] Fang W and Wickert J A 1994 Post-buckling of micromachined beams *J. Micromech. Microeng.* **4** 116–22
- [14] Saif M T A 2000 On a tunable bistable MEMS—theory and experiment *J. Microelectromech. Syst.* **9** 157–70
- [15] Nayfeh A H and Lacarbonara W 1998 On the discretization of spatially continuous systems with quadratic and cubic nonlinearities *JSM Int. J. C* **41** 510–31
- [16] Lacarbonara W and Nayfeh A H 1998 Experimental validations of reduction methods for nonlinear vibrations of distributed-parameter systems: analysis of a buckled beam *Nonlinear Dyn.* **17** 95–117
- [17] Li H and Balachandran B 2005 Buckling and free oscillations of composite microresonators *J. Microelectromech. Syst.* at press
- [18] Nayfeh A H and Mook D T 1979 *Nonlinear Oscillations* (New York: Wiley) pp 447–53
- [19] Li H 2006 Oscillations of microscale composite structures with applications to microresonators *PhD Dissertation* Department of Mechanical Engineering, University of Maryland, College Park
- [20] Talpaert Y R 2002 *Tensor Analysis and Continuum Mechanics* (Dordrecht: Kluwer) pp 199–209
- [21] Crawley E F and Lazarus K B 1991 Induced strain actuation of isotropic and anisotropic plates *AIAA J.* **29** 944–51
- [22] Nayfeh A H 1981 *Introduction to Perturbation Techniques* (New York: Wiley) pp 388–471
- [23] Dick A J, Balachandran B, DeVoe D L and Mote C D Jr 2005 Parametric identification of piezoelectric micro-scale resonators *Proc. ENOC-2005 (Eindhoven, Netherlands, 7–12 August 2005)*

# A semi-analytical tool based on geometric nonlinearities for microresonator design

Sergio Preidikman and Balakumar Balachandran

Department of Mechanical Engineering, University of Maryland, College Park,  
MD 20742-3035, USA

Received 22 September 2005, in final form 23 December 2005

Published 30 January 2006

Online at stacks.iop.org/JMM/16/512

## Abstract

In this paper, a computational mechanics model specifically tailored for composite microresonators with piezoelectric actuation and piezoelectric sensing is developed and used as a design tool for these microresonators. The developed model accounts for the structural properties and the electromechanical coupling effect through finite-element analysis. It is assumed that the deflection is large and that the geometric nonlinearity must be included. The dynamic admittance model is derived by combining the linear piezoelectric constitutive equations with the modal transfer function of the multi-layered microresonator structure. The resonator receptance matrix is constructed through modal summation by considering a limited number of dominant modes. The electromechanical coupling determination at the input and output ports makes use of converse and direct piezoelectric effects. In the development of the finite-element models, the boundary conditions, the shapes of electrodes and distributed parameters such as varying elastic modulus across the length of the structure have been taken into account. The developed semi-analytical tool can be used to carry out parametric studies with respect to the following: (i) the resonator beam thickness and length, (ii) the influence of constant axial forces on the transverse vibrations of clamped–clamped microresonators, (iii) the geometry of the drive and sense electrodes and (iv) imperfect boundary conditions due to mask imperfections and fabrication procedure. The semi-analytical development has been validated by comparing model predictions with prior results available in the literature for clamped–clamped resonators and experimental measurements. A detailed discussion of modeling considerations is also presented.

(Some figures in this article are in colour only in the electronic version)

## 1. Introduction

Piezoelectrically actuated microscale resonators are attractive for communication and signal-processing applications [1]. Two types of resonators are considered here. One type of resonators will be referred to as the AlGaAs resonator, and the other type of resonators will be referred to as the PZT resonator. Both types of resonators are composite structures, and the PZT resonators have asymmetric cross-sections, as discussed in previous work [2, 3]. The considered resonators are based on the piezoelectric effect, as shown in figure 1. The elastic substrate is a SiO<sub>2</sub> layer, on the top of which a platinum electrode layer is deposited throughout the length

of the structure. A thin layer of sol–gel piezoelectric film is located on the top of this electrode layer. To complete the structure, another platinum layer is deposited on the top of this piezoelectric film and this layer extends over one quarter of the length from each anchor. The mid-section of the resonator structure is free from this platinum electrode layer [1]. Due to the asymmetry of the cross-section, the position of the piezoelectric layer is offset from the neutral axis, and in addition, (tensional) residual stress may also be introduced in each layer during the fabrication process. The effect of these stresses is explored in this work.

As pointed out in the authors' recent work, the resonators also exhibit nonlinear characteristics [4–6]. These

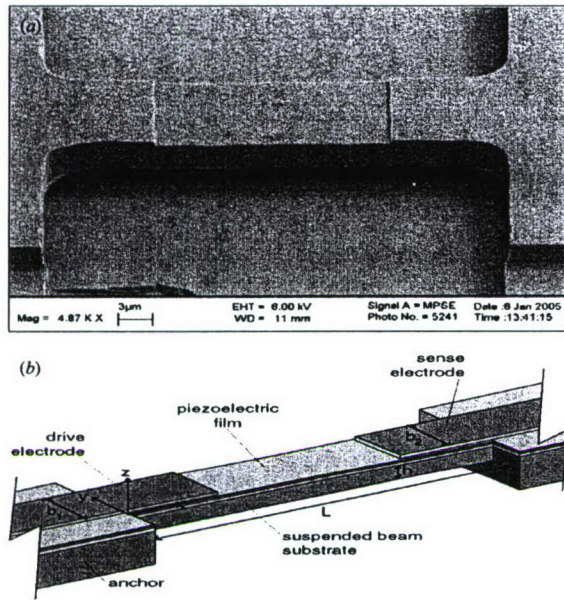


**Figure 1.** (a) SEM of a PZT resonator (courtesy, Maryland MEMS Laboratory) and (b) a schematic showing the details [2].

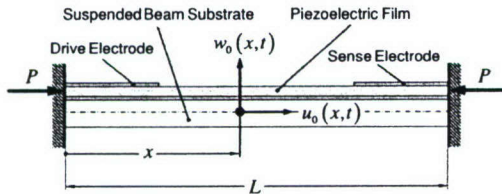


**Figure 2.** A clamped-clamped composite resonator subjected to a constant axial load  $P$ .

characteristics include Duffing oscillator-like response during resonance excitations, temporal harmonics in the response and spatial patterns during forced oscillations that cannot be explained by a conventional linear analysis. The lengths of the resonators considered in previous studies typically range from 100  $\mu\text{m}$  to 400  $\mu\text{m}$ , and the thickness of each platinum electrode is in the range of 90 nm to 180 nm [2–6]. In some typical uses of this resonator, the structure is driven close to its first resonance frequency with the input at the drive electrode having a dc bias in addition to the harmonic component.

In this work, the authors discuss a semi-analytical finite-element (e.g. [7, 8]) based formulation, in which transverse-free vibrations of composite and axially stepwise varying properties of microresonators subjected to constant axial loads are considered (see figure 2 for a clamped-clamped case). It is shown that the consideration of axial loads is important to predict the natural frequencies of the resonators observed in the experiments.

To take into account the effect of the axial load, a geometrically nonlinear analysis needs to be performed. In such a case, the equations of motion for the microresonator can be written in the following form:

$$\mathbf{M}\ddot{\mathbf{d}}(t) + \mathbf{C}\dot{\mathbf{d}}(t) + \mathbf{K}\mathbf{d}(t) = \mathbf{f}(t),$$

where  $\mathbf{K} = \mathbf{K}_E + \mathbf{K}_G$  is the global stiffness matrix,  $\mathbf{K}_E$  is the elastic stiffness matrix and  $\mathbf{K}_G$  is the geometrical stiffness matrix that is obtained from the nonlinear component of the strain–displacement relation. This matrix has not been considered in the previous studies of microelectromechanical systems (MEMS).

In the last several years, there has been a growing need for accurate modeling and simulation of microelectromechanical devices and systems that employ piezoelectric materials. This comes from the need to reduce design iterations and speed up the product development, and also to ensure reliability of the final product. Finite-element analysis (FEA) plays an important role in the simulation of MEMS devices, and this analysis generally covers multiple domains for a single device, such as structural, thermal, electrostatic, electromagnetic and fluid domains. von Preissig and Kim [9] examined techniques for modeling thin-piezoelectric MEMS devices by using existing finite-element packages. In this work, piezoelectrically actuated bending is examined. The authors point out that, while it may seem that the sheet-like nature of structures in piezoelectric MEMS would make them good candidates for conducting FEA with plate elements, solid or ‘brick’ elements can work remarkably well. Finite-element model (FEM) errors associated with the discretization of the model have also been analyzed. An important issue to note is that meshing a thin sheet into low-aspect-ratio elements requires a prohibitively large number of elements, while too low a mesh density might result in severe discretization and element-shape errors. A four-node, isoparametric, linear piezoelectric, plane-strain element from the ANSYS library has been used in this work. Wang and Ostergaard [10] used finite elements to develop a coupled simulation method for piezoelectric transducers with an attached electric circuit. In this work, the weak form of the laws of conservation of momentum and electric charge for a linear piezoelectric medium are discretized by using the FEM. Their method has been implemented in the ANSYS software. Chen *et al* [11] presented a two-dimensional analytical model of a spiral-shaped PZT ceramic actuator. They used the FEA to validate the results obtained from the analytical model. In this work, the commercially available software packages PATRAN and ABAQUS are used. PATRAN is utilized as a pre-processor and ABAQUS is used as a post-processor to perform the linear elastic, piezoelectric analysis. In order to capture bending effects accurately, the authors used eight-node, isoparametric, plane strain, linear elastic, piezoelectric elements. For achieving convergence, while keeping the length-to-width ratio of the elements reasonable, they used meshes with at least ten elements across the spiral thickness. A typical finite-element mesh of a two-turn spiral actuator has more than 3000 elements.

In this paper, the coupling of electrical and mechanical fields that is intrinsic to a piezoelectric material is accomplished in a non-traditional approach. From a filter design standpoint, the admittance function relating input voltage to output current  $I_2(\omega)/V_1(\omega)$  is an important frequency-response function to be determined (see figure 3). This admittance function may be obtained by relating the mechanical transfer function of the microresonator structure to the corresponding electrical input and output through the

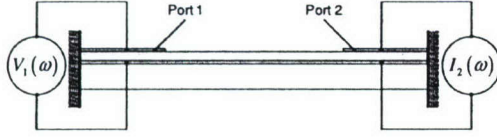


**Figure 3.** Input and output quantities of interest for a clamped-clamped piezoelectric microresonator.

piezoelectric constitutive equations. In the second section of this work, this admittance function is determined for a composite microresonator with axially stepwise varying properties. This microresonator is also subjected to constant axial loads. The obtained admittance function has the form

$$Y_{21}(\omega) = \frac{I_2(\omega)}{V_1(\omega)} = \mathbf{C}^S(\omega) \mathbf{H}^{SA}(\omega) \mathbf{F}^A,$$

where  $\mathbf{H}^{SA}(\omega)$  is a ‘block’ of the complex frequency response matrix for the considered microresonator (e.g. [7]);  $\mathbf{C}^S(\omega)$  is a matrix that depends on the material properties of the PZT material, the geometry of the sensor and the finite-element discretization of the microresonator, and  $\mathbf{F}^A$  is a vector that depends on the material properties of the PZT, the geometry of the actuator, the geometry of the suspended beam substrate and the finite-element discretization of the microresonator. In the second section and the appendices, the expressions for these matrices/vectors are derived. Comparisons with experimental results and results available in the literature are presented in the third section. It is believed that the numerical and analytical efforts presented in this work can be used as a basis to develop design tools for piezoelectric microresonators.

## 2. Semi-analytical development

### 2.1. The equations of motion in the frequency domain

The equations of motion of the microresonator in the frequency domain are of the form

$$\{-\omega^2 \mathbf{M} + j\omega \mathbf{C} + \mathbf{K}\} \mathbf{d}(\omega) = \mathbf{f}(\omega), \quad (1)$$

where  $j = \sqrt{-1}$ ,  $\mathbf{K} = \mathbf{K}_E + \mathbf{K}_G$  is the global stiffness matrix,  $\mathbf{M}$ ,  $\mathbf{K}_E$  and  $\mathbf{K}_G$  are the global mass matrix, elastic stiffness matrix and geometrical stiffness matrix, respectively, and  $\mathbf{d}(\omega)$  and  $\mathbf{f}(\omega)$  are the Fourier transforms of the nodal displacements  $\mathbf{d}(t)$  and the nodal forces  $\mathbf{f}(t)$ , respectively. The development of the time-domain model with the geometric nonlinearity is detailed in appendix A. From (1), one obtains

$$\mathbf{d}(\omega) = \mathbf{H}(\omega) \mathbf{f}(\omega), \quad (2)$$

where

$$\mathbf{H}(\omega) = \{-\omega^2 \mathbf{M} + j\omega \mathbf{C} + \mathbf{K}\}^{-1} \quad (3)$$

is the complex frequency response matrix (the mechanical force–displacement transfer function) of the beam microresonator [7]. Since proportional damping is assumed, the complex frequency response matrix can be constructed from the modal summation as [12]

$$\mathbf{H}(\omega) = [H_{rs}(\omega)] = \left[ \sum_{l=1}^{n_{\text{mod}}} \frac{\phi_{lr} \phi_{ls}}{\omega_l^2 [1 - (\omega/\omega_l)^2 + j2\zeta_l(\omega/\omega_l)]} \right], \quad (4)$$

where  $r, s = 1, 2, \dots, n_{\text{dof}}$ ,  $n_{\text{dof}}$  is the number of degrees of freedom (dof) of the finite-element model,  $\omega_l$  is the  $l$ th natural frequency of the undamped system and  $\zeta_l$  is the  $l$ th damping ratio of the microresonator, which is given by

$$\zeta_l = \frac{1}{2\omega_l} (\alpha + \beta\omega_l). \quad (5)$$

In (4),  $\phi_{lr}$  and  $\phi_{ls}$  are, respectively, the  $r$ -component and the  $s$ -component of the  $l$ th mass normalized mode shape of the microresonator and these modes satisfy

$$\varphi_m^T \mathbf{M} \varphi_n = \delta_{mn}, \quad \varphi_m^T \mathbf{K} \varphi_n = \delta_{mn} \omega_m^2. \quad (6)$$

Further, in (4),  $n_{\text{mod}}$  is the number of dominant modes. The natural frequencies and mode shapes in (4) are determined from

$$\mathbf{K} \Phi = \mathbf{M} \Phi \Lambda, \quad (7)$$

where

$$\Phi = [\varphi_1 \varphi_2 \dots \varphi_{n_{\text{mod}}}], \quad \Lambda = [\delta_{mn} \omega_m^2]. \quad (8)$$

The damping ratio in (4) is, in general, determined experimentally from the measured quality factor,  $Q_l$ , which is given by

$$Q_l = \frac{\sqrt{\Omega_{\text{cu}} \Omega_{\text{cl}}}}{\Omega_{\text{cu}} - \Omega_{\text{cl}}}, \quad (9)$$

where the cutoff frequencies are given by [13]

$$\Omega_{\text{cl}} = \sqrt{1 - 2\zeta_l^2 - 2\zeta_l \sqrt{1 - \zeta_l^2}}, \quad (10a)$$

$$\Omega_{\text{cu}} = \sqrt{1 - 2\zeta_l^2 + 2\zeta_l \sqrt{1 - \zeta_l^2}}. \quad (10b)$$

After substituting (10) into (9) and using a Taylor’s series expansion about  $Q_l = 0$ , the result obtained is

$$Q_l = \frac{1}{2\zeta_l} - \frac{3}{2}\zeta_l - \frac{9}{4}\zeta_l^3 + O(\zeta_l^4). \quad (11)$$

Hence, for very lightly damped microresonators (high- $Q$  microresonators), that is,  $0 < \zeta \ll 1$ , the quality factor can be approximated as

$$Q_l \cong \frac{1}{2\zeta_l}. \quad (12)$$

Now, in terms of the quality factors, it is possible to rewrite the dof-to-dof mechanical complex frequency response function of the microresonator structure,  $H_{rs}(\omega)$ , as

$$H_{rs}(\omega) = \sum_{l=1}^{n_{\text{mod}}} \frac{\phi_{lr} \phi_{ls}}{\omega_l^2 [1 - (\omega/\omega_l)^2 + j/Q_l(\omega/\omega_l)]}. \quad (13)$$

At this point, one has the elements of the complex frequency response matrix, which describes the resulting harmonic displacement of the  $r$ th dof caused by a unit harmonic force applied at the  $s$ th dof.

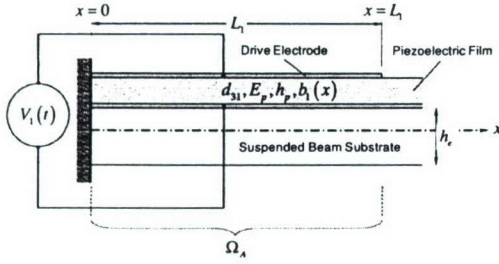


Figure 4. A schematic view of the actuator port.

## 2.2. Admittance model

In this section, a semi-analytical model describing the admittance function for a clamped-clamped piezoelectric microresonator is developed. The semi-analytical admittance model may be obtained by relating the (numerical) mechanical transfer function of the microresonator structure to the corresponding electrical input and output through the (analytical) piezoelectric constitutive equations. The overall frequency-response function describing the admittance  $Y_{21}(\omega)$  between the driven input (port 1) and the sense output (port 2) of the beam resonator shown in figure 3 is defined as

$$Y_{21}(\omega) = \frac{I_2(\omega)}{V_1(\omega)}, \quad (14)$$

where  $V_1(\omega)$  is the voltage applied to the input port and  $I_2(\omega)$  is the current measured at the output port.

## 2.3. Actuator side

In this work, the active film under consideration is considered to be long, narrow and thin, so as to make the length  $L_1$  much greater than the maximum value of the width  $b_1(x)$ , which is much greater than the thickness  $h_p$  (figure 4). Next, attention is focused on the case when the active film is driven by an ac voltage  $V_1(t)$ . The externally transverse distributed force  $f_w(x, t)$  can be expressed in terms of the drive voltage  $V_1(t)$  as

$$f_w(x, t) = \frac{1}{2} d_{31} E_p h_e \frac{d^2 b_1(x)}{dx^2} V_1(t) H(x), \quad (15)$$

where  $H(x) = U(x) - U(x - L_1)$ , and  $U(x - a)$  is the Heaviside step function. The basis for (15) is detailed in appendix B.

In view of (15), the generalized element nodal forces,  $\mathbf{f}_1^e(t)$  and  $\mathbf{f}_2^e(t)$ , can be written in terms of the drive voltage  $V_1(t)$  as  $\mathbf{f}_1^e(t) = \mathbf{0}_{2 \times 1}$ ,

$$\mathbf{f}_2^e(t) = \left\{ \frac{1}{2} d_{31} E_p h_e \int_{\Omega_e} \frac{d^2 b_1(x)}{dx^2} \mathbf{N}_2(x) dx \right\} V_1(t), \quad \Omega_e \subseteq \Omega_A, \quad (16)$$

where  $\mathbf{N}_2(x)$  is a shape function matrix, as discussed in appendix A. Further,  $\Omega_A = \{x \mid 0 \leq x \leq L_1\}$  denotes the sub-domain of  $[0, L]$  occupied by the sensor (figure 5). In the frequency domain, (16) becomes

$$\mathbf{f}_1^e(\omega) = \mathbf{0}_{2 \times 1},$$

$$\mathbf{f}_2^e(\omega) = \left\{ \frac{1}{2} d_{31} E_p h_e \int_{\Omega_e} \frac{d^2 b_1(x)}{dx^2} \mathbf{N}_2(x) dx \right\} V_1(\omega), \quad \Omega_e \subseteq \Omega_A, \quad (17)$$

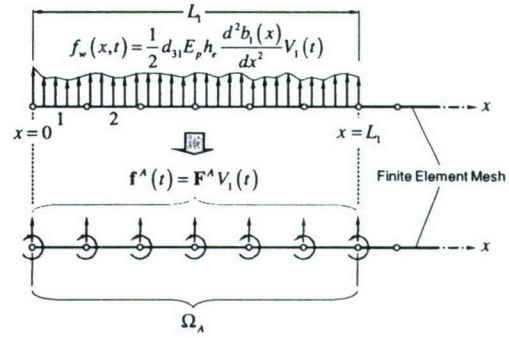


Figure 5. An external, transverse distributed force and generalized finite element nodal forces.

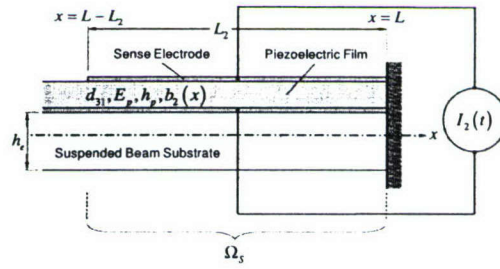


Figure 6. A schematic view of the sensor port.

or

$$\mathbf{f}_1^e(\omega) = \mathbf{0}_{2 \times 1}, \quad \mathbf{f}_2^e(\omega) = \mathbf{F}_2^e V_1(\omega), \quad \Omega_e \subseteq \Omega_A, \quad (18)$$

where  $V_1(\omega)$ ,  $\mathbf{f}_1^e(\omega)$  and  $\mathbf{f}_2^e(\omega)$  are the Fourier transforms of  $V_1(t)$ ,  $\mathbf{f}_1^e(t)$  and  $\mathbf{f}_2^e(t)$ , respectively, and  $\mathbf{F}_2^e$  is the frequency-independent vector of generalized element nodal forces defined as

$$\mathbf{F}_2^e = \frac{1}{2} d_{31} E_p h_e \int_{\Omega_e} \frac{d^2 b_1(x)}{dx^2} \mathbf{N}_2(x) dx, \quad \Omega_e \subseteq \Omega_A. \quad (19)$$

By using (17) and the assembly operator, the sub-vector of generalized equivalent nodal forces can be written as follows:

$$\mathbf{f}^A(\omega) = \mathbf{A}_e \begin{Bmatrix} \mathbf{0}_{2 \times 1} \\ \mathbf{F}_2^e \end{Bmatrix} V_1(\omega) = \mathbf{F}^A V_1(\omega), \quad e \in \Omega_A. \quad (20)$$

## 2.4. Sensor side

On the sensor side, the attention is focused on the direct piezoelectric effect. As described before, a key to developing a useful electromechanical model of a piezoelectric model is the determination of changes in electrode charges when the active film is strained due to the mechanical excitation of the microresonator. At the sensor port, it is also considered that the active film is long, narrow and thin, so as to make the length  $L_2$  much greater than the maximum value of the width  $b_2(x)$ , which in turn is much greater than the thickness  $h_p$  (figure 6).

Considering the relation between the output charge and the output current given by (B.7) in the frequency domain, the expression for the output current becomes

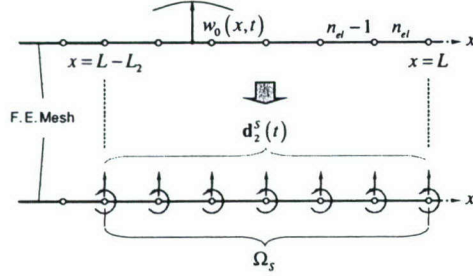


**Figure 7.** Transverse displacements of the centroidal axis and generalized finite-element nodal displacements.

$$I_2(\omega) = j\omega Q_2(\omega) = j\omega d_{31} E_p \int_{L-L_2}^L b_2(x) \left[ \frac{\partial u_0(x, \omega)}{\partial x} - \frac{h_e}{2} \frac{\partial^2 w_0(x, \omega)}{\partial x^2} \right] dx. \quad (21)$$

The integral in (21) can be split as

$$\int_{L-L_2}^L b_2(x) \frac{\partial u_0(x, \omega)}{\partial x} dx = \sum_e \int_{\Omega_e} b_2(x) \frac{\partial u_0(x, \omega)}{\partial x} dx, \\ \int_{L-L_2}^L b_2(x) \frac{\partial^2 w_0(x, \omega)}{\partial x^2} dx = \sum_e \int_{\Omega_e} b_2(x) \frac{\partial^2 w_0(x, \omega)}{\partial x^2} dx, \\ \Omega_e \subseteq \Omega_S \quad (22)$$

where  $\Omega_S = \{x \mid L - L_2 \leq x \leq L\}$  denotes the sub-domain of  $[0, L]$  occupied by the sensor port (figure 7). After using (A20a) and (A20c), one obtains

$$\int_{\Omega_e} b_2(x) \frac{\partial u_0(x, \omega)}{\partial x} dx = \left[ \int_{\Omega_e} b_2(x) \frac{\partial \mathbf{N}_1(x)}{\partial x} dx \right] \mathbf{d}_1^e(\omega), \\ \int_{\Omega_e} b_2(x) \frac{\partial^2 w_0(x, \omega)}{\partial x^2} dx = \left[ \int_{\Omega_e} b_2(x) \frac{\partial^2 \mathbf{N}_2(x)}{\partial x^2} dx \right] \mathbf{d}_2^e(\omega). \quad (23)$$

Hence, the expression for the output current becomes

$$I_2(\omega) = \sum_e \left[ \mathbf{A}^e(\omega) \mathbf{d}_1^e(\omega) + \mathbf{B}^e(\omega) \mathbf{d}_2^e(\omega) \right] = \mathbf{C}^S(\omega) \mathbf{d}^S(\omega), \quad e \in \Omega_S, \quad (24)$$

where the sub-matrices  $\mathbf{A}^e(\omega)$  and  $\mathbf{B}^e(\omega)$  are given by

$$\mathbf{A}^e(\omega) = j\omega d_{31} E_p \int_{\Omega_e} b_2(x) \frac{\partial \mathbf{N}_1(x)}{\partial x} dx, \quad \forall \Omega_e \subseteq \Omega_S, \\ \mathbf{B}^e(\omega) = -j\omega \frac{h_e}{2} d_{31} E_p \int_{\Omega_e} b_2(x) \frac{\partial^2 \mathbf{N}_2(x)}{\partial x^2} dx, \quad \forall \Omega_e \subseteq \Omega_S. \quad (25)$$

At this point, it is convenient to rewrite the system (2) in the following block-partitioned form:

$$\begin{Bmatrix} \mathbf{d}^A(\omega) \\ \mathbf{d}^M(\omega) \\ \mathbf{d}^S(\omega) \end{Bmatrix} = \begin{bmatrix} \mathbf{H}^{AA}(\omega) & \mathbf{H}^{AM}(\omega) & \mathbf{H}^{AS}(\omega) \\ \mathbf{H}^{MA}(\omega) & \mathbf{H}^{MM}(\omega) & \mathbf{H}^{MS}(\omega) \\ \mathbf{H}^{SA}(\omega) & \mathbf{H}^{SM}(\omega) & \mathbf{H}^{SS}(\omega) \end{bmatrix} \begin{Bmatrix} \mathbf{f}^A(\omega) \\ \mathbf{f}^M(\omega) \\ \mathbf{f}^S(\omega) \end{Bmatrix} \quad (26)$$

where  $A$  stands for ‘actuator’,  $M$  for ‘midspan’ and  $S$  for ‘sensor’ (figure 8).

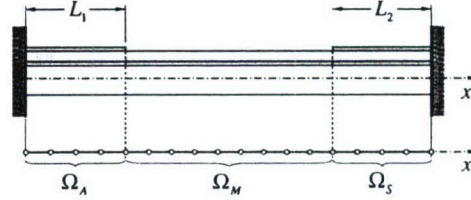


**Figure 8.** A schematic view of the clamped–clamped piezoelectric microresonator and the finite-element mesh.

By considering that in the present case, both  $\mathbf{f}^M(\omega)$  and  $\mathbf{f}^S(\omega)$  are equal to zero, and using (20), it is possible to express  $\mathbf{d}^S(\omega)$  in terms of the mechanical force–displacement transfer function and the driven voltage as follows:

$$\mathbf{d}^S(\omega) = \mathbf{H}^{SA}(\omega) \mathbf{f}^A(\omega) = \mathbf{H}^{SA}(\omega) \mathbf{F}^A V_1(\omega). \quad (27)$$

Finally, combining (24) and (27), the admittance function  $Y_{21}(\omega)$  relating input voltage to output current can be expressed as

$$Y_{21}(\omega) = \frac{I_2(\omega)}{V_1(\omega)} = \mathbf{C}^S(\omega) \mathbf{H}^{SA}(\omega) \mathbf{F}^A. \quad (28)$$

### 3. Experimental results, comparisons and discussion

The developed coupled model enables one to investigate the following: (i) the elastic stability of the resonator, (ii) the influence of a constant axial force on the transverse vibrations of a clamped–clamped resonator structure and (iii) the influence of a constant axial force on the transverse vibrations of a free–free structure.

#### 3.1. Pre-stressed microresonators

A case of interest is one where the geometric stiffness is driven by a parameter  $\lambda$ ; for example, in the case of a microresonator subjected to an initial axial force  $P_0$  due to residual stresses introduced during the fabrication of the resonators [14–16], one can write

$$P_e = \lambda P_0, \quad e = 1, 2, \dots, n_{e1} \quad (29)$$

where  $P_e$  is the axial force in the  $e$ th element and the number of elements is  $n_{e1}$ . The geometric stiffness is itself proportional to this parameter

$$\mathbf{K}_G = \lambda \mathbf{K}_G^*. \quad (30)$$

The eigenvalues of the resulting problem

$$(\mathbf{K}_E + \lambda \mathbf{K}_G^*) \varphi_n = \omega_m^2 \mathbf{M} \varphi_n \quad (31)$$

then become functions of  $\lambda$ . When  $\omega_m = 0$ , one gets an eigenproblem with eigenvalues  $\lambda_m$  corresponding to the critical loads,

$$\mathbf{K}_E \psi_n = -\lambda_m \mathbf{K}_G^* \psi_n. \quad (32)$$

The eigenvalue  $\lambda_1$  of the lowest mode yields the pre-stress state

$$P_{e,cr} = \lambda_1 P_0, \quad e = 1, 2, \dots, n_{e1} \quad (33)$$

in which the system buckles. For free–free microresonators, one has an unconstrained structure, since the stiffness matrix

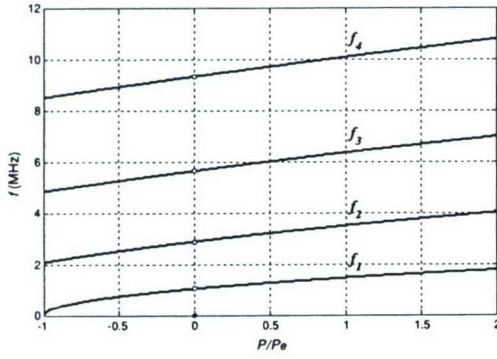


**Figure 9.** Variations of natural frequencies with an axial load for an AlGaAs microresonator (length = 120  $\mu\text{m}$ , width = 15  $\mu\text{m}$ ,  $L_1 = L_2 = 30 \mu\text{m}$ ,  $Q = 565$ ,  $n_{el} = [10 \ 20 \ 10]$ ,  $f_{0,j} = [1.0427, 2.8743, 5.6348, 9.3146]$  kHz).

**Table 1.** Characteristics of an AlGaAs resonator.

Layer	Thickness $h_k$ ( $\mu\text{m}$ )	Residual stress $\sigma_0$ (MPa)
Top AlGaAs:Si	0.5	-80
Middle AlGaAs (undoped)	1.5	-80
Bottom AlGaAs:Si	2.0	-80

is singular. In this case, there are two zero frequencies for the rigid-body degrees of freedom and one more zero frequency when the compressive load equals the buckling load. To remove the rigid-body modes from the solution of the semi-definite eigenvalue problem  $(\mathbf{K}_E + \lambda \mathbf{K}_G^*)\varphi_n = \omega_m^2 \mathbf{M}\varphi_n$ , one can perform a shift  $\mu > 0$  on  $\mathbf{K}_E + \lambda \mathbf{K}_G^*$  by calculating

$$\mathbf{K}_E + \lambda \mathbf{K}_G^* + \mu \mathbf{M}, \quad (34)$$

and then, considering the positive definite eigenproblem

$$(\mathbf{K}_E + \lambda \mathbf{K}_G^* + \mu \mathbf{M})\xi_n = \sigma_m^2 \mathbf{M}\xi_n, \quad (35)$$

where  $\xi_n = \varphi_n$  and  $\sigma_m^2 = \omega_m^2 + \mu \Rightarrow \omega_m^2 = \sigma_m^2 - \mu$ .

### 3.2. Influence of a constant axial force on the transverse vibrations of a clamped-clamped resonator structure

In figure 9, for a clamped-clamped AlGaAs resonator, the variations of the first four natural frequencies are shown with respect to the axial load. As expected, as the axial stretching load increases, the natural frequencies increase. Similarly, they decrease with the increase of the compressive axial load.

When the compressive axial force reaches the value of the Euler's buckling load,  $P_{cr} = 1.2489 \times 10^{-2}$  N, the first natural frequency goes to zero. The composite material properties and layer thickness values for the considered AlGaAs resonators are listed in table 1. Each AlGaAs microresonator has a particular orientation on the wafer. The orientation on the wafer is indicated, with respect to a reference orientation, by the so-called wafer-angle and this in turn leads to a certain crystallographic direction of the AlGaAs structure. The variation of the first natural frequency shown in table 2 has been obtained from experimental measurements for different resonators.

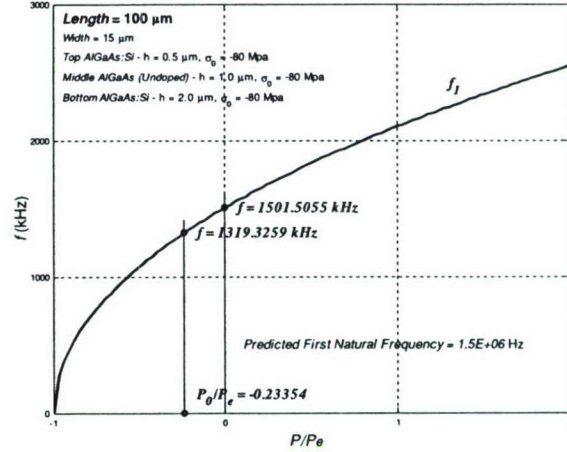


**Figure 10.** Variation of the first natural frequency with an axial load  $P/P_e$  for a clamped-clamped AlGaAs resonator ( $L_1 = L_2 = 25 \mu\text{m}$ ).

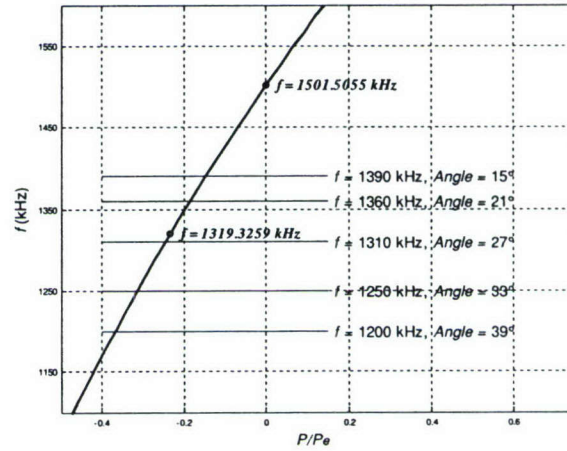


**Figure 11.** An expanded plot of figure 5 in the vicinity of the first natural frequency of the AlGaAs resonator predicted without residual stresses.

**Table 2.** Experimentally obtained first natural frequencies for different resonator lengths and wafer angles.

Length	Angle				
	15°	21°	27°	33°	39°
80 $\mu\text{m}$	2130 kHz	2070 kHz	2040 kHz	1970 kHz	1890 kHz
100 $\mu\text{m}$	1390 kHz	1360 kHz	1310 kHz	1250 kHz	1200 kHz
120 $\mu\text{m}$	960 kHz	920 kHz	900 kHz	860 kHz	830 kHz

As a representative example, a 100  $\mu\text{m}$  long resonator with a 15  $\mu\text{m}$  width is considered. From the results shown in figure 10, it can be seen that the numerically calculated value of the first natural frequency is 1501.5 kHz, in the absence of axial stresses. The first natural frequency value shifts to 1319.3 kHz, when the experimentally obtained values of residual stresses are included in the model. In figure 11, an expanded plot of a portion of figure 10 is shown. The horizontal lines represent the experimentally obtained values of the first natural frequency corresponding to the 100  $\mu\text{m}$

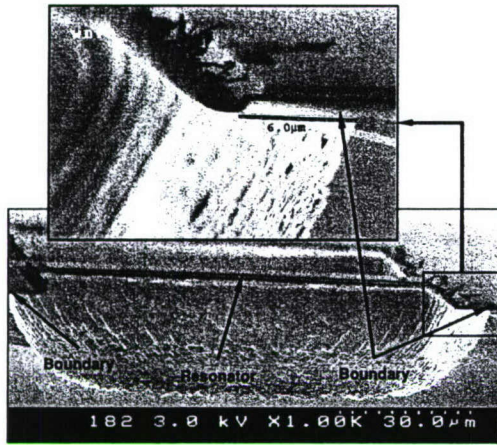


Figure 12. SEM of undercut introduced in a resonator anchor by the etching processes during fabrication (courtesy, ARL, Adelphi, MD).

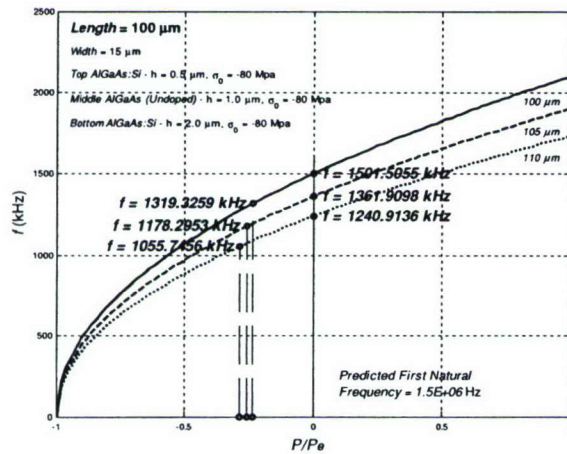


Figure 13. Variation of the first natural frequency with an axial load  $P/P_e$  for a clamped-clamped AlGaAs resonator.

resonator for different wafer angles. It can be seen that the numerically obtained values fall within the range of experimental measurements, which are listed in table 2.

### 3.3. Imperfect boundary conditions due to mask imperfections and fabrication procedure

As a second example, the effect of a 2.5 μm to 5 μm undercut introduced in each resonator anchor by the etching processes during fabrication [17] is considered (for illustrative purposes only, see figure 12).

Resonators of 105 μm and 110 μm lengths were studied to model the effect of the undercut. In figure 13, the variation of the first natural frequency with respect to the axial load is shown for 100 μm, 105 μm and 110 μm long microresonators. The experimentally obtained values of the first natural frequencies are also shown in the figure as horizontal lines for making the comparisons. In figure 14, an expanded portion of figure 13 is shown around the 1400 kHz range.

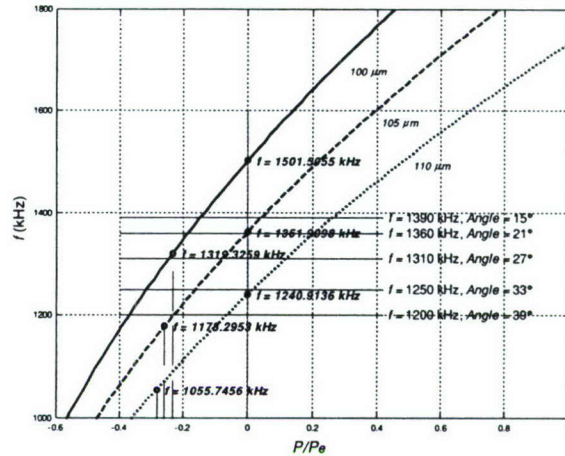


Figure 14. An expanded plot of figure 13 around 1400 kHz.

Here, the undercut has been simply modeled as an increase in the extension of the microresonator length. The change in the cross-section area is not considered in this one-dimensional model. This effect has been included in a series of two-dimensional models developed by the authors, and in these models, it is recognized that the undercut region cannot just be modeled as a beam. Rather, a more refined finite-element model with plate elements needs to be used to model more realistic boundary conditions which include changes in the cross-section area.

### 3.4. Material property variations from manufacturing uncertainties

As a third example, the effect of a ±10% varying elastic modulus across the length of the multi-layered microresonator is considered. For micromechanical resonators, these uncertainties in material properties come, in large, partly due to the manufacturing process [17]. A resonator of 120 μm length is studied to model the effect of the varying elastic modulus. In figure 15, the variation of the first natural frequency with respect to the axial load is shown for 90%  $E$ ,  $E$  and 110%  $E$ . The experimentally obtained values of the first natural frequencies are also shown in the figure as horizontal lines for making the comparisons. In figure 16, an expanded portion of figure 15 is shown around the 900 kHz range. For all wafer angles, the measured average residual stresses are the same and they equal -80 MPa.

The residual stresses are based on lattice structure measurements, and these values were provided to the authors by researchers in the Maryland MEMS Laboratory. Wafer bow measurements have also been used to measure residual stresses in this type of multi-layered microstructures [18].

### 3.5. Predictions of frequency response

The shapes of the drive and sense electrodes affect the resonator admittance through  $b_1(x)$  and  $b_2(x)$  in (19) and (25). For the resonators shown in this work, maximum electromechanical coupling is desired; that is, the electrodes must be shaped such that  $Y_{21}(\omega)$  is maximized. This may be

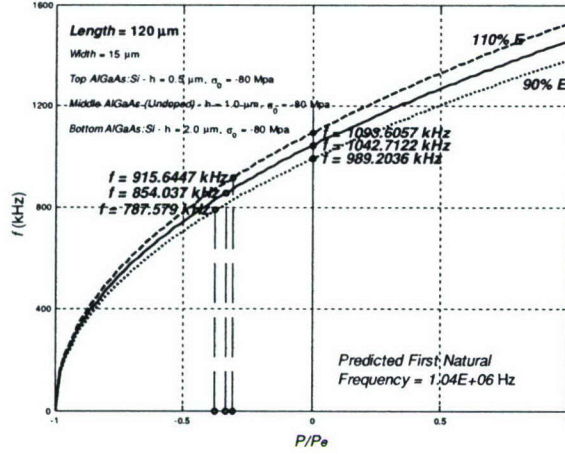


**Figure 15.** Variation of the first natural frequency with an axial load  $P/P_e$  for a clamped-clamped AlGaAs resonator.

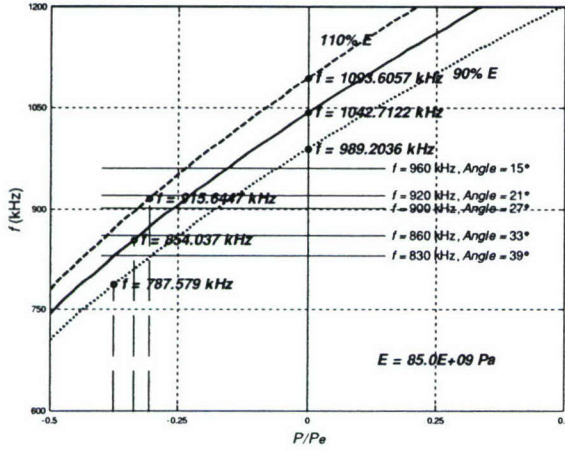


**Figure 16.** An expanded plot of figure 15 around 900 kHz.

achieved by clipping the electrodes at the quarter beam points, as depicted in figure 1(b). For this electrode geometry,  $b_1(x)$  and  $b_2(x)$  can be written as

$$b_1(x) = b \left[ U(x) - U\left(x - \frac{L}{4}\right) \right] = b g_1(x), \quad (36a)$$

$$b_2(x) = b \left[ U\left(x - \frac{3L}{4}\right) - U(x - L) \right] = b g_2(x), \quad (36b)$$

where  $b$  is the nominal width of both electrodes and  $U(x)$  is the Heaviside unit step function. By using (36), the terms in (19) and (25) involving the electrode shapes simplify to

$$\mathbf{F}_2^e = \left( \frac{1}{2} d_{31} E_p h_e b \right) \int_{\Omega_e} \frac{d^2 g_1(x)}{dx^2} \mathbf{N}_2(x) dx \quad (37)$$

and

$$\begin{aligned} \mathbf{A}^e(\omega) &= j\omega \left( \frac{1}{2} h_e d_{31} E_p b \right) \frac{2}{h_e} \int_{\Omega_e} g_2(x) \frac{\partial \mathbf{N}_1(x)}{\partial x} dx, \\ \mathbf{B}^e(\omega) &= -j\omega \left( \frac{1}{2} h_e d_{31} E_p b \right) \int_{\Omega_e} g_2(x) \frac{\partial^2 \mathbf{N}_2(x)}{\partial x^2} dx. \end{aligned} \quad (38)$$

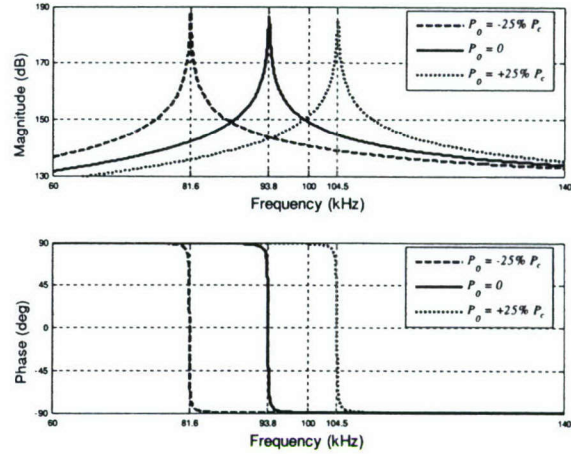


**Figure 17.** The response of a 400  $\mu\text{m}$  AlGaAs resonator for three different values of the axial load ( $Q = 565$ ,  $P_e = 7.4930 \times 10^{-4}$  N,  $L_1 = L_2 = 100 \mu\text{m}$ ,  $NE = [10 \ 20 \ 10]$ ,  $f_1 = [81.59 \ 93.84 \ 104.55]$  kHz).

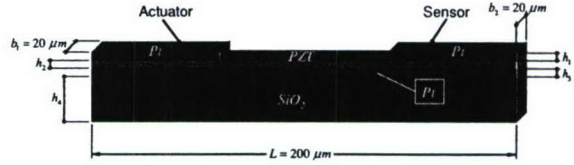


**Figure 18.** PZT microresonator characteristics.

**Table 3.** Material properties for finite-element modeling.

Material	Young's modulus $E$ (GPa)	Density $\rho$ ( $\text{kg m}^{-3}$ )	Poisson's ratio $\nu$
Pt	160–190	18 000	0.35
PZT	25 or 35	8 800	0.30
SiO <sub>2</sub>	100	2 200	0.27

In figure 17, for a 400  $\mu\text{m}$  doubly clamped AlGaAs resonator with quarter-beam electrodes, the response (magnitude and phase of the normalized admittance function  $Y_{21}(\omega)/(\frac{1}{2}d_{31}E_p h_e b)^2$ ) is shown for three different values of the axial load. As expected, as the axial stretching load increases, the first natural frequency increases. Similarly, it decreases with the increase of the compressive axial load. The composite material properties and layer thickness values for the considered AlGaAs resonators are listed in table 1.

As a second example, a 200  $\mu\text{m}$  clamped-clamped PZT resonator with quarter-beam electrodes (see figure 18) is considered and the responses obtained for three different values of the axial load are shown in figure 19. Again, as expected, as the axial stretching load increases, the first natural frequency increases. Similarly, it decreases with the increase of the compressive axial load. The material properties and geometric properties used for finite-element modeling of the considered PZT resonator are listed in tables 3 and 4, respectively.

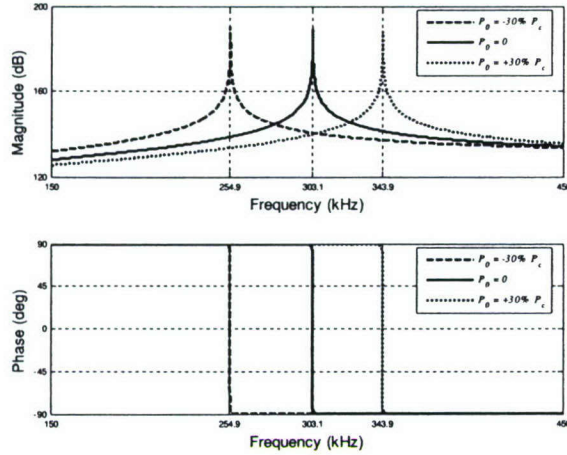


**Figure 19.** The response of a 200  $\mu\text{m}$  PZT microresonator for three different values of the axial load ( $Q = 4000$ ,  $P_c = 3.3338 \times 10^{-3}$  N,  $L_1 = L_2 = 50$   $\mu\text{m}$ ,  $NE = [10\ 20\ 10]$ ,  $f_1 = [255\ 303\ 344]$  kHz).

**Table 4.** Geometric properties for finite-element modeling.

Layer	Thickness $h_k$
SiO <sub>2</sub>	1.0602 $\mu\text{m}$
Bottom Pt	135.0 nm
PZT	0.5303 $\mu\text{m}$
Top Pt	200.0 nm

#### 4. Summary

In this work, a semi-analytical computational mechanics model of a composite microstructure with piezoelectric actuation and piezoelectric sensing has been developed as a design tool for microresonators. The developed dynamic model of microresonators accounts for structural properties and the electromechanical coupling effect through finite-element analysis. The dynamic admittance model is derived by combining the linear piezoelectric constitutive equations with the modal transfer function of the multi-layered microresonator structure. The resonator receptance matrix is constructed through modal summation by considering only a limited number of dominant modes. The electromechanical coupling determination at the input and output ports makes use of the converse and direct piezoelectric effects. The developed model has been validated by comparing it with results available in the literature for clamped-clamped resonators. The numerical results are found to be in good agreement with the experimental measurements. The numerical simulations show that the consideration of axial loads is important to predict the natural frequencies of the resonators studied in the experiments. A detailed discussion of modeling considerations has also been presented. The microresonators studied in this work, which are used as micromechanical filters, are important for mobile communication systems and signal processing applications. It is believed that the numerical and analytical efforts presented in this work can be used as a basis to develop design tools for such systems.

#### Appendix A. The finite-element model

In this appendix, a geometrically nonlinear finite-element analysis (e.g. [19, 20]) is carried out to study transverse vibrations of clamped-clamped and free-free resonators subjected to constant axial loads. This is done in the context of a planar beam, but a similar development can be carried out for the three-dimensional case. As discussed earlier, the consideration of axial loads is important to predict the first natural frequencies of the resonators observed in the experiments. In addition, as also shown, the developed model and the numerical implementation can be used to understand the influence of uncertainties associated with the fabrication process. The effect of curvature shortening (e.g. [21]) is incorporated in the developed numerical code.

##### A.1. Kinematics of the motion

The equations governing the bending of Euler-Bernoulli beams with moderately large rotations but with small strains can be derived using the following *linearized* displacement field

$$u_1 = u_0(x, t) - z \frac{\partial w_0(x, t)}{\partial x}, \quad u_2 = 0, \quad u_3 = w_0(x, t), \quad (\text{A.1})$$

where  $(u_1, u_2, u_3)$  are the total displacements along the coordinate directions  $(x, y, z)$ , and  $u_0$  and  $w_0$  denote the axial and transverse displacements of the centroidal (neutral) axis ( $y = z = 0$ ). Equation (A.1) is used in the majority of existing nonlinear formulations. Although, linearization of beam kinematics is apparently incongruent with the notion of geometric nonlinearity, the linearized field provides an adequate description for incremental static and dynamic solutions. In a geometrically nonlinear analysis, using the finite-element method formulation, it is customary to use a nonlinear strain-displacement relation of the form (sum on repeated subscripts is implied)

$$\varepsilon_{ij} = \frac{1}{2} \left( \frac{\partial u_i}{\partial x_j} + \frac{\partial u_j}{\partial x_i} \right) + \frac{1}{2} \left( \frac{\partial u_m}{\partial x_j} \frac{\partial u_m}{\partial x_i} \right). \quad (\text{A.2})$$

Due to the assumption of small strains, no distinction is made here between the material and the spatial coordinates [22]. In the case of planar motions, substitution of the linearized displacement field (A.1) into (A.2) yields

$$\varepsilon_{11} = \varepsilon_{xx} = \frac{\partial u_0}{\partial x} + \frac{1}{2} \left[ \left( \frac{\partial u_0}{\partial x} \right)^2 - 2z \frac{\partial u_0}{\partial x} \frac{\partial^2 w_0}{\partial x^2} + z^2 \left( \frac{\partial^2 w_0}{\partial x^2} \right)^2 + \left( \frac{\partial w_0}{\partial x} \right)^2 \right] - z \frac{\partial^2 w_0}{\partial x^2}, \quad (\text{A.3})$$

and all other strains are zero. Note that the notation  $x_1 = x$ ,  $x_2 = y$  and  $x_3 = z$  is used. The first term in (A.3) represents the centroidal strain of the element according to the Lagrangian (Cauchy-Green) strain tensor, and the last term represents the additional axial strain due to flexure for fibers at a distance  $y$  from the centroid of the cross-section. For the considered microresonators, the longitudinal inertia is small compared with the restoring force, and hence, based on this hypothesis it follows that  $u_0 = O(w_0^2)$  (i.e.  $u_0$  is of the order of  $w_0^2$ ) [23]. Making use of this assumption and neglecting terms of order

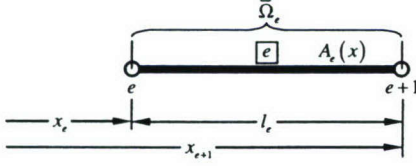


Figure 20. Geometry of a typical finite element.

higher than 2; that is, ignoring terms that involve the square of  $\partial u_0/\partial x$  and retaining the square of  $\partial w_0/\partial x$  (which represents the rotation of a transverse normal line in the beam) yields

$$\begin{aligned}\varepsilon_{11} = \varepsilon_{xx} &= \frac{\partial u_0}{\partial x} - z \frac{\partial^2 w_0}{\partial x^2} + \frac{1}{2} \left( \frac{\partial w_0}{\partial x} \right)^2 \\ &= \left[ \frac{\partial u_0}{\partial x} + \frac{1}{2} \left( \frac{\partial w_0}{\partial x} \right)^2 \right] - z \frac{\partial^2 w_0}{\partial x^2} \\ &\equiv \varepsilon_{xx}^0 + z \varepsilon_{xx}^1,\end{aligned}\quad (\text{A.4})$$

where

$$\varepsilon_{xx}^0 = \left[ \frac{\partial u_0}{\partial x} + \frac{1}{2} \left( \frac{\partial w_0}{\partial x} \right)^2 \right], \quad \varepsilon_{xx}^1 = \frac{\partial^2 w_0}{\partial x^2}.\quad (\text{A.5})$$

These strains are known as von Kármán strains.

### A.2. Strain energy

For a given element, the strain energy  $U^e$  is given by

$$U^e(t) = \int_{V_e} \int_{\varepsilon_{ij}} \sigma_{ij} d\varepsilon_{ij} dV.\quad (\text{A.6})$$

Here  $V_e$  is the volume of the element,  $\sigma_{ij}(x, z, t)$  and  $\varepsilon_{ij}(x, z, t)$  denote the Cartesian components of the stress and the Green strain tensors, respectively. Due to the assumption of small strains, no distinction is made here between the Cauchy and the second Piola–Kirchhoff stress tensors [22]. The total volume of the laminated element is given by the tensor product  $A_e \times \bar{\Omega}_e$ , where  $A_e$  is the cross-sectional area, and  $\bar{\Omega}_e = [x_e, x_{e+1}]$  defines the length of the element. Here,  $x_e$  and  $x_{e+1}$  are the  $x$ -coordinates of the left and right nodes of the element, as shown in figure 20.

In view of the explicit nature of the assumed displacement field (A.1) in the thickness coordinate  $z$  and its independence of coordinate  $y$ , the volume integral can be expressed as the (tensor) product of integrals over the length,  $x_e \leq x \leq x_{e+1}$ , and the cross-sectional area of the element:

$$\int_{V_e} (\cdot) dV = \int_{x_e}^{x_{e+1}} \int_{A_e} (\cdot) dA dx.$$

Therefore, the expression for the strain energy can be simplified as follows (for a beam element, the only nonzero components of strain and stress are  $\varepsilon_{11} \equiv \varepsilon_{xx}$  and  $\sigma_{11} \equiv \sigma_{xx}$ ):

$$U^e(t) = \int_{\bar{\Omega}_e} \int_{A_e} \int_{\varepsilon_{xx}} (\sigma_{xx} d\varepsilon_{xx}) dA dx,\quad (\text{A.7})$$

where  $\sigma_{xx}$  is the axial stress and  $\varepsilon_{xx}$  is the axial strain given by (A.4). Assuming that each layer is isotropic with respect to its material symmetry lines and linearly elastic, the axial stress and strain are related by Hooke's law

$$\sigma_{xx}^{(k)}(x, t) = E^{(k)}(x) \varepsilon_{xx}^{(k)}(x, t), \quad k = 1, 2, \dots, n_{\text{layers}}\quad (\text{A.8})$$

where  $n_{\text{layers}}$  denotes the total number of layers and  $E^{(k)}(x)$  is the modulus of elasticity of the  $k$ th layer. After substituting (A.8) into (A.7) and performing integration over the strain field  $\varepsilon_{xx}$ , the result is

$$\begin{aligned}U^e(t) &= \int_{\bar{\Omega}_e} \int_{A_e} \int_{\varepsilon_{xx}} (E \varepsilon_{xx} d\varepsilon_{xx}) dA dx \\ &= \frac{1}{2} \int_{\bar{\Omega}_e} \int_{A_e} E \varepsilon_{xx}^2 dA dx.\end{aligned}\quad (\text{A.9})$$

After substituting (A.4) into (A.9), the expression obtained is

$$\begin{aligned}U^e(t) &= \frac{1}{2} \int_{\bar{\Omega}_e} \int_{A_e} E \left[ \left( \frac{\partial u_0}{\partial x} \right)^2 + \left( \frac{\partial^2 w_0}{\partial x^2} \right)^2 z^2 \right. \\ &\quad \left. - 2 \frac{\partial u_0}{\partial x} \frac{\partial^2 w_0}{\partial x^2} z - \frac{\partial^2 w_0}{\partial x^2} \left( \frac{\partial w_0}{\partial x} \right)^2 z + \frac{\partial u_0}{\partial x} \left( \frac{\partial w_0}{\partial x} \right)^2 \right. \\ &\quad \left. + \frac{1}{4} \left( \frac{\partial w_0}{\partial x} \right)^4 \right] dA dx.\end{aligned}\quad (\text{A.10})$$

The higher-order term  $1/4(\partial w_0/\partial x)^4$  can be neglected in the above expression. Although the strains are continuous through the thickness, stresses are not, due to the change in material coefficients through the thickness (i.e. each lamina). Hence, the integration of stresses through the laminate thickness requires laminawise integration. Integrating (laminawise) over the cross-sectional area  $A_e$  and noting that since  $z$  is measured from the neutral axis of the multi-layered cross-section, all integrals of the form  $\int z dA$  must vanish, one obtains

$$\begin{aligned}U^e(t) &= \frac{1}{2} \int_{\bar{\Omega}_e} (EA)_{\text{eff}} \left( \frac{\partial u_0}{\partial x} \right)^2 dx \\ &\quad + \frac{1}{2} \int_{\bar{\Omega}_e} (EI)_{\text{eff}} \left( \frac{\partial^2 w_0}{\partial x^2} \right)^2 dx \\ &\quad + \frac{1}{2} \int_{\bar{\Omega}_e} (EA)_{\text{eff}} \frac{\partial u_0}{\partial x} \left( \frac{\partial w_0}{\partial x} \right)^2 dx,\end{aligned}\quad (\text{A.11})$$

where  $(EA)_{\text{eff}}(x)$  and  $(EI)_{\text{eff}}(x)$  denote the effective extensional and bending stiffness of a typical (generic) finite element, respectively. One can note that the first two integrals in (A.11) represent the linear strain energy while the third integral is the contribution from the nonlinear component of the strain,  $1/2(\partial w_0/\partial x)^2$ . In order to derive the stiffness matrix from the expression for the strain energy given by (A.11), it is necessary to express the displacement fields  $u_0(x, t)$  and  $w_0(x, t)$  in terms of the generalized nodal displacements  $d_i^e(t)$ ,  $i = 1, 2, \dots, 6$  (see figure 21). This can be accomplished by assuming a displacement field for  $u_0(x, t)$  and  $w_0(x, t)$ . By letting

$$u_0(x, t) = a_0(t) + a_1(t)x,\quad (\text{A.12})$$

$$w_0(x, t) = b_0(t) + b_1(t)x + b_2(t)x^2 + b_3(t)x^3,\quad (\text{A.13})$$

and using the boundary conditions,

$$u_0(x, t)|_{x=x_e} = d_1^e(t), \quad u_0(x, t)|_{x=x_{e+1}} = d_4^e(t),\quad (\text{A.14})$$

$$w_0(x, t)|_{x=x_e} = d_2^e(t), \quad \frac{\partial}{\partial x} w_0(x, t)|_{x=x_e} = d_3^e(t),$$

$$w_0(x, t)|_{x=x_{e+1}} = d_5^e(t), \quad \frac{\partial}{\partial x} w_0(x, t)|_{x=x_{e+1}} = d_6^e(t),\quad (\text{A.15})$$

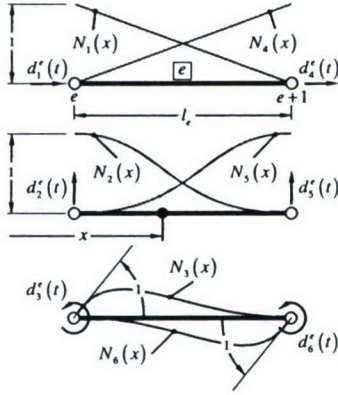


**Figure 21.** Generalized nodal displacements and finite-element basis functions.

it can be shown that

$$u_0(x, t) = [N_1(x) \quad N_4(x)] \begin{Bmatrix} d_1^e(t) \\ d_4^e(t) \end{Bmatrix}, \quad (\text{A.16})$$

where

$$N_1(x) = 1 - \frac{x}{l_e}, \quad N_4(x) = \frac{x}{l_e}$$

are the linear Lagrange basis functions,  $l_e = x_{e+1} - x_e$  is the length of the element  $\Omega_e$  and

$$w_0(x, t) = [N_2(x) \quad N_3(x) \quad N_5(x) \quad N_6(x)] \begin{Bmatrix} d_2^e(t) \\ d_3^e(t) \\ d_5^e(t) \\ d_6^e(t) \end{Bmatrix}, \quad (\text{A.17})$$

where

$$N_2(x) = 1 - 3\frac{x^2}{l_e^2} + 2\frac{x^3}{l_e^3}, \quad N_3(x) = x - 2\frac{x^2}{l_e} + \frac{x^3}{l_e^2},$$

$$N_5(x) = 3\frac{x^2}{l_e^2} - 2\frac{x^3}{l_e^3}, \quad N_6(x) = -\frac{x^2}{l_e} + \frac{x^3}{l_e^2}$$

are the cubic Hermite basis functions. Symbolically, (A.16) and (A.17) can be written respectively as

$$u_0(x, t) = \mathbf{N}_1(x) \mathbf{d}_1^e(t) \quad (\text{A.18})$$

and

$$w_0(x, t) = \mathbf{N}_2(x) \mathbf{d}_2^e(t), \quad (\text{A.19})$$

where  $\mathbf{N}_1(x)$  and  $\mathbf{N}_2(x)$  are referred to as shape function matrices. Furthermore,

$$\frac{\partial u_0(x, t)}{\partial x} = \frac{\partial \mathbf{N}_1(x)}{\partial x} \mathbf{d}_1^e(t), \quad (\text{A.20a})$$

$$\frac{\partial w_0(x, t)}{\partial x} = \frac{\partial \mathbf{N}_2(x)}{\partial x} \mathbf{d}_2^e(t), \quad (\text{A.20b})$$

$$\frac{\partial^2 w_0(x, t)}{\partial x^2} = \frac{\partial^2 \mathbf{N}_2(x)}{\partial x^2} \mathbf{d}_2^e(t). \quad (\text{A.20c})$$

In view of (A.18)–(A.20), the element strain energy  $U^e$  can be written as

$$U^e(t) = \frac{1}{2} \int_{\Omega_e} \mathbf{d}_1^{eT}(t) EA_e \frac{\partial \mathbf{N}_1^T(x)}{\partial x} \frac{\partial \mathbf{N}_1(x)}{\partial x} \mathbf{d}_1^e(t) dx$$

$$+ \frac{1}{2} \int_{\Omega_e} \mathbf{d}_2^{eT}(t) EI_e \frac{\partial \mathbf{N}_2^T(x)}{\partial x} \frac{\partial \mathbf{N}_2(x)}{\partial x} \mathbf{d}_2^e(t) dx$$

$$\times \frac{1}{2} \int_{\Omega_e} EA_e \left[ \frac{\partial \mathbf{N}_1(x)}{\partial x} \mathbf{d}_1^e(t) \right]$$

$$\times \left[ \mathbf{d}_2^{eT}(t) \frac{\partial \mathbf{N}_2^T(x)}{\partial x} \frac{\partial \mathbf{N}_2(x)}{\partial x} \mathbf{d}_2^e(t) \right] dx. \quad (\text{A.21})$$

It is to be noted that even for relatively large deflections, the term  $EA_e/l_e \partial \mathbf{N}_1(x)/\partial x \mathbf{d}_1^e(t)$  may be treated as a constant equal to the axial tensile force in the element. Hence, introducing

$$P_e \cong \frac{EA_e}{l_e} \frac{\partial \mathbf{N}_1(x)}{\partial x} \mathbf{d}_1^e(t) = EA_e \begin{bmatrix} -\frac{1}{l_e} & \frac{1}{l_e} \end{bmatrix} \begin{Bmatrix} d_1^e(t) \\ d_4^e(t) \end{Bmatrix}$$

$$= \frac{EA_e}{l_e} [d_4^e(t) - d_1^e(t)], \quad (\text{A.22})$$

it is obtained that

$$U^e(t) = \frac{1}{2} \mathbf{d}_1^{eT}(t) \left[ \int_{\Omega_e} EA_e \frac{\partial \mathbf{N}_1(x)}{\partial x} \frac{\partial \mathbf{N}_1^T(x)}{\partial x} dx \right] \mathbf{d}_1^e(t)$$

$$+ \frac{1}{2} \mathbf{d}_2^{eT}(t) \left[ \int_{\Omega_e} EI_e \frac{\partial \mathbf{N}_2^T(x)}{\partial x} \frac{\partial \mathbf{N}_2(x)}{\partial x} dx \right] \mathbf{d}_2^e(t)$$

$$+ \frac{1}{2} \mathbf{d}_2^{eT}(t) P_e \left[ \int_{\Omega_e} \frac{\partial \mathbf{N}_2^T(x)}{\partial x} \frac{\partial \mathbf{N}_2(x)}{\partial x} dx \right] \mathbf{d}_2^e(t). \quad (\text{A.23})$$

### A.3. Kinetic energy

In this work, the effect of rotary inertia is ignored. Consistent with this kinematic assumption, the kinetic energy is given by

$$T^e(t) = \frac{1}{2} \int_{\Omega_e} m_{\text{eff}}(x) \left\{ \left[ \frac{\partial u_0(x, t)}{\partial t} \right]^2 + \left[ \frac{\partial w_0(x, t)}{\partial t} \right]^2 \right\} dx, \quad (\text{A.24})$$

where  $m_{\text{eff}}(x)$  is the effective mass per unit length of the multi-layered element. In view of

$$\frac{\partial u_0(x, t)}{\partial t} = \mathbf{N}_1(x) \frac{d\mathbf{d}_1^e(t)}{dt} = \mathbf{N}_1(x) \dot{\mathbf{d}}_1^e(t), \quad (\text{A.25a})$$

$$\frac{\partial w_0(x, t)}{\partial t} = \mathbf{N}_2(x) \frac{d\mathbf{d}_2^e(t)}{dt} = \mathbf{N}_2(x) \dot{\mathbf{d}}_2^e(t), \quad (\text{A.25b})$$

the element kinetic energy  $T^e$  can be written as

$$T^e(t) = \frac{1}{2} \dot{\mathbf{d}}_1^{eT}(t) \left[ \int_{\Omega_e} m_{\text{eff}}(x) \mathbf{N}_1^T(x) \mathbf{N}_1(x) dx \right] \dot{\mathbf{d}}_1^e(t)$$

$$+ \frac{1}{2} \dot{\mathbf{d}}_2^{eT}(t) \left[ \int_{\Omega_e} m_{\text{eff}}(x) \mathbf{N}_2^T(x) \mathbf{N}_2(x) dx \right] \dot{\mathbf{d}}_2^e(t). \quad (\text{A.26})$$

### A.4. Virtual work due to nonconservative distributed forces

The virtual work done by the nonconservative distributed forces has the form

$$\delta \bar{W}_{nc}^e(t) = \int_{\Omega_e} f_u(x, t) \delta u_0(x, t) dx + \int_{\Omega_e} f_w(x, t) \delta w_0(x, t) dx, \quad (\text{A.27})$$

where  $f_u(x, t)$  is the externally applied axial force per unit length,  $\delta u_0(x, t)$  is an arbitrary axial virtual displacement,  $f_w(x, t)$  is the externally applied transverse force per unit length and  $\delta w_0(x, t)$  is an arbitrary transverse virtual displacement. In view of (A.18) and (A.19), the virtual displacements  $\delta u_0(x, t)$  and  $\delta w_0(x, t)$  can be written as

$$\delta u_0(x, t) = \mathbf{N}_1(x) \delta \mathbf{d}_1^e(t) \quad (\text{A.28})$$

and

$$\delta w_0(x, t) = \mathbf{N}_2(x) \delta \mathbf{d}_2^e(t), \quad (\text{A.29})$$

respectively. On using (A.28) and (A.29) in (A.27), the virtual work due to the nonconservative distributed forces has the form

$$\begin{aligned} \delta \bar{W}_{nc}^e(t) &= \left\{ \int_{\Omega_e} f_u(x, t) \mathbf{N}_1(x) dx \right\} \delta \mathbf{d}_1^e(t) \\ &\quad + \left\{ \int_{\Omega_e} f_w(x, t) \mathbf{N}_2(x) dx \right\} \delta \mathbf{d}_2^e(t) \\ &= \delta \mathbf{d}_1^{eT}(t) \mathbf{f}_1^e(t) + \delta \mathbf{d}_2^{eT}(t) \mathbf{f}_2^e(t), \end{aligned} \quad (\text{A.30})$$

where  $\mathbf{f}_1^e(t)$  and  $\mathbf{f}_2^e(t)$  are the generalized element nodal forces. Note that the integration domain above is the small sub-domain ( $0 \leq x \leq l_e$ ) of a typical finite element.

#### A.5. Equations of motion in the time domain

In this section, Lagrange's equations [13, 24] are used to derive the equations of motion. Treating the nodal displacements  $\mathbf{d}^{eT}(t) = \{\mathbf{d}_1^{eT}(t), \mathbf{d}_2^{eT}(t)\}$  as the generalized coordinates, Lagrange's equations take the form

$$\frac{d}{dt} \left( \frac{\partial T^e}{\partial \dot{\mathbf{d}}^{eT}} \right) - \frac{\partial T^e}{\partial \mathbf{d}^{eT}} + \frac{\partial U^e}{\partial \mathbf{d}^{eT}} = \mathbf{f}^e, \quad (\text{A.31})$$

where

$$\mathbf{f}^{eT}(t) = \{\mathbf{f}_1^{eT}(t), \mathbf{f}_2^{eT}(t)\}. \quad (\text{A.32})$$

After using (A.26), one can write

$$\frac{d}{dt} \left( \frac{\partial T^e}{\partial \dot{\mathbf{d}}^{eT}} \right) = \begin{bmatrix} \mathbf{M}_{11}^e & \mathbf{0}_{2 \times 4} \\ \mathbf{0}_{4 \times 2} & \mathbf{M}_{22}^e \end{bmatrix} \begin{Bmatrix} \dot{\mathbf{d}}_1^e(t) \\ \dot{\mathbf{d}}_2^e(t) \end{Bmatrix} = \mathbf{M}^e \dot{\mathbf{d}}^e(t), \quad (\text{A.33})$$

where  $\mathbf{M}^e$  is the element consistent mass matrix, and its nonzero sub-matrices  $\mathbf{M}_{11}^e$  and  $\mathbf{M}_{22}^e$  are defined as

$$\mathbf{M}_{11}^e = \int_{\Omega_e} m_{\text{eff}}(x) \mathbf{N}_1^T(x) \mathbf{N}_1(x) dx \quad (\text{A.34})$$

and

$$\mathbf{M}_{22}^e = \int_{\Omega_e} m_{\text{eff}}(x) \mathbf{N}_2^T(x) \mathbf{N}_2(x) dx. \quad (\text{A.35})$$

In this work, since the system is a natural system (the kinetic energy has the quadratic form shown in (A.26)) [20, 21] and its mass distribution does not depend on the generalized coordinates; hence  $\partial T^e / \partial \mathbf{d}^{eT} = \mathbf{0}_{6 \times 1}$ . By using (A.23), the last term on the left-hand side of (31) can be written in the following form:

$$\begin{aligned} \frac{\partial U^e}{\partial \mathbf{d}^{eT}} &= \left\{ \begin{bmatrix} \mathbf{K}_{E11}^e & \mathbf{0}_{2 \times 4} \\ \mathbf{0}_{4 \times 2} & \mathbf{K}_{E22}^e \end{bmatrix} + \begin{bmatrix} \mathbf{0}_{2 \times 2} & \mathbf{0}_{2 \times 4} \\ \mathbf{0}_{4 \times 2} & \mathbf{K}_{G22}^e \end{bmatrix} \right\} \begin{Bmatrix} \mathbf{d}_1^e(t) \\ \mathbf{d}_2^e(t) \end{Bmatrix} \\ &= [\mathbf{K}_E^e + \mathbf{K}_G^e] \mathbf{d}^e(t). \end{aligned} \quad (\text{A.36})$$

Thus, one can clearly see that the total stiffness of the element consists of two parts, the elastic stiffness  $\mathbf{K}_E^e$  and

the geometrical stiffness  $\mathbf{K}_G^e$ . The elastic stiffness matrix  $\mathbf{K}_E^e$  is the same as that used in the linear analysis and its nonzero sub-matrices are given by

$$\mathbf{K}_{E11}^e = \int_{\Omega_e} (EA)_{\text{eff}}(x) \frac{\partial \mathbf{N}_1(x)}{\partial x} \frac{\partial \mathbf{N}_1^T(x)}{\partial x} dx \quad (\text{A.37})$$

and

$$\mathbf{K}_{E22}^e = \int_{\Omega_e} (EI)_{\text{eff}}(x) \frac{\partial \mathbf{N}_2^T(x)}{\partial x} \frac{\partial \mathbf{N}_2(x)}{\partial x} dx. \quad (\text{A.38})$$

The nonzero component,  $\mathbf{K}_{G22}^e$ , of the geometrical stiffness matrix,  $\mathbf{K}_G^e$ , is given by

$$\mathbf{K}_{G22}^e = P_e \int_{\Omega_e} \frac{\partial \mathbf{N}_2^T(x)}{\partial x} \frac{\partial \mathbf{N}_2(x)}{\partial x} dx. \quad (\text{A.39})$$

It is important to mention that the geometrical stiffness matrix  $\mathbf{K}_G^e$  either increases or decreases the direct stiffness coefficients (diagonal terms), depending on the sign of the axial force  $P_e$ . After substituting (A.32), (A.33) and (A.36) into (A.31), one obtains

$$\mathbf{M}^e \ddot{\mathbf{d}}^e(t) + [\mathbf{K}_E^e + \mathbf{K}_G^e] \mathbf{d}^e(t) = \mathbf{f}^e(t), \quad (\text{A.40})$$

which is the equation of motion for element  $e$  in the global inertial reference system. Expanding this equation of motion to system size and combining all the element equations, the equation of motion for the entire system can be written in the following form:

$$\mathbf{M} \ddot{\mathbf{d}}(t) + \mathbf{C} \dot{\mathbf{d}}(t) + \mathbf{K} \mathbf{d}(t) = \mathbf{f}(t), \quad (\text{A.41})$$

where

$$\mathbf{K} = \mathbf{K}_E + \mathbf{K}_G \quad (\text{A.42})$$

is the global stiffness matrix, and  $\mathbf{M}$ ,  $\mathbf{K}_E$ ,  $\mathbf{K}_G$  and  $\mathbf{f}(t)$  are the (global) mass matrix, elastic stiffness matrix, geometrical stiffness matrix and force vector, respectively. All these matrices and the force vector of the complete system are obtained from the corresponding individual element matrices and load vector by using the direct stiffness method; that is,

$$\mathbf{M} = \mathbf{A}_{e=1}^{n_{el}} (\mathbf{M}^e), \quad \mathbf{K}_E = \mathbf{A}_{e=1}^{n_{el}} (\mathbf{K}_E^e), \quad \mathbf{K}_G = \mathbf{A}_{e=1}^{n_{el}} (\mathbf{K}_G^e)$$

and

$$\mathbf{f}(t) = \mathbf{A}_{e=1}^{n_{el}} (\mathbf{f}^e(t)),$$

where  $\mathbf{A}$  is the so-called assembly operator [25] and  $n_{el}$  is the number of elements in our model.

Here, the Rayleigh proportional damping is introduced in the equation of motion with the following formulation for the damping matrix:

$$\mathbf{C} = \alpha \mathbf{M} + \beta \mathbf{K}. \quad (\text{A.43})$$

In (A.43),  $\alpha$  and  $\beta$  are coefficients which can be obtained from the modal properties of the microresonator.

## Appendix B. Actuator and sensor models

The derivation of the electromechanical coupling at the input and output ports makes use of the constitutive equations of a linear piezoelectric material. The length direction of the piezoelectric film is chosen along the  $x$ -axis, the width direction is chosen along the  $y$ -axis and the height direction is chosen along the  $z$ -axis. This choice of variables implies that the structure of the constitutive equations of a linear piezoelectric material in the 'T-E' form is [26]

$$S_1 = s_{11}^E T_1 + d_{31} E_3, \quad (\text{B.1a})$$

$$D_3 = d_{31} T_1 + \epsilon_{33}^T E_3. \quad (\text{B.1b})$$

Here, the contracted (Voigt) notation is used to simplify the presentation of second- and fourth-order tensors. In (B.1)  $S_1 \equiv \epsilon_{xx}$  and  $T_1 \equiv \sigma_{xx}$  are the strain and stress in the  $x$ -direction of the beam;  $D_3$  and  $E_3$  are the electrical displacement and electrical field along the piezoelectric film in the  $z$ -direction and  $s_{11}^E$ ,  $d_{31}$  and  $\epsilon_{33}^T$  are the  $x$ -axis mechanical compliance at a constant electric field, the transverse-piezoelectric-coupling coefficient and the permittivity at a constant stress of the film, respectively.

At the input port (i.e. the actuator side), through the converse piezoelectric effect, the voltage applied across the active film causes a forced strain equal to

$$S_1(t) = d_{31} E_3(t), \quad (\text{B.2})$$

where  $E_3(t)$  is the electric field across the active film, which is given by

$$E_3(t) = \frac{V_1(t)}{h_p}. \quad (\text{B.3})$$

This forced strain is caused by the electric field, which is uniform through the active film; hence, the forced strain is also uniform in the active film. This means that, if we restrain the active layer from an extension, the forced stress is also uniform through the layer, and it is equal to

$$T_1(t) = \frac{S_1(t)}{s_{11}^E} = S_1(t) E_p, \quad (\text{B.4})$$

where  $E_p$  is Young's modulus of the piezoelectric film. Since the film's offset from the neutral axis, the forced stress given by (B.4) is translated into a distributed internal bending moment  $M(x, t)$ . To obtain an approximation for the distributed moment, one can follow along similar lines of earlier work. The distributed bending moment is given by the product of the lateral force caused by the piezoelectric film,  $T_1(t)h_p b_1(x)$ , and the distance between the film and the neutral axis of the microresonator. Assuming that the thickness of the piezoelectric layer ( $h_p$ ) is relatively small compared to the thickness of the resonator substrate ( $h_e$ ), after using (B.2)–(B.4), the expression for  $M(x, t)$  becomes

$$\begin{aligned} M(x, t) &= [T_1(t)h_p b_1(x)] \frac{h_e}{2} = [S_1(t)E_p h_p b_1(x)] \frac{h_e}{2} \\ &= \frac{1}{2} d_{31} E_p h_e b_1(x) V_1(t). \end{aligned} \quad (\text{B.5})$$

It is known that an externally transverse distributed force,  $f_w(x, t)$ , leads to an internal bending moment at each section of the microresonator structure, but here one has the reverse; one has an internally generated distributed moment inside the

microresonator structure, and it is needed to bring that outside as an externally distributed force that is structurally equivalent to  $M(x, t)$ . From [27], it follows that the relationship between  $M(x, t)$  and  $f_w(x, t)$  is given by

$$f_w(x, t) = \frac{\partial^2 M(x, t)}{\partial x^2}. \quad (\text{B.6})$$

At the output port (i.e. the sensor side), the output current,  $I_2(t)$ , can be written in terms of the output charge,  $Q_2(t)$ , as follows:

$$I_2(t) = \frac{d}{dt} Q_2(t). \quad (\text{B.7})$$

The output charge is found by integrating the electric displacement,  $D_3(x, y, t)$ , over the area of the sensing electrode:

$$\begin{aligned} Q_2(t) &= \int_{L-L_2}^L \int_0^{b_2(x)} D_3 dy dx \\ &= \int_{L-L_2}^L \int_0^{b_2(x)} (d_{31} T_1 + \epsilon_{33}^T E_3) dy dx. \end{aligned} \quad (\text{B.8})$$

In the case of a noncollocated sensor, the voltage across the sensor is maintained at  $E_3(t) = 0$ . After using this fact and appealing again to the actuator equation (B.8) simplifies to

$$Q_2(t) = \int_{L-L_2}^L \int_0^{b_2(x)} d_{31} T_1(x, t) dy dx. \quad (\text{B.9})$$

Here, the stress in the sensing layer,  $T_1(x, t)$ , can be written in terms of the longitudinal strain,  $S_1(x, t)$ , and the Young's modulus of the piezoelectric film,  $E_p$ , as

$$T_1(x, t) = E_p S_1(x, t). \quad (\text{B.10})$$

Since we assume that the thickness of the piezoelectric sensing layer ( $h_p$ ) is relatively small compared to the thickness of the resonator substrate ( $h_e$ ), the longitudinal strain in this layer is approximately equal to the longitudinal strain at the surface of the microresonator structure. This total strain consists of both a bending strain and an extensional strain:

$$S_1^{\text{Bend}}(x, t) = -\frac{h_e}{2} \frac{\partial^2 w_0(x, t)}{\partial x^2}, \quad (\text{B.11a})$$

$$S_1^{\text{Exten}}(x, t) = \frac{\partial u_0(x, t)}{\partial x} + \frac{1}{2} \left( \frac{\partial w_0(x, t)}{\partial x} \right)^2. \quad (\text{B.11b})$$

In this work, the contribution from the nonlinear component of the extensional strain to the output charge is neglected. When the input at the drive electrode has a dc bias, in addition to the time varying excitation, the effect of the nonlinear term is included in the model as a constant axial load. With this assumption, the output charge is found by combining (B.9)–(B.11), resulting in

$$\begin{aligned} Q_2(t) &= d_{31} E_p \int_{L-L_2}^L \int_0^{b_2(x)} \left[ \frac{\partial u_0}{\partial x} - \frac{h_e}{2} \frac{\partial^2 w_0}{\partial x^2} \right] dy dx \\ &= d_{31} E_p \int_{L-L_2}^L b_2(x) \left[ \frac{\partial u_0(x, t)}{\partial x} - \frac{h_e}{2} \frac{\partial^2 w_0(x, t)}{\partial x^2} \right] dx, \end{aligned} \quad (\text{B.12})$$

and, in the frequency domain,

$$\begin{aligned} Q_2(\omega) &= d_{31} E_p \int_{L-L_2}^L b_2(x) \\ &\times \left[ \frac{\partial u_0(x, \omega)}{\partial x} - \frac{h_e}{2} \frac{\partial^2 w_0(x, \omega)}{\partial x^2} \right] dx, \end{aligned} \quad (\text{B.13})$$

where  $Q_2(\omega)$ ,  $w_0(x, \omega)$  and  $u_0(x, \omega)$  are the Fourier transforms of  $Q_2(t)$ ,  $w_0(x, t)$  and  $u_0(x, t)$ , respectively.

## Acknowledgments

The authors thank the researchers (Professor Don DeVoe, Dr Parshant Kumar and Ms Lihua Li) of the Maryland MEMS Laboratory for providing geometric and material properties of AlGaAs and PZT microresonators and experimental data and related inputs. Valuable discussions with Mr He Li are acknowledged. The authors also thank Mr Luke Currano and Mr Jeff Pulskamp of ARL, Adelphi, Maryland for providing figure 12. Support received for this work through DARPA contract no. F3060202C0016, AFOSR grant no. F49620-03-10181 and ARO grant no. W911NF0510076 is gratefully acknowledged.

## References

- [1] Lin L, Howe R and Pisano A P 1998 Microelectromechanical filters for signal processing *J. Microelectromech. Syst.* **7** 286–94
- [2] DeVoe D L 2001 Piezoelectric thin film micromechanical beam resonators *Sensors Actuators A* **88** 263–72
- [3] Currano L 2002 Experimental and finite element analysis of piezoelectrically driven MEMS actuators *MS Thesis* Department of Mechanical Engineering, University of Maryland, College Park
- [4] Balachandran B and Li H 2003 Nonlinear phenomena in microelectromechanical resonators *Proc. of IUTAM Symposium on Chaotic Dynamics and Control of Systems and Processes in Mechanics (Rome, Italy, 8–13 June)* pp 97–106
- [5] Balachandran B and Preidikman S Oscillations of piezoelectric microscale resonators *Progress in Computational Structures Technology* (Stirling: Saxe-Coburg Publications) pp 327–52 chapter 13
- [6] Li H and Balachandran B 2005 Buckling and free oscillations of composite microresonators *J. Microelectromech. Syst.* **15** 1–10
- [7] Park Y-H and Park K C 2004 High-fidelity modeling of MEMS resonators—part I: anchor loss mechanics through substrate *J. Microelectromech. Syst.* **13** 238–47
- [8] Park Y-H and Park K C 2004 High-fidelity modeling of MEMS resonators—part II: coupled beam-substrate dynamics and validation *J. Microelectromech. Syst.* **13** 248–57
- [9] von Preissig F J and Kim E S 2000 Topics in finite-element modeling of piezoelectric MEMS *Int. Conf. on Modeling and Simulation of Microsystems, MSN*
- [10] Wang J S and Ostergaard D F 1999 A finite element-electric circuit coupled simulation method for piezoelectric transducer *IEEE Ultrasonics Symposium*
- [11] Chen B, Cheeseman B A, Safari A, Danforth S C and Chou T-W 2002 Theoretical and numerical predictions of the electromechanical behavior of spiral-shaped lead zirconate titanate (PZT) actuators *IEEE Trans. Ultrason. Ferroelectr. Freq. Control* **49** 319–26
- [12] Ewins D J 1984 *Modal Testing: Theory and Practice* (New York: Wiley) pp 52–4
- [13] Balachandran B and Magrab E B 2004 *Vibrations* (Learning, CA: Brooks/Cole-Thompson)
- [14] Chen S, Baughn T V, Yao Z J and Goldsmith C L 2002 A new in situ residual stress measurement method for a MEMS thin fixed-fixed beam structure *J. Microelectromech. Syst.* **11** 309–16
- [15] Espinosa H D, Zhu Y, Fischer M and Hutchinson J 2003 An experimental/computational approach to identify moduli and residual stress in MEMS radio-frequency switches *Exp. Mech.* **43** 309–16
- [16] Kobrinsky M J, Deutsch E R and Senturia S D 2000 Effect of support compliance and residual stress on the shape of doubly supported surface-micromachined beams *J. Microelectromech. Syst.* **9** 361–9
- [17] Kumar P, Li L, Calhoun L, Boudreaux P and DeVoe D L 2004 Fabrication of piezoelectric Al<sub>0.3</sub>Ga<sub>0.7</sub>As microstructures *Sensors Actuators A* **1115** 96–103
- [18] Pulskamp J S, Smith G, Wickenden A, Polcawich R, Piekarski B and Dubey M 2003 Mitigation of residual film stress deformation in multi-layer MEMS cantilever devices *J. Vac. Sci. Technol. B* **21** 2482–6
- [19] Stricklin J A, Haisler W E and von Rieseemann W A 1971 Geometrically nonlinear analysis by stiffness method *J. Struct. Div.* **97** 2299–314
- [20] Wen R K and Rahimzadeh J 1983 Nonlinear elastic frame analysis by finite element *J. Struct. Eng.* **109** 1952–71
- [21] Thomsen J J 1997 *Vibrations and Stability: Order and Chaos* (UK: McGraw-Hill International)
- [22] Holzapfel G H 2001 *Nonlinear Solid Mechanics: A Continuum Approach for Engineering* (New York: Wiley)
- [23] Nayfeh A H and Mook D T 1979 *Nonlinear Oscillations* (New York: Wiley)
- [24] Meirovitch L 1997 *Principles and Techniques of Vibrations* (Englewood Cliffs, NJ: Prentice-Hall)
- [25] Hughes T J R 2000 *The Finite Element Method: Linear Static and Dynamic Finite Element Analysis* (NY: Dover)
- [26] *IEEE Standard on Piezoelectricity*, ANSI/IEEE Standard 176-1987
- [27] Solecky R and Conant R J 2003 *Advanced Mechanics of Materials* (Oxford: Wiley, Oxford University Press)

# Parametric identification of piezoelectric microscale resonators

A J Dick, B Balachandran, D L DeVoe and C D Mote Jr

Department of Mechanical Engineering, University of Maryland, College Park, MD, USA

E-mail: balab@umd.edu

Received 24 April 2006, in final form 6 June 2006

Published 29 June 2006

Online at stacks.iop.org/JMM/16/1593

## Abstract

Piezoelectrically actuated and sensed microscale resonators have been widely studied for filtering, communication and sensing applications. In this effort, to characterize these resonators, the nonlinear frequency-response behavior of these resonators is examined and parametric identification is carried out. A nonlinear beam model is used with a single-mode approximation to produce a forced Duffing oscillator. Nonlinear analysis is used to obtain the frequency-response equation, and this equation is used along with a least-squares minimization scheme to identify the linear and nonlinear parameter values in oscillator models describing the microscale structures. A linearized analytical model of the stepwise axially varying resonator is also used to obtain additional system parameters. The experimentally identified parameter values are found to be in agreement with predicted values obtained from a nonlinear beam model. Parameter values obtained from multiple sets of data for PZT and AlGaAs microresonators are used to observe trends with respect to a variety of operating conditions.

(Some figures in this article are in colour only in the electronic version)

## 1. Introduction

Piezoelectric microscale resonators and resonator arrays are currently being developed through a number of different efforts. These devices are manufactured by using microelectromechanical systems (MEMS) fabrication techniques with the goal of replacing the bulky macroscale resonators currently in use. With microscale dimensions, they require only a fraction of the space, and in addition, the power requirements are low compared to those of their macroscale counterparts. A number of different resonator devices of various geometries are currently being developed. A few of these include clamped–clamped resonators [1], film bulk acoustic wave resonators (FBARs) [2], ring-shaped contour-mode resonators [3] and various disk resonators [4, 5]. During their development, the presence of nonlinear behavior has been observed in many of these devices [6, 7]. Modeling and identification of the nonlinear behavior of dynamic systems has been the focus of a large number of studies. These efforts include both non-parametric identification methods [8] and parametric identification methods [9–11]. Here, a parametric identification scheme is developed and applied to study the nonlinear dynamic behavior of clamped–clamped microresonators.

Ayela and Fournier [12] proposed a method, in which a Duffing oscillator model is used to determine the parameter values for microstructures exhibiting nonlinear behavior. In their identification scheme, seven parameter values are determined by using seven equations. These equations correspond to the amplitude and frequency of the maxima associated with the increasing (or forward) and decreasing (or backward) frequency sweeps, the frequency difference between the location of the maximum determined during the increasing or forward frequency sweep and the point where the response drops to the lower branch of the response curve and the critical force and amplitude values. These critical values correspond to the separation of the responses observed during increasing and decreasing frequency sweeps into two unique curves. By using a large number of data points, the method proposed in this paper allows for a better representation of the response in the presence of noise and/or small deviations from the ‘ideal’ case, where the experimental data align perfectly with a frequency-response curve determined by using the forced Duffing equation. Furthermore, the scheme does not require data points collected during the backward (or decreasing) sweep of the excitation frequency. Also, the method developed here provides additional information such



Figure 1. Structure of the piezoelectric, microscale clamped-clamped resonator.

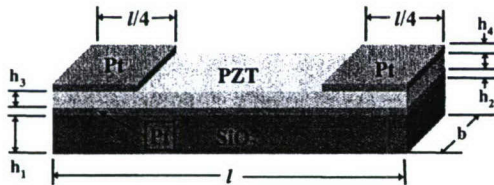


Figure 2. PZT resonator and geometry.

as the average residual stress levels in a microscale structure. A parametric identification scheme was also proposed by Malatkar and Nayfeh [13] to study systems exhibiting similar nonlinear dynamic behavior. However, unlike the scheme described in this paper, the identification scheme of Malatkar and Nayfeh was meant to be applied to frequency-response data that did not exhibit jumps.

In the next section, the microscale structures of interest are discussed and the experimental arrangement is described. In the third section, the model development is presented. The identification scheme is discussed in the fourth section. Preliminary studies of parameter trends are presented in the fifth section. In the last section, remarks are collected and presented.

## 2. Piezoelectric microresonators

The microresonator design studied in this work consists of a clamped-clamped microstructure machined out of a composite wafer [1], as shown in figure 1. The dynamic characteristics of the resonators provide spectral filtering of the electrical signals. In order to produce the desired piezoelectric actuation and sensing capabilities, the device is fabricated from a composite wafer [14]. The different layers of one style utilizing the piezoelectric properties of lead zirconate titanate (PZT) are shown in figure 2. The suspended structure is produced by removing a portion of the silicon substrate from underneath the oxide layer. This silicon dioxide layer, which provides the primary stiffness for the resonator, offsets the neutral axis of the structure from the centerline of the piezoelectric film, and the two platinum layers serve as electrodes for the PZT. The top electrode is separated to create input and output ports for the microresonator. Representative dimensions of geometry corresponding to figure 2 are presented in table 1.

In a second type of microresonators that is studied, aluminum gallium arsenide (AlGaAs) is used for the piezoelectric layer [15]. For this style of resonator, the two electrode layers are produced by doping AlGaAs with silicon (AlGaAs:Si). The thickness of the bottom layer of AlGaAs:Si is increased in this design to provide additional stiffness for the resonator and eliminate the need for an additional layer, such as SiO<sub>2</sub> in the PZT resonators. Some of these resonators are

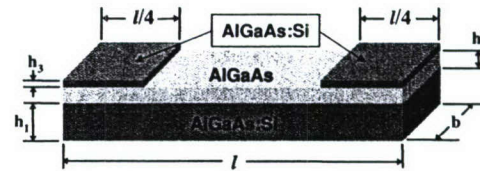


Figure 3. Structure of the AlGaAs microresonator.

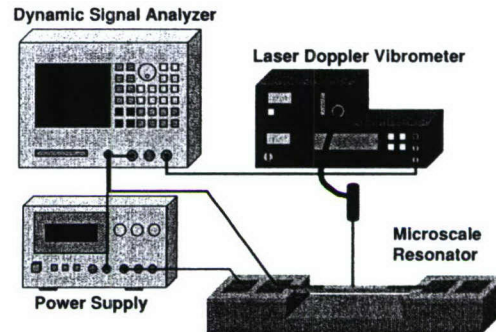


Figure 4. Experimental arrangement utilized to excite and monitor the transverse oscillations of a microscale resonator.

Table 1. Representative PZT resonator dimensions.

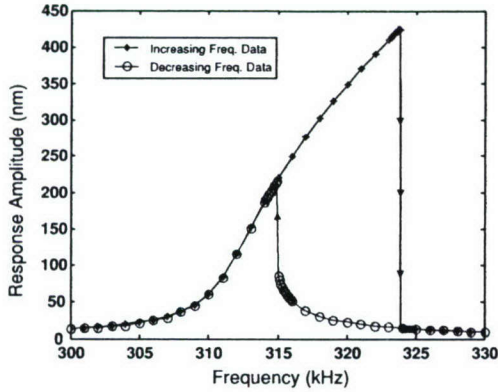
Dimension	Symbol	Value
Resonator length	$l$	200 $\mu\text{m}$
Width of all layers	$b$	20 $\mu\text{m}$
Thickness, SiO <sub>2</sub>	$h_1$	1.06 $\mu\text{m}$
Thickness, bottom Pt	$h_2$	135 nm
Thickness, PZT	$h_3$	530 nm
Thickness, top Pt	$h_4$	200 nm

Table 2. Representative AlGaAs resonator dimensions.

Dimension	Symbol	Value ( $\mu\text{m}$ )
Resonator length	$l$	200
Width of all layers	$b$	10
Thickness, bottom AlGaAs:Si	$h_1$	2.0
Thickness, AlGaAs	$h_2$	1.0
Thickness, top AlGaAs:Si	$h_3$	0.5

being fabricated to be thicker than the PZT resonators. This results in a stiffer device with higher resonance frequencies, and the onset of nonlinear behavior in this device occurs at higher excitation levels. This design also helps eliminate some of the problems that can arise when materials with different lattice structures are placed together on a composite wafer. The arrangement of the three layers of the AlGaAs microresonators is shown in figure 3. One set of dimension values for this resonator type are presented in table 2.

The arrangement of some of the key components of the experimental setup is illustrated in figure 4. With the sample fixed in an RF probe station, a function generator or dynamic signal analyzer is used to apply a harmonic signal while the response is monitored by using laser interferometry. After initially conducting the frequency sweep in a quasi-static fashion, simulations are conducted with the identified parameter values and it is determined that a



**Figure 5.** Frequency-response data for a 200  $\mu\text{m}$  PZT resonator. Data obtained during an increasing frequency sweep are represented by asterisks and data obtained during a decreasing frequency sweep are represented by circles.

swept-sine signal from the analyzer can be used to obtain valid results. The signal produced by the laser vibrometer is sent back to the analyzer to produce a frequency-response plot. A representative frequency-response data set is shown in figure 5, where the response amplitude is given in nanometers and the excitation frequency is given in kilohertz. Data represented by asterisks ‘\*’ correspond to an increasing (or forward) frequency sweep and data represented by circles ‘o’ correspond to a decreasing (or backward) frequency sweep. Although data are shown for both forward and backward frequency sweeps, only the forward sweep data are used in the parametric identification scheme.

### 3. Resonator model

The frequency-response data obtained from the microscale resonators clearly reveal nonlinear characteristics. Although the dimensions of each resonator may suggest that a plate model may be appropriate, a beam representation is found to adequately model the dynamic behavior of the device. To account for the nonlinear behavior of the resonators within the model, both axial stretching and nonlinear curvature are considered [16]. By applying a single-mode Galerkin approximation to the nonlinear beam model, it is found that the contribution of the nonlinear curvature to the coefficient of the resulting cubic term is more than three orders of magnitude smaller than the contribution of the axial stretching term. For this reason, the nonlinear curvature is considered to be negligible. Because of this, only the axial stretching is included when modeling the traverse deflection  $W_n$  as a function of axial position  $x$  and time  $t$ .

$$[P_n(t)\bar{h}(x)]_{,xx} = \rho A_n W_{n,tt} + c W_{n,t} + (EI_n W_{n,xx})_{,xx} + P_0 W_{n,xx} - \sum_{m=1}^M \left[ EA_m / (2l) \int_{l_{m-1}}^{l_m} (W_{m,x})^2 dx \right] W_{n,xx}. \quad (1)$$

Within (1), the parameters and variables used are as follows: mass per length  $\rho A_n$ , viscous damping coefficient  $c$ , bending stiffness  $EI_n$ , compressive axial force  $P_0$ , axial stiffness  $EA_m$  and axial force from piezoelectric layer  $P_n$ .

Furthermore,  $\bar{h}(x)$  is a discontinuous function that describes the separation between the neutral axis and the applied axial force. This separation produces the distributed moment that excites the resonator [7]. The subscripts  $n$  and  $m$  are used to identify the sections of the stepwise axially varying geometry of the structure and  $M$  is the total number of sections. The summation is required to calculate the total axial stretching within all of the sections. Subscripts following a comma ‘,’ indicate partial derivatives. To complete the model, boundary conditions and compatibility conditions are required. The boundary conditions constrain the displacement and slope of the beam at each end to be zero. Since these resonators are made up of three different segments, the displacement profile is separated into three sections that require continuity at the two intersections. In order to accomplish this consistency, the compatibility conditions require that the displacement, slope, moment and shear be equal on both sides of each of the connections. The composite structure of the resonators also requires additional calculations to obtain averaged properties such as the bending stiffness and the axial stiffness. These values are calculated based upon the assumption that the effect of the coupling between bending and stretching is negligible. With the nonlinear partial differential equation, the boundary conditions, the compatibility equations and the averaged properties, the model of the resonator is complete.

In order to facilitate the analysis of this model, the Galerkin procedure is employed. Noting that the response range of interest is close to the resonator’s first natural frequency, a single-mode approximation is used. Through this procedure, the simplified model takes the form of a forced Duffing oscillator, shown as (2) where  $z(t)$  is the temporal amplitude. The coefficients of this equation, to be identified through the parametric identification scheme are the following: the modal mass  $\bar{m}$ , the viscous damping coefficient  $\bar{c}$ , the linear stiffness coefficient  $k$ , the nonlinear stiffness coefficient  $\alpha_3$  and a modal force parameter  $F$ .

With this model, a number of the parameters can be predicted by using the resonator’s geometry, material properties and the resonator’s modeshape function. With either a target frequency or an independent measurement of the axial force  $P_0$ , the modeshape can be determined and used to calculate the values of  $\bar{m}$ ,  $k$  and  $\alpha_3$ . An approximate value of  $P_n$ , and subsequently  $F$ , can be calculated by using the piezoelectric property of resonator and the magnitude of the applied sinusoidal signal. This is discussed in depth in section 5. With the aid of the parametric identification scheme to be presented in section 4, the parameters  $\bar{m}$ ,  $\bar{c}$ ,  $k$ ,  $\alpha_3$ ,  $F$  and  $P_0$  can be identified from experimental frequency-response data of the piezoelectric microscale resonators.

$$\bar{m}\ddot{z}(t) + \bar{c}\dot{z}(t) + kz(t) + \alpha_3 z^3(t) = F \cos(\omega t). \quad (2)$$

The overdots in (2) are used to represent time derivatives. A harmonic excitation is assumed in arriving at (2). The different modal coefficients are defined by

$$\bar{m} = \sum_{n=1}^3 \left\{ \int_{l_{n-1}}^{l_n} \phi_n(x) [\rho A_n \phi_n(x)] dx \right\} \quad (3)$$

$$\bar{c} = \sum_{n=1}^3 \left\{ \int_{l_{n-1}}^{l_n} \phi_n(x) [c \phi_n(x)] dx \right\} \quad (4)$$

$$k = \sum_{n=1}^3 \left\{ \int_{l_{n-1}}^{l_n} \phi_n(x) [EI_n \phi_n^{IV}(x) - P_0 \phi_n''(x)] dx \right\} \quad (5)$$

$$\alpha_3 = \left( \sum_{n=1}^3 \left\{ \int_{l_{n-1}}^{l_n} \phi_n(x) [-\phi_n''(x)] dx \right\} \right) \times \left( \sum_{m=1}^3 \left\{ \frac{EA_m}{2I} \int_{l_{m-1}}^{l_m} [\phi_m'(x)]^2 dx \right\} \right) \quad (6)$$

$$\hat{F}(t) = \sum_{n=1}^3 \left( \int_{x_{n-1}}^{x_n} \phi_n(x) \left\{ \frac{\partial^2}{\partial x^2} [P_n(t) \bar{h}(x)] \right\} dx \right), \quad (7)$$

where the primes in (5) and (6) indicate spatial derivatives and  $\phi_n(x)$  is the considered modeshape function. Previous studies have shown that a forced Duffing oscillator with a hardening-type nonlinearity is capable of producing a frequency-response curve with a structure similar to the experimental frequency-response data obtained from the piezoelectric microscale resonator [17]. Assuming the nonlinearity, damping and forcing to be weak and focusing on excitation frequencies close to the first natural frequency, the method of multiple scales is used to obtain an approximate solution to the nonlinear differential equation (2) [18]. The approximate solution for this case is found as (8) where HOT stands for higher order terms and the amplitude and phase are governed by (9) and (10), respectively.

$$z(t) = a(t) \cos(\omega t - \gamma(t)) + \text{HOT} \quad (8)$$

$$\dot{a}(t) = -\mu a(t) + K \sin(\gamma(t)) \quad (9)$$

$$a(t) \dot{\gamma}(t) = \sigma a(t) - \frac{3}{8} \alpha a^3(t) + K \cos(\gamma(t)). \quad (10)$$

Periodic responses of the microresonator correspond to the fixed points  $(a_0, \gamma_0)$  of (9) and (10), that is,  $\dot{a}(t) = \dot{\gamma}(t) = 0$ . The fixed-point equations provide the frequency-response equation (11), which shows how the amplitude of the periodic response changes with respect to the excitation amplitude and the excitation frequency. The parameter values at which the fixed points lose stability are given by the critical points' equation (12).

$$[\mu^2 + (\sigma - \frac{3}{8} \alpha a_0^2)] a_0^2 = K^2 \quad (11)$$

$$\mu^2 + (\sigma - \frac{3}{8} \alpha a_0^2) (\sigma - \frac{9}{8} \alpha a_0^2) = 0. \quad (12)$$

The variables within (11) and (12) are related to the parameters of (2) by the following relations:

$$\omega_0 = \sqrt{k/\bar{m}}, \quad \Omega = \omega/\omega_0, \quad \sigma = \Omega - 1, \quad (13)$$

$$\mu = \bar{c}/(2\bar{m}\omega_0), \quad \alpha = \alpha_3/k, \quad K = F/(2k).$$

The critical points, where bifurcations occur, are satisfied by both (11) and (12). Analytical curves produced by using these equations are displayed in figure 6.

In order to determine the spatial function needed to calculate the coefficients for the forced Duffing equation from the nonlinear beam model, the linearized system is considered and from analysis of this system along with the boundary and compatibility conditions, the first natural frequency and the associated mode shape are determined. This mode shape is used as the spatial function.

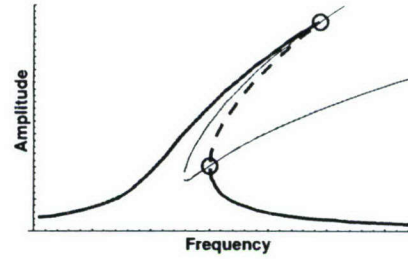


Figure 6. Thick lines are used to show the analytically predicted frequency-response curve, and the stable and unstable response segments are shown by solid lines and dashed lines, respectively. The thin lines are the critical-point curves, which are independent of the excitation level. The encircled intersections of these lines represent the critical points of the frequency-response curves.

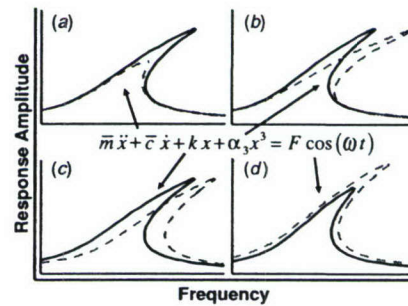
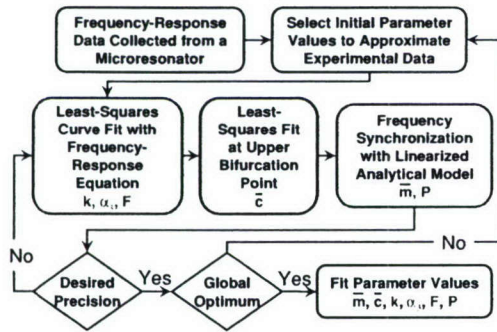


Figure 7. The effects of increasing parameter values on the analytical response curve. The curve depicted by using solid lines corresponds to the nominal case, and the curve illustrated by using dashed lines corresponds to the effect of increasing the following: (a) viscous damping coefficient, (b) nonlinear stiffness coefficient, (c) linear stiffness coefficient and (d) modal force parameter.

### 4. Identification scheme

With the aid of the nonlinear beam model, the system parameters are examined to determine how they affect the structure of the frequency-response curve. In order to determine how best to design the parametric identification process, the damping coefficient, the linear stiffness coefficient, the nonlinear stiffness coefficient and the modal force parameter are examined. The influence of the modal mass is not examined because the modal mass is calculated from the nominal geometry, material properties and approximated mode shape of the resonator. Frequency-response curves showing the effects of an increase in each of these parameters are displayed in figures 7(a) through 7(d). As expected and shown in figure 7(a), the damping coefficient affects the amplitude of the peak of the frequency-response curve while leaving much of the rest of the curve unchanged. The nonlinear stiffness coefficient influences the amount by which the peak of the frequency-response curve leans away from the neutral position corresponding to the first natural frequency, as illustrated in figure 7(b). Changing the value of the linear stiffness results in a shifting of the system's linear natural frequency and this causes the horizontal position of the peak of the frequency-response curve to change, as shown in figure 7(c). The modal force represents the general magnitude



**Figure 8.** A flow chart depicting an overview of the parametric identification scheme utilized to quantify the behavior of the microscale resonators. Starting from the top left corner, experimental data and initial parameter value guesses are input into the identification scheme. The three-part identification process is employed to tune the parameter values by comparing the experimental data with an analytical model. These three steps are repeated until the desired precision is attained. The resulting parameter set is varied and reanalyzed to ensure that they correspond to the global optimum.

of the force being applied to the system and a change in the value of this parameter affects the response amplitude of the entire frequency-response curve most notably at the peak; this is illustrated in figure 7(d).

#### 4.1. Stages of identification

Based on the information presented in figure 7, the parametric identification scheme is developed so that the parameters with the most influence over the response are fit before the parameters that affect the response the least. A flow chart depicting an overview of the parametric identification scheme is presented in figure 8. First, it is necessary to select initial values for each parameter so that the peak of the analytical curve is located within the same frequency range as the experimental data and exhibits a similar structure. While the selection of these values has a very large effect on the results of the parametric identification process, the initial values are easily determined by using relations obtained from the Galerkin procedure and by using a visual comparison of the predicted analytical curve and the experimental data.

Once the initial values are selected, a three-stage parametric identification scheme is applied to determine the optimal combination of parameter values in order to fit the analytical curve to the experimental data. In the first stage, the frequency-response equation (11) is utilized for a least-squares curve fitting process. The parameters determined in this section, in the order identified, are the linear stiffness coefficient, the nonlinear stiffness coefficient and the modal force parameter. These parameters are identified by tuning each parameter as long as the difference between the analytical curve and the entire experimental data set continues to decrease. The parameters are tuned both positively and negatively for a number of different adjustment sizes.

In the second stage of the identification process, the frequency-response equation (11) as well as the critical points equation (12) are utilized to fit the upper

bifurcation point by tuning the viscous damping coefficient. As previously mentioned, the identification procedure is designed specifically to study nonlinear dynamic behavior that experiences jumps in the frequency-response data. Experimental data sets that do not experience jumps can be studied with one of the identification schemes previously discussed, such as the method developed by Malatkar and Nayfeh [13]. Here, a similar tuning procedure is used but only the analytically predicted amplitude of the upper bifurcation point is compared with the amplitude of the last experimental data point before the jump. Although this does not take into account any difference in the frequency, additional iterations of the identification process account for this discrepancy through tuning of the linear stiffness coefficient. While both the modal force parameter and the viscous damping coefficient affect the amplitude value at the peak of the frequency-response curve, only the modal force parameter significantly affects the portion of the curve away from the peak. As a result, it is possible to determine a unique combination of these two parameters for a given set of experimental data.

In the final of the three stages within the identification scheme, the linearized system is used to obtain an approximate mode shape. This mode shape is determined by tuning the axial force within the linearized system to synchronize the first resonance frequency of the model with the frequency calculated from the identified parameter values. The axial force value is tuned in the same fashion as the other parameters. This provides an approximation of the microresonator's mode shape for this natural frequency and an axial force value that can be used to calculate the average residual stress in the resonator. By using this approximate mode shape, the modal mass value can be recalculated. This new modal mass value is then used in the next iteration of the identification process to aid in the further refinement of the values of the other parameters.

Upon completion of these three stages of the identification scheme, the parameter values are examined to determine if the desired level of precision has been obtained. If the parameter values are not determined to sufficient precision, the identification scheme is returned to the first stage of the three-stage process by using the current parameter values for the initial values. Since the system is nonlinear and has a multi-dimensional parameter space, the possibility exists that the identification scheme may converge to local optima and not the global optimum. To avoid selecting local optima, after the scheme has gone through a sufficient number of iterations to produce the desired level of precision, each of the key parameter values,  $\bar{c}$ ,  $k$ ,  $\alpha_3$  and  $F$ , is perturbed both positively and negatively to produce eight different sets of parameter values. These eight sets are then used as initial values and the results of the nine cases are compared. If the first set of parameter values is found to have the best values, then it is considered to represent the 'global optimum'. The quality of each set of parameter values is determined by calculating an RMS error from comparisons of the resulting analytical values with the experimental data. In the event that the best set is one of the eight perturbed sets, these optimized values are perturbed to produce eight new sets and the same process is repeated.

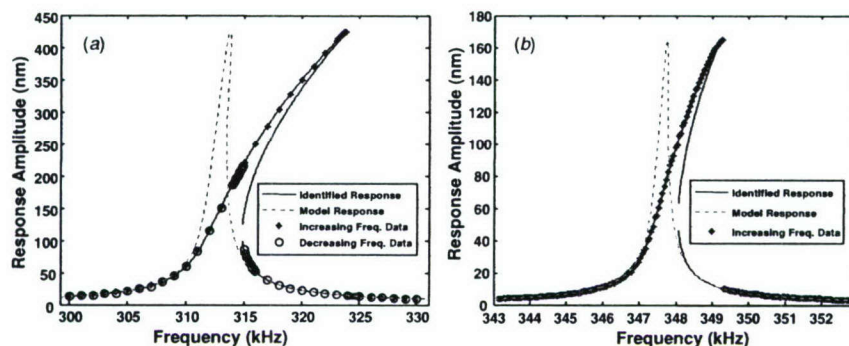


**Figure 9.** Nonlinear frequency-response curves: (a) a 200  $\mu\text{m}$  PZT microresonator and (b) a 200  $\mu\text{m}$  AlGaAs microresonator. Experimental data are represented by asterisks and circles. Analytical curves that are plotted with solid and dashed lines correspond to parameters obtained with the parametric identification scheme and the nonlinear beam model, respectively.

#### 4.2. Identified parameters for PZT and AlGaAs microresonators

The same experimental arrangement and procedures are employed for both PZT and AlGaAs microresonators. In figure 9(a), a comparison of the experimental data and frequency-response curves obtained on the basis of the identified parameter values and beam model parameter values is shown for a PZT microresonator. The large difference between the beam-model response and the identified response is reflected by the parameter values and this is discussed shortly. For the PZT microresonator, a minimal RMS error value of 1.0943 nm is calculated from the forward sweep data and the identified parameter values. Although only the forward sweep data are used to determine the parameter values, the analytical curve plotted with identified parameter values in figure 9(a) shows agreement with both the forward sweep data and the backward sweep data. For this particular data set, the RMS error calculated for the backward sweep data has an even smaller value of 1.0814 nm. This indicates that although the backward sweep data are not taken into account, the identification scheme is able to predict the correct frequency response in the lower branch, including the jump location.

In figures 9(b), the experimental data collected from a 200  $\mu\text{m}$  AlGaAs resonator are presented with analytical curves produced with the parameter values identified by using the authors' identification scheme and those calculated by using the nonlinear beam model. The difference seen between the beam model response and the identified response is similar to that seen for the PZT device. Once again, the parametric identification scheme is able to match the analytical curve to the experimental data well. For the data shown in figure 9(b), an extremely small RMS error value of 0.5666 nm is calculated.

In tables 3 and 4, the parameter values determined by using the parametric identification scheme and numerical values calculated from the nonlinear beam model are shown for the PZT microresonator and AlGaAs microresonator, respectively. The second column of each table contains parameters calculated by using the identified axial force value. The parameters in the third column correspond to residual stress levels determined by using the wafer bow

**Table 3.** Comparison of parameter values for the PZT resonator.

Parameters and units	Parametric identification	Beam model	Beam model (bow stress)
$\bar{m}$ ( $\text{kg} \times 10^{-11}$ )	1.58	1.58	1.58
$\bar{c}$ ( $\text{N s m}^{-1} \times 10^{-8}$ )	7.81	—	—
$k$ ( $\text{N m}^{-1}$ )	60.91	60.88	69.78
$\alpha_3$ ( $\text{N m}^{-3} \times 10^{+12}$ )	32.4	3.54	3.53
$P$ ( $\text{N} \times 10^{-3}$ )	1.50	1.50	1.87
$\omega_0$ (kHz)	312.61	312.55	334.61
$Q_{\text{effective}}$	397.15	—	—
$\sigma_{\text{average}}$ (MPa)	43.56	43.56	54.29

**Table 4.** Comparison of parameter values for the AlGaAs resonator.

Parameters and units	Parametric identification model	Beam	Beam model (bow stress)
$\bar{m}$ ( $\text{kg} \times 10^{-11}$ )	1.13	1.13	1.12
$\bar{c}$ ( $\text{N s m}^{-1} \times 10^{-8}$ )	1.55	—	—
$k$ ( $\text{N m}^{-1}$ )	54.02	54.02	45.83
$\alpha_3$ ( $\text{N m}^{-3} \times 10^{+12}$ )	24.6	2.84	2.84
$P$ ( $\text{N} \times 10^{-4}$ )	-2.68	-2.68	-5.88
$\omega_0$ (kHz)	347.58	347.58	321.42
$Q_{\text{effective}}$	1599.19	—	—
$\sigma_{\text{average}}$ (MPa)	-8.94	-8.94	-19.6

measurement method (e.g., [19]). From comparisons of the identified resonance frequencies, it can be confirmed that the AlGaAs microresonator is stiffer than the PZT microresonator. The experimental AlGaAs data also show lower response amplitude values than the PZT resonator data for equivalent input signals. This observation is consistent with the fact that the AlGaAs resonators are stiffer and experience smaller transverse deflections and that the piezoelectric coupling of the AlGaAs material is not quite as strong as that of the PZT material. However, as seen from tables 3 and 4, the AlGaAs resonator has a higher effective quality factor  $Q$  compared to the PZT resonator. This higher  $Q$ -amplification for the AlGaAs resonators compensates substantially for the increased stiffness and reduced piezoelectric coupling.

In the case of the PZT microresonator, for the identified axial force, the numerically obtained parameter values from the beam model generally agree with the identified values with

the largest discrepancy being between the values obtained for the nonlinear stiffness coefficient. For the numerical values calculated with the residual stress from the wafer bow measurements, the increased stress/axial force values affect the linear stiffness coefficient, and subsequently, the first resonance frequency.

For the AlGaAs microresonator, there is also a difference between the residual stress levels that affect the linear stiffness coefficient and frequency. When comparing the parameter values within table 4, the deviation between the identified and calculated values for the nonlinear stiffness parameter is consistent with results obtained for the PZT resonators. A number of possible sources of this discrepancy are investigated. A single-mode Galerkin approximation is selected because the frequencies examined are in close proximity to the resonators first natural frequency and the second natural frequency has a value of more than twice the value of the first. Studies have shown that the use of the domain method with the device's modeshapes is one of the more successful means to produce a reduced order model [20]. In addition, a profile assembled from multiple single point measurements is found to most closely match the first linear modeshape. When conducting the perturbation analysis, a weak nonlinearity is initially assumed and found to match well to the experimental data. Plotting the RMS error against the excitation amplitude shows that low excitation levels produce nearly linear behavior, moderate excitation levels produce weakly nonlinear behavior and higher levels of excitation produce stronger nonlinear behavior that diverges from the model and produces higher RMS error values. The curvature nonlinearity is not included in the nonlinear beam model for the reason stated in section 3. The consistent deviation between the nonlinear beam model and the experimental data suggests that there may be an additional source of nonlinearity that must be taken into account in the nonlinear beam model to more accurately represent the dynamic behavior of the considered microresonators.

Overall, as demonstrated here, it has been possible to produce a successful curve fit to the experimental data by using the parametric identification scheme constructed on the basis of the Duffing oscillator.

## 5. Trends of identified parameters

Here, results of preliminary investigations conducted into the variations of the identified parameters with respect to the selected inputs or operating conditions are reported. By studying the parameter trends caused by changes in the input signal and operating conditions, it is possible to determine how to improve the resonator design and how to preprocess the input signal to improve the resonator performance. Different swept-sine signals with increasing amplitudes and the addition of various dc bias levels to fixed amplitude sinusoidal signals are considered. The application of a dc voltage has been used to control the stiffness of a MEMS device [21]. The addition of a dc bias to the excitation signal is also used to account for remanent polarization of the piezoelectric material. The parameters examined include the modal force parameter, the linear stiffness parameter and the nonlinear stiffness parameter.

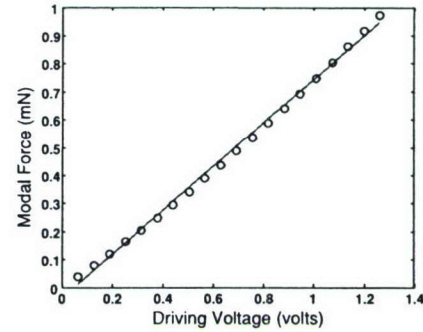


**Figure 10.** Approximating a linear force–voltage relation. The circles ‘o’ represent modal force values for different data sets and the solid line is a linear curve fit to these data points.

### 5.1. Modal force and piezoelectric coefficient

In order to understand how changes in the amplitude of the applied signal affect the modal force parameter, the corresponding term in the nonlinear beam model is examined. The excitation results from the distributed moment produced by the piezoelectric material. The excitation term in (1) is separated into a time-dependent function  $P_n(t)$  and a position-dependent function  $\tilde{h}(x)$ . Following the application of the Galerkin procedure, the modal force function  $\hat{F}(t)$  given by (7) is produced. After carrying out integration by parts twice with respect to  $x$ , (14) is obtained.

$$\hat{F}(t) = P_1(t)h\phi'_1(x_1). \quad (14)$$

By using the block force method to obtain the axial force from the piezoelectric material, the definition of the modal excitation term can be further expanded to include material properties, additional device geometry and the applied voltage. The block force method is a highly approximate method that treats a piezoelectric actuator as a line force without accounting for any spanwise variation of stress or strain. This form of the modal force is given in

$$\hat{F}(t) = EA(d_{31}/t)V(t)h\phi'_1(x_1). \quad (15)$$

This equation can be used to gain additional information about the device. From a number of data sets collected from the same device for increasing drive voltage values, a complete set of parameter values can be identified. A plot of the modal force parameters versus the drive voltage amplitude yields a near-linear set of points under ‘ideal’ conditions. An example of this data is displayed in figure 10. Rearranging (15) to solve for the piezoelectric coefficient,  $d_{31}$ , reveals a term that directly corresponds to the slope of the data points. Because this term consists of two temporal functions, it is important to note that the slope of the data points represents the ratio of the amplitudes of the two harmonic functions and a negative sign must be included to account for the phase difference. This form of the equation is shown in (16), where the actuator area  $A = bh$ ,  $F_0$  is the amplitude of  $\hat{F}(t)$  and  $V_0$  is the amplitude of  $V(t)$ .

$$d_{31} = -(F_0/V_0)(Ebh\phi'_1(x_1))^{-1}. \quad (16)$$

With additional information about the resonator, it is possible to calculate values for the piezoelectric coefficient.

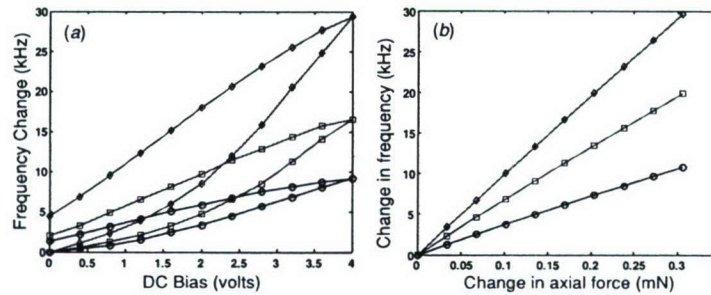


**Figure 11.** Trends of the first, linear natural frequency for different PZT microresonators. Diamonds correspond to 100  $\mu\text{m}$  resonators, squares correspond to 200  $\mu\text{m}$  resonators and circles correspond to 400  $\mu\text{m}$  resonators. Identified parameter values are presented in (a) and model parameter values are presented in (b) showing how the model is capable of explaining the parameter trends.

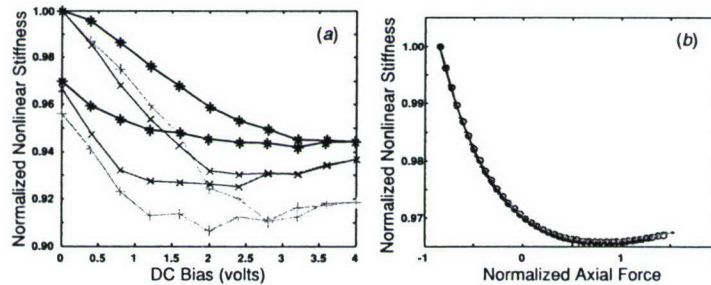


**Figure 12.** Trends of the nonlinear stiffness coefficient for different PZT microresonators. Identified parameter values are presented in (a) and model parameter values are presented in (b) showing how the model is partially capable of explaining the parameter trends.

This is useful since material properties of thin-film materials often differ from their macroscale counterparts and the properties of these materials can be dependent on the various fabrication procedures to which they are exposed. In initial applications of the identification scheme, the determined piezoelectric coefficient values range from  $-116 \times 10^{-12} \frac{\text{m}}{\text{V}}$  to  $-192 \times 10^{-12} \frac{\text{m}}{\text{V}}$ . These thin-film material values are of the same order of magnitude as the piezoelectric coefficient values associated with bulk ceramic materials. However, the thin-film material piezoelectric coefficients are smaller in magnitude.

### 5.2. Axial force, linear stiffness and nonlinear stiffness

The addition of a dc bias to the applied signal produces a constant axial force in the microresonator. As the value of the dc bias increases, the peak of the frequency-response curve shifts to the right. Based on the parametric study previously discussed, the axial force produced by the addition of the dc bias affects the linear stiffness of the resonator. This behavior agrees with the fundamental understanding of the effects of an axial force within clamped-clamped beam structures. By using the nonlinear beam model, it is possible to calculate linear natural frequency values that qualitatively and quantitatively agree with the frequency changes observed in the experimental data. While the model utilized within this work does not include the effects of the hysteresis of the piezoelectric material, a basic linear approximation is compared with identified parameter values to obtain a rough range for the dc bias and the axial force. By using the block force method, that is, axial force =  $EA(d_{31}/t)(\text{dc Bias})$ ,

refined values of this voltage–force ratio can be used to determine the piezoelectric coefficient  $d_{31}$  for the devices. By using the ratio values from this basic model, piezoelectric coefficient values ranging from  $-93.3 \times 10^{-12} \frac{\text{m}}{\text{V}}$  to  $-163 \times 10^{-12} \frac{\text{m}}{\text{V}}$  are determined for the PZT microresonators. Although this is merely a coarse approximation, these values are of a magnitude common for the piezoelectric coefficients of bulk PZT materials.

To qualitatively compare the identified parameters with those of the nonlinear beam model, the changes in the identified first natural frequencies are shown in figure 11(a) for a range of dc bias levels and the changes in the first natural frequencies obtained from the model are shown in figure 11(b) for a range of axial force values. Within these figures, the diamonds ‘ $\diamond$ ’ correspond to a 100  $\mu\text{m}$  PZT resonator, the squares ‘ $\square$ ’ represent the frequency values of a 200  $\mu\text{m}$  PZT resonator and the changes in the frequency values of a 400  $\mu\text{m}$  PZT resonator are represented by the circles ‘ $\circ$ ’.

Another parameter that is significantly affected by the addition of a dc bias is the nonlinear stiffness parameter. Increasing the level of dc bias causes the identified nonlinear stiffness parameter values to decrease. The nonlinear stiffness parameter values also appear to be influenced by the hysteresis of the piezoelectric material. Again, by using only a basic model, a range of axial force values is found where the value of the nonlinear stiffness decreases as the axial force increases. To qualitatively compare the identified parameters with those of the nonlinear beam model, the identified nonlinear stiffness values are shown in figure 12(a) for a range of dc bias levels and the nonlinear stiffness parameters from the model are shown in figure 12(b) for a range of axial force values, both

normalized with respect to their initial parameter values. The axial force values are normalized with respect to the buckling force so that buckling occurs at a normalized axial force value of negative one.

In this section, parameter trends with respect to the resonator inputs have been examined by applying the parametric identification scheme to a series of data sets. These parameter trends included modal force parameter values for various drive voltage amplitudes and linear and nonlinear stiffness variations with respect to dc bias. By using the nonlinear beam model, it has been possible to explain the trends of each of the parameters and produce numerical values that qualitatively agree with the identified values. While further work will be necessary to develop more complete models of the trends, identifying this qualitative agreement is important in validating the selection of the nonlinear beam model and determining the course of future work.

## 6. Concluding remarks

In this paper, a parametric identification scheme is developed with the capability of analyzing nonlinear systems that exhibit jumps in their frequency-response behavior. In addition to its ability to identify the parameter values corresponding to a nonlinear model, this identification scheme can also provide additional information about a device such as the average residual stress level. The identification scheme is applied to frequency-response data collected from piezoelectric microscale resonators in order to quantify their nonlinear behavior. Methods are developed to determine the values of an equivalent viscous damping coefficient, a linear stiffness coefficient, a nonlinear stiffness coefficient, a modal force parameter as well as the level of axial force and the modal mass of the resonator. The identification scheme has been successfully applied to data obtained from both PZT and AlGaAs microscale resonators. The parameter values are also compared to numerical values obtained from a beam model and agreement is seen. The identification scheme is applied to multiple data sets and parameter trends have also been studied.

In future work, it is conceivable that a parametric identification scheme such as that discussed in this work can be used to tailor the characteristics of a MEMS array, so that phenomenon such as localization [22, 23] can be engineered to improve the performance of the considered devices.

## Acknowledgments

Drs Parshant Kumar, Sergio Preidikman, He Li and Lihua Li of the University of Maryland and Dr Brett Piekarski of the Army Research Laboratory, Adelphi, Maryland are thanked for their assistance and interactions with regard to this work. Support received for this work through DARPA contract no. F3060202C0016, AFOSR grant no. F49620-03-10181 and ARO grant no. W911NF0510076 is gratefully acknowledged.

## References

- [1] DeVoe D L 2001 Piezoelectric thin film micromachined beam resonators *Sensors Actuators A* **88** 263–72

- [2] Kirby P B, Su Q X, Komuro E, Zhang Q, Imura M and Whatmore R W 2001 PZT thin film bulk acoustic wave resonators and filters *Proc. IEEE Inter. Freq. Ctrl. Symp. & PDA Exhibition (Seattle, USA, 6–8 June)* pp 687–94
- [3] Piazza G, Stephanou P J, Porter J M, Wijesundara M B J and Pisano A P 2005 Low motional resistance ring-shaped contour-mode aluminum nitride piezoelectric micromechanical resonators for UHF applications *Proc. IEEE Inter. Conf. MEMS (Miami, USA, 30 Jan–3 Feb)* pp 20–3
- [4] Hao Z and Ayazi F 2005 Support loss in micromechanical disk resonators *Proc. IEEE Inter. Conf. MEMS (Miami, USA, 30 Jan–3 Feb)* pp 137–41
- [5] Yan L, Wu J and Tang W C 2005 A 1.14 GHz piezoelectrically transduced disk resonator *Proc. IEEE Inter. Conf. MEMS (Miami, USA, 30 Jan–3 Feb)* pp 203–06
- [6] Balachandran B and Li H 2003 Nonlinear phenomena in microelectromechanical resonators *Proc. IUTAM Symp. on Chaotic Dynamics and Control of Systems and Processes in Mechanics (Rome, Italy, 8–13 June)* pp 97–106
- [7] Li H, Preidikman S, Balachandran B and Mote C D Jr 2006 Nonlinear free and forced oscillations of piezoelectric microresonators *J. Micromech. Microeng.* **16** 356–67
- [8] Masri S F and Caughey T K 1979 Nonparametric identification technique for non-linear dynamic problems *J. Appl. Mech.* **46** 433–47
- [9] Jaksic N and Boltezar M 2002 An approach to parameter identification for a single-degree-of-freedom dynamical system based on short free acceleration response *J. Sound Vib.* **250** 465–83
- [10] Nayfeh A H 1984 Parametric identification of nonlinear dynamic systems *Comput. Struct.* **20** 487–93
- [11] Yasuda K, Kamiya K and Komakine M 1997 Experimental identification technique of vibrating structures with geometric nonlinearity *J. Appl. Mech. Trans. ASME* **64** 275–80
- [12] Ayela F and Fournier T 1998 An experimental study of anharmonic micromachined silicon resonators *Meas. Sci. Technol.* **9** 1821–30
- [13] Malatkar P and Nayfeh A H 2003 A parametric identification technique for single-degree-of-freedom weakly nonlinear systems with cubic nonlinearities *J. Vib. Control* **9** 317–36
- [14] Piekarski B, DeVoe D, Dubey M, Kaul R and Conrad J 2001 Surface micromachined piezoelectric resonant beam filters *Sensors Actuators A* **91** 313–20
- [15] Kumar P, Li L, Calhoun L, Boudreaux P and DeVoe D L 2004 Fabrication of piezoelectric  $\text{Al}_{0.3}\text{Ga}_{0.7}\text{As}$  microstructures *Sensors Actuators A* **1115** 96–103
- [16] Thomsen J J 1997 *Vibrations and Stability: Order and Chaos* (UK: McGraw-Hill)
- [17] Nayfeh A H and Balachandran B 1995 *Applied Nonlinear Dynamics: Analytical, Computational, and Experimental Methods* (New York: Wiley)
- [18] Nayfeh A H 1981 *Perturbation Techniques* (New York: Wiley)
- [19] Pulskamp J S, Smith G, Wickenden A, Polawich R, Piekarski B and Dubey M 2003 Mitigation of residual film stress deformation in multi-layer MEMS cantilever devices *J. Vac. Sci. Technol. B* **21** 2482–6
- [20] Nayfeh A H, Younis M I and Abdel-Rahman E M 2005 Reduced-order modeling for MEMS applications *Nonlinear Dyn.* **41** 211–36
- [21] Adams S G, Bertsch F M, Shaw K A and MacDonald N C 1998 Independent tuning of linear and nonlinear stiffness coefficients *J. Microelectromech. Syst.* **7** 172–80
- [22] Peyrard M 1998 The pathway to energy localization in nonlinear lattices *Physica D* **119** 184–99
- [23] Sato M, Hubbard B E, English L Q, Sievers A J, Ilic B, Czaplewski D A and Craighead H G 2003 Study of intrinsic localized vibrational modes in micromechanical oscillator arrays *Chaos* **13** 702–15